PHOTOPHYSICS OF NOVEL OPTOELECTRONIC MATERIALS UNDER HYDROSTATIC PRESSURE

Front Image: Pressure-induced indirect to direct bandgap transition in methylammonium lead iodide.

Ph.D Thesis, University of Amsterdam, March 2019
Photophysics of Novel Optoelectronic Materials under Hydrostatic Pressure
Tianyi Wang

ISBN 978-94-92323-26-2

PHOTOPHYSICS OF NOVEL OPTOELECTRONIC MATERIALS UNDER HYDROSTATIC PRESSURE

Academisch Proefschrift

ter verkrijging van de graad van doctor
aan de Universiteit van Amsterdam
op gezag van de Rector Magnificus
prof. dr. ir. K.I.J. Maex
ten overstaan van een door het College voor Promoties ingestelde commissie
in het openbaar te verdedigen in de Agnietenkapel
op dinsdag 26 maart 2019 om 12:00 uur

door

Tianyi WANG

geboren te Jiangsu.

Promotiecommissie

promotor: prof. dr. A. Polman	Universiteit van Amsterdam
copromotor: dr. B. Ehrler	AMOLF

Overige leden:

prof. dr. T. Gregorkiewicz,	Universiteit van Amsterdam
prof. dr. E. C. Garnett,	Universiteit van Amsterdam
prof. dr. W. C. Sinke,	Universiteit van Amsterdam
dr. K. Newell,	Universiteit van Amsterdam
prof. dr. A. Rao,	University of Cambridge

Faculteit der Natuurwetenschappen, Wiskunde en Informatica

The work described in this thesis was performed at
AMOLF, Science Park 104, 1098 XG Amsterdam, The Netherlands.
This work is part of the research programme of the Netherlands Organisation for Scientific Research (NWO).
An electronic version of this dissertation is available at https://amolf.nl/.

Two roads diverged in a wood, and I—
I took the one less traveled by,
And that has made all the difference.

The Road Not Taken,
Robert Frost

CONTENTS

1

INTRODUCTION

1

Energy is essential for the daily needs and development of our society. While a significant fraction of energy is generated via burning fossil fuels [1], tremendous amounts of greenhouse gases such as carbon dioxide (CO_2) and nitrous oxide (N_2O) are produced, leading to a global warming that may have severe consequences for the environment. The Intergovernmental Panel on Climate Change (IPCC) has alarmed in its report that the warming needs to be controlled to within 1.5 °C to avoid potentially disastrous impact. To realize this goal, the annual emissions need to be reduced by 50 % between now and 2030, and all fossil fuels need to be completely replaced by renewable energy sources by 2050. [1]

Solar energy is a promising sustainable energy source. Compared to other sustainable energy sources like wind, hydrothermal, tide and biomass, solar energy is highly abundant and relatively equally distributed around the globe. Among various ways of utilizing solar energy, photovoltaics, the process that converts the energy of sunlight directly into electricity, is of great interest for the society. The price of solar panels has dropped significantly in the past decade [2], making photovoltaics an even cheaper energy source than fossil fuels in certain areas of the world [3] and more competitive with fossil fuels in general. Meanwhile, the record lab efficiency of crystalline silicon solar cells has reached 26.7 % [4], which is significantly higher than the efficiency of the best commercially available solar panels (22.8 %, SunPower), indicating that there is still room for a further reduction of cost of solar panels in the future.

The steady increase in efficiency for both lab solar cells and commercial solar panels brought their efficiency close to the fundamental thermodynamic limit for single-junction solar cells like crystalline silicon and Gallium Arsenide (GaAs) solar cells, namely the Shockley-Quiesser limit. Shockley and Queisser calculated the maximum theoretical efficiency of a single-junction solar cell in 1961, taking into consideration spectral losses, blackbody radiation losses and recombination losses and demonstrated that a maximum 33.6 % efficiency could be reached at an optimum bandgap of 1.34 eV under AM1.5G illumination [5]. When realistic loss channels such as Auger recombination are included in the calculation, the maximum efficiency suffers a further drop. The realistic maximum efficiency for single-junction solar cell based on crystalline silicon peaks at 29.8 % [6]. With a 26.7 % record lab efficiency for crystalline silicon solar cells, it is worth noting that the progress of state-of-art manufacturing technology has performed remarkably well in pushing silicon solar cells into its ultimate limit. On the other hand, the room for further increase in efficiency for silicon solar cells is rather limited. New concepts and new materials need to be developed to elevate the efficiency of solar cells above the single-junction Shockley-Quiesser limit, and a clear understanding of the photophysics, especially the influence of micro-to-nanometre scale structure in novel photovoltaic materials will be helpful for material development and device optimization.

In this thesis we focus on the photophysics of novel photovoltaic materials that can potentially help to surpass the Shockley-Quiesser limit and other relevant optoelectronic materials under hydrostatic pressure. We first introduce metal halide perovskites and two exciton conversion processes, singlet fission and triplet-triplet annihilation. For

both we discuss the generation and application of hydrostatic pressure to study the structure-property relationship and conclude with an outline of the thesis.

1.1. METAL HALIDE PEROVSKITES

First discovered by Gustav Rose in 1839 and named after Russian mineralogist Lev A. Perovski, perovskite is a type of mineral that has an ABX_3 structure, where an A-site cation sits in between octahedra with B-site cation located in the center and X-site anion located at the corners (Figure 1.1). For a long time since its discovery, research has been mainly conducted on oxide perovskites with focus on ferroelectricity, superconductance, and catalysis.

Even though the first metal halide perovskite has been synthesized from aqueous solution in 1892 [7], extensive research on metal halide perovskites for solar cells took off only in 2009, as researchers from Japan fabricated a solar cell with 3.9 % power conversion efficiency exploiting methylammonium lead iodide and bromide as sensitizers for dye-sensitized solar cells [8]. In 2013, one of the first solar cells incorporating a planar metal halide perovskite thin film was fabricated by researchers from the University of Oxford, achieving an astonishing efficiency of more than 15 % [9]. Nowadays, the highest efficiency of single-junction lab perovskite solar cell has reached 23.7 %, which is not far from the best silicon solar cells [4], while a 27.3 % record efficiency has been reported for monolithic tandem solar cell based on metal halide perovskites and silicon [4]. Beyond solar cells, many other applications based on metal halide perovskites have been developed, such as light-emitting diodes, photodetectors, lasers and ionic conductors. Perovskite LEDs with more than 20 % external quantum efficiency are reported recently [10–12]. All these results demonstrate a great potential of this class of materials for optoelectronics.

One useful property of metal halide perovskites is that their optical bandgap can be tuned from ultraviolet to infrared by changing the chemical composition [13]. For photovoltaics, this wide range of tunability makes metal halide perovskites not only ideal for single-junction solar cells, but also promising for tandem solar cells either in combination with commercially available photovoltaic materials like crystalline silicon and CIGS or by combining two perovskite materials with different bandgaps. Unlike for III-V semiconductors, where the tuning of composition has to take place in (ultra)high vacuum, the compositional tuning of metal halide perovskites can be achieved in solution, providing great flexibility for device fabrication as well as material morphology from nanocrystals, nanowires, polycrystalline thin films, to single crystals [14–17]. The micro/nano-structure can also be tuned from two-dimensional sheets [18] to three-dimensional frameworks. Surprisingly, despite the polycrystalline nature and the simple fabrication methods of most solution processed metal halide perovskite, the photophysical properties remain top-tier among a variety of commonly used semiconductors. This is not only beneficial from a production point of view, as high quality materials can be fabricated at a relatively low cost, but also spurs a large number of fundamental research questions.

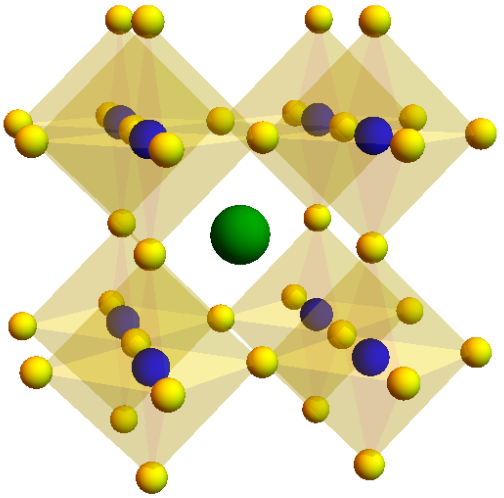

Figure 1.1: Crystal structure of metal halide perovskites. The metal cation (blue) are located in the center of halide (yellow) octahedra, while the organic or inorganic cations (green) are located in between the metal halide octahedra.

One mystery is that metal halide perovskites have a high absorption coefficient and a long charge carrier lifetime at the same time, which is a highly unusual combination for conventional semiconductors. In this thesis, we focus on the structural origin of this phenomenon and investigate how the structure of the material influences the photophysical properties that are relevant for optoelectronic applications. We also study the photophysics of low dimensional perovskites, a promising candidate for light emitting devices under pressure.

1.2. SINGLET FISSION AND TRIPLET-TRIPLET ANNIHILATION

Singlet fission and triplet-triplet annihilation are excitonic conversion processes that only happen in organic (carbon-based) semiconductors. Organic semiconductors differ from inorganic semiconductors in a range of important photophysical properties, perhaps the most important difference is that they form stable, Coulombically bound electron-hole pairs, called excitons.

When light is absorbed in organic semiconductors, electron-hole pairs will be created. Unlike in inorganic semiconductors, where the electron-hole pairs quickly dissociate into free charge carriers due to the low binding energy, electron-hole pairs in organic

semiconductors have a much higher binding energy (up to 1 eV), forming a so-called Frenkel exciton. When the spin of the electron and the hole is antiparallel, the exciton has a net spin of zero and is called a singlet exciton. A triplet exciton is formed when the electron and hole have parallel spins, yielding a net spin of one. The singlet exciton normally carries a higher energy than the triplet exciton due to the exchange energy [19].

When the energy difference between the first excited singlet state (S_1) and the first excited triplet state (T_1) is large enough such that $E(S_1)>2E(T_1)$, the process of singlet fission can occur, where one chromophore in its first excited singlet state can transfer part of its energy to another chromophore close by and form two triplet excitons on the two chromophores [20]. It is a spin-allowed process as the two triplets can have an overall spin of zero, and therefore singlet fission can occur on a femtosecond timescale in certain materials [21]. Singlet fission was first introduced to explain the photophysics in anthracene and tetracene [22, 23] and this assignment was confirmed by magnetic field dependent measurements in 1969 [24, 25]. In the following decades, singlet fission has been observed in a variety of materials, including polyacenes and their derivatives, conjugated polymers and carotenoids [26–30].

In 1979, Dexter proposed for the first time that singlet fission could be used for the sensitization of photovoltaic devices to enhance their power conversion efficiencies [31]. In 2006 Hanna and Nozik proposed that singlet fission could potentially be utilized to increase the efficiency of single-junction solar cells by 25 % if combined with an infrared absorber, yielding a maximum 45 % efficiency theoretically [32]. This article has rejuvenated the interest in singlet fission solar cells. Solar cells incorporating singlet fission layers have shown higher than 100 % external quantum efficiency [33–35], while near-unity efficient transfer of triplet excitons from polyacenes to lead chalcogenide quantum dots has been demonstrated [36, 37], providing solid evidence for the potential benefit of singlet fission for photovoltaics.

Different mechanisms for singlet fission are proposed from the fundamental studies as more experimental evidence is found for the relevant excited states for singlet fission. For example, the process of singlet fission involves intermediate states, and proposals for these states include triplet pair states [38, 39], charge transfer states [40], and quintet states [41, 42]. Yet, a complete physical picture of singlet fission and design rules for highly efficient singlet fission materials are still missing, requiring further investigation into this photophysical process.

Triplet-triplet annihilation (TTA) is the reverse process of singlet fission, where two triplet excitons fuse to form a higher-energy exciton, which can be a singlet, a triplet or a quintet exciton. When a singlet exciton is formed, it can radiatively decay to the ground state by emitting a high-energy photon. This process can be used for a so-called photon upconversion process that converts low-energy photoexcitation into high-energy emission. The photon upconversion process can be of great use in many areas, for instance biomedical therapy [43], solar cells [44] and light-emitting diodes [45]. Highly efficient triplet-triplet upconversion can be realized in solution [46]. However, the liquid nature

strongly limits the application of TTA upconversion. Solid-state and pseudo-solid material systems have also been developed for TTA upconversion and the up-converted light covers a broad range from red to the ultraviolet [47, 48]. However, the quantum efficiency of these systems is significantly lower than the solution systems. A clear understanding of the loss channels is thus needed for the development of solid-state material systems with higher efficiency.

A variety of aspects can have an impact on the rate and efficiency of excitonic conversion processes. In this thesis, we modulate the intermolecular distance and packing via hydrostatic pressure and focus on the effect of intermolecular electronic coupling on the rate and efficiency of the excitonic conversion processes.

1.3. PHOTOPHYSICS UNDER HYDROSTATIC PRESSURE

The structure of a material often determines its properties, which is especially true for semiconductors. For example, the band structure is entirely dependent on the crystal structure of the semiconductor. Materials for photovoltaics, both organic or inorganic, are no exception. Studying the structure-property relationship is therefore important for photovoltaic materials, and the structures of the active materials may be strongly influenced by the operation conditions, leading to variations in device performance. In flexible devices, the strain induced via bending of the substrates can also influence the performance and stability of the devices. Therefore, a clear understanding of the structure-property relationship is important not only for fundamental research but also from a practical perspective.

There are several ways to change the structure and study the influence on photophysical properties. These include direct variation of the structure by changing the chemical nature of the crystal or molecules that form the semiconductor, or more subtle changes like changing the temperature. However, these methods typically influence more than just the structure alone. For solar cells for example, temperature can have an impact on the performance because it also changes the phonon spectrum, the carrier mobilities, the carrier density and the entropy of the systems [49].

In contrast, external pressure is a relatively clean approach to modify the structure of semiconductor materials with little impact on other aspects of the photophysics. Pressure induces strain that changes the intermolecular distance. Since many processes rely exponentially on the molecular distance, even small variations in strain can lead to large variations in the properties.

Various methods of generating pressure can be used in practice. The most common method is a diamond anvil cell, where the sample is placed in between two diamond anvils. When the diamond anvils are pushed closer to each other, a high pressure can be generated on the sample. In the ultrahigh pressure regime (>100 GPa) exotic properties of materials [50] can be reached in the diamond anvil cell, yet there are some drawbacks

of this powerful tool. First, the sample volume allowed for diamond anvil cells is limited to the cubic micrometer range. This limitation rules out the possibility of testing centimeter sized thin film samples, which is the more relevant size for practical solar cell and LED devices. Second, the accuracy of the pressure reading is relatively poor, leading to uncertainties especially for low pressure measurements, the regime most interesting to study subtle changes in semiconductors. Last but not least, for the photovoltaic materials the deformation under realistic operation is significantly below what can be reached in the diamond anvil cells. For practical applications it is thus more interesting to study the materials under mild strain (sub-GPa) that can be encountered in realistic operating conditions, than pushing the materials towards the extremes.

To apply a sub-GPa pressure on semiconductor thin films, many possibilities are available. For instance, pressure can be applied in a gas pressure cell [51], with a fluid/spring-driven piston [52] and by substrate-induced strain [53]. The major concern for a gas pressure cell is the safety. The possibility of gas explosion makes it dangerous for realistic operation. Strain can also be induced via driving a piston. However, the generated pressure is anisotropic, leading to different degrees of deformation in different directions. As thin films are normally deposited on top of substrates, a change in the lattice constant of the substrate can also induce strain in the thin film. However, the substrate-induced strain is also anisotropic. And if the change of lattice constant in the substrate is generated via heating, the temperature change could also induce unexpected changes in the thin film in addition to the substrate-induced strain, as described above. In this thesis we use a hydraulic pressure cell as a tool for pressure generation. This cell uses an inert liquid to transfer the pressure from a piston onto the sample, which sits in a pressure chamber. The sample area is large enough (2.25 cm^2) to house full solar cells, and macroscopic thin films, as well as cuvettes to measure liquids under pressure. The major benefits are the hydrostatic (isotropic) nature of the generated pressure, large sample size, and safe operation.

As pressure directly accesses the structure of materials, pressure-dependent studies on materials have often focused on structural changes such as crystal phase transitions. For materials relevant for optoelectronic applications, the steady-state and dynamic optical properties under pressure are of great interest. Studying these properties under pressure allows to directly link the structural changes with changes in the functionality.

While numerous steady-state optical measurements have been conducted under pressure, time-resolved optical measurements, especially ultrafast optical measurements that can provide information on the initial dynamics in optoelectronic materials upon excitation, are still in very early stage. In this thesis, we perform one of the first ultrafast pump-probe optical measurements of macroscopic semiconductors under hydrostatic pressure.

Both our steady-state and time-resolved measurements focus on the exciton and charge carrier dynamics in materials relavant for photovoltaics and optoelectronics. We show that with this powerful tool, a clearer understanding of photophysics in various

materials is achieved.

1.4. OUTLINE OF THIS THESIS

We use pressure to clarify the photophysics of photovoltaic materials and their evolution in response to structural changes. It is not only interesting as a fundamental research problem, but also highly relevant for realistic applications. In this thesis, we apply hydrostatic pressure on thin films of three- and two-dimensional metal halide perovskites, the singlet fission material rubrene and an upconverting ionic liquid. We measure their steady-state and time-resolved optical properties under pressure.

In Chapter 2, we study the photophysics of thin films of methylammonium lead iodide perovskite (MAPI), a prototypical material for metal halide perovskite photovoltaics, under pressure. We observe a pressure induced phase transition at 325 MPa. From the pressure-dependent steady-state photoluminescence (PL) and PL lifetime measurements we find evidence for the theoretically predicted Rashba-splitting in metal halide perovskites. With pressure we can change the band structure to be less split, and we show that a high-pressure phase transition results in a purely direct bandgap semiconductor.

In Chapter 3, we study the Rashba splitting of two-dimensional (2D) metal halide perovskites under pressure. We find the steady-state optical response of the 2D perovskites to hyrostatic pressure is strongly dependent on the organic spacer in between the lead halide octahedra sheets. The quantum confinement effect is relaxed in a system with short spacers with increasing pressure, while no significant change is observed for a system with long spacers. We do not see evidence for Rashba splitting in monolayer 2D perovskites from time-resolved optical measurements under pressure. We propose pressure studies on multilayer 2D perovskites for a thorough investigation of Rashba splitting in 2D perovskites.

In Chapter 4, we study the effect of intermolecular electronic coupling on singlet fission. Coupling should have a strong effect on singlet fission because it is an intrinsically intermolecular process. We vary the micro-morphology of rubrene thin films and measure their exciton dynamics under pressure. We find that a higher singlet fission efficiency is achieved in amorphous rubrene under high pressure while a slower dissociation rate of the triplet pair is observed in crystalline rubrene. Our study shows that a balance between electronic coupling and energetics needs to be considered for designing highly efficient singlet fission materials.

Similarly to singlet fission, triplet-triplet annihilation involves the interaction of molecular chromophores, and should hence depend strongly on the molecular coupling. In Chapter 5, we study the effect of external pressure on a photon-upconverting ionic liquid network. We find the response of the network to external magnetic field is solid-like. The effect of pressure on the upconverting properties of the network remain inconclu-

sive due to the photo-bleaching damage of the sensitizers. We propose approaches that can be taken to improve the stability.

In Chapter 6, we discuss opportunities of valorization that emerge from the preceding chapters. We propose singlet fission sensitized perovskite solar cells as a potentially cheap and efficient alternative for single-junction silicon solar cells. We discuss the benefits of such devices and the requirement of materials and stability that need to be fulfilled for the realization of such devices. Finally, we look into the potential of such devices compared to single-junction solar cells.

2

INDIRECT TO DIRECT BANDGAP TRANSITION IN METHYLAMMONIUM LEAD HALIDE PEROVSKITE

Solar cells made from hybrid perovskite semiconductors have seen an unprecedented rise in efficiency over the past few years, now reaching efficiency values close to the best silicon solar cells. However, the understanding as to why these materials perform so efficiently is lacking behind the device progress. One of the great mysteries is the unusually long charge carrier lifetime. Conventional semiconductors show either strong absorption and short charge carrier lifetime (direct bandgap semiconductors), or weak absorption and long lifetimes (indirect bandgap). Hybrid perovskites seem to offer both strong absorption and long lifetime, which is very convenient for solar cell operation. Here we show that the origin of the unusually long lifetimes could lie in the peculiar bandstructure of methylammonium lead iodide (MAPI). An indirect transition, arising from a relativistic spin-orbit splitting of the lower conduction band, is present just below the direct bandgap of the perovskites. This allows strong light absorption via the direct transition, then the generated charges relax into the indirect band where they are protected from recombination. We also show that the indirect bandgap disappears at high pressure. Then the lifetime is reduced and the radiative efficiency is doubled which could open the route towards more efficient light emitting devices such as LEDs and lasers.

2.1. INTRODUCTION

Solar cells based on methylammonium lead iodide perovskites (MAPI) have seen an unprecedented increase in efficiency over a short period of time [8, 54–56], while other applications including lasers and photodetectors have shown promise [57, 58]. The high efficiency of these applications arises due to low defect density [17] with long charge carrier lifetime [59] and diffusion length [60], in spite of the material being solution processable. MAPI has widely been considered a direct bandgap semiconductor according to both theoretical calculations and experimental observations [61, 62]. However, the unusually long minority carrier lifetime with values more similar to those of indirect bandgap semiconductors [63], and the associated long charge carrier diffusion length has been a long-standing mystery in the field. It evoked explanations based on long-lived trapping of charges,[64] large polarons [65], reabsorption [66] and triplet exciton formation [67]. Recently, theoretical calculations predicted a slightly indirect bandgap in this material [68]. Brivio et al. calculated the band structure of MAPI using quasiparticle self-consistent GW theory and found that a Rashba-splitting of the conduction band should generate this slightly indirect bandgap [69]. The same relativistic effect has been reported in other calculations. [70–72]

Recent experimental indications point towards a Rashba-split band in $MAPbBr_3$ and MAPI [73]. However, there is little experimental evidence that directly correlates the changes of bandstructure and the charge carrier dynamics of MAPI. The bandstructure of a semiconductor can be altered by structural changes under external application of pressure [74, 75]. Pressure has been applied to MAPI to understand the structural changes [76–78] and the recombination dynamics [79]. It is found that MAPI undergoes a phase transition at around 325 MPa. The phase at ambient pressure is tetragonal [76, 77] and the high pressure phase has been subject to debate, assigned to orthorhombic [76, 78, 79] and cubic [77] crystal phases. A further phase transition is known to occur in the GPa regime [76–78].

Here we find that MAPI has an indirect bandgap 60 meV below the direct bandgap both in absorption and emission spectra. This indirect gap is responsible for the unusually long carrier lifetime because the thermalized carriers are protected against recombination via the fast direct transition. The indirect transition arises from Rashba splitting of the conduction band. The band is split due to the local electric field generated by the absence of inversion symmetry around the Pb site, which acts on the 6p orbitals of the lead-atom where most of the conduction band minimum is located [69, 80].

We study the optoelectronic changes of thin polycrystalline MAPI films under mild hydrostatic pressure up to 400 MPa, below and just above the phase transition at 325 MPa. We show that the bandgap changes with pressure and that the direct transition is enhanced. Above the phase transition MAPI behaves like a purely direct bandgap semiconductor. As the bandgap becomes more direct, the charge carrier lifetime decreases drastically with increasing pressure and the photoluminescence quantum yield (PLQY) exhibits a two-fold increase. These changes can be understood in terms of an increase in

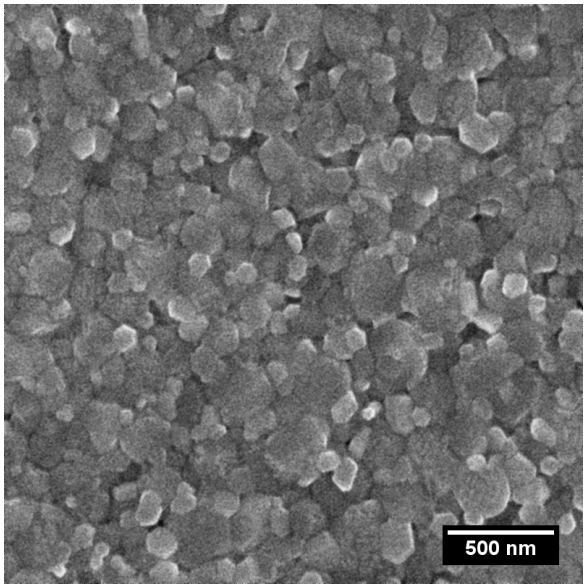

Figure 2.1: Scanning electron micrograph of the MAPI film on fused silica substrate prepared via one-step spin-coating in combination with antisolvent treatment.

inversion symmetry around the Pb site due to a reduction in the in-phase ordering of the MA ions under pressure. These changes lead to a reduction in Rashba splitting, resulting in a more direct bandgap of MAPI. Our results show that small structural changes can significantly improve relevant optoelectronic properties of MAPI.

2.2. RESULTS AND DISCUSSIONS

2.2.1. SAMPLE PREPARATION

We prepare MAPI thin films via a one-step spin-coating method in combination with antisolvent treatment [81]. 1.2 g of PbI_2 was first mixed with 2 mL of anhydrous N,N-dimethylformamide (DMF) and heated to 100 °C while stirring. After PbI_2 was fully dissolved, 0.4 g of methylammonium iodide (MAI) was added to the solution. The solution was kept stirring at 100 °C until MAI was completely dissolved. For the formation of thin films, 100 microliter of solution was deposited onto the glass substrates by spin-coating at 5000 rpm for 20 seconds. After 5 seconds of spinning, 100 μL of chlorobenzene was placed on the sample for the anti-solvent treatment. The sample was then transferred to a hotplate and annealed at 100 °C for 10 min. A dark brown film was obtained after annealing. A scanning electron micrograph of the MAPI film is shown in Figure 2.1.

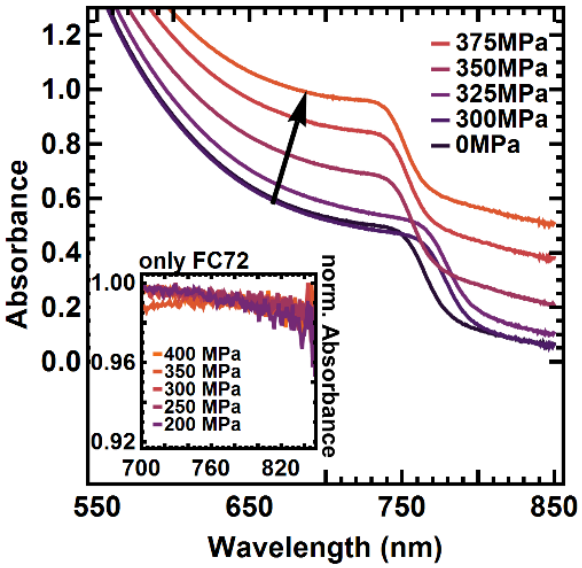

Figure 2.2: Absorption spectra with transparent and translucent pressure liquid. The inset shows the normalized absorption spectra of the pressure liquid without sample at elevated pressure. The spectral response is flat around the band-edge.

2.2.2. ABSORPTION OF MAPI FILM UNDER PRESSURE

We apply hydrostatic pressure to 400 nm thin polycrystalline films of MAPI using a pressure cell filled with an inert, mechanically pumped pressure liquid 2.4. The pressure was first applied from ambient pressure to 400 MPa (pressure upstroke) and then down from 400 MPa to ambient pressure (pressure downstroke), both in steps of 25 MPa. A 5–7 min waiting step after application of pressure and before the measurement was used to allow the material to equilibrate under pressure. The pressure liquid FC-72 started to scatter a fraction of light from 300 MPa onwards (Figure 2.2), presumably because it crystallizes. This effect varies from measurement-to-measurement, so we corrected for it in the absorbance spectra by fitting a linear model to the part of the spectra where MAPI does not absorb (>820 nm) and subtracting the background. From the measurement-to-measurement variability we estimate the upper limit on the error of the pressure reading (following the 5–7 min waiting step) to be 20 MPa. The material is continuously compressed up to a maximum strain of 3 % at 400 MPa, as calculated from a Young's modulus of 12.8 GPa [82]. This value is in good agreement with the change of lattice volume up to 400 MPa, derived from powder X-ray diffraction (PXRD) data [77].

The corrected absorption spectrum remains constant in shape, but the onset of absorption clearly changes with pressure (Figure 2.3a, see Figure 2.13 for complete set of absorption spectra under pressure). To extract the (direct) bandgap, we used the linear part of Tauc plots [83] of the absorption edge. For the pressure upstroke, a continuous red-shift of the absorption edge by 30 meV is observed until 325 MPa (Figure 2.3b).

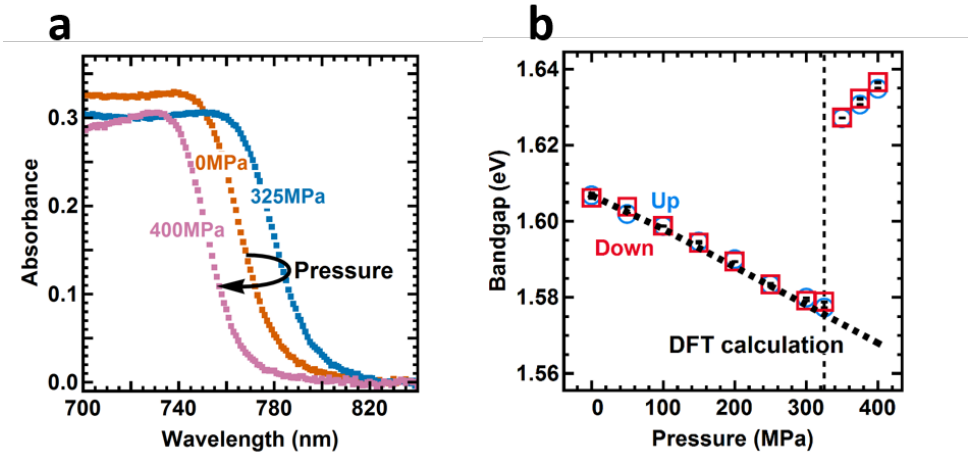

Figure 2.3: (a) Absorbance spectra of MAPI at three characteristic pressures and (b) bandgap shift of MAPI under pressure and DFT calculations (dashed line) predicting the bandgap change

This unusual trend arises due to the electronic band structure associated with the corner sharing lead iodide network [84]. While many semiconductors have negative bandgap deformation potentials (the bandgap increases with increasing pressure), hybrid lead halide perovskites have positive values as the band extrema are found at the boundary of the Brillouin zone (R point) that corresponds to out-of-phase interactions between neighboring unit cells [85]. An abrupt blue-shift occurs above 325 MPa which can be understood as a result of a phase transition from a tetragonal to an orthorhombic or cubic crystal structure [76–79]. The phase transition is followed by a continuous blue-shift. Upon release of pressure from 400 MPa, i.e. the pressure downstroke, the change in bandgap is completely reversible, thus we can infer that the deformation of the crystal lattice is elastic and therefore the pressure-induced structural changes, including the phase transition, are reversible. The change in bandgap is in good agreement with the result of density functional theory (DFT) calculations before the phase transition (dashed line in Figure 2.3b). Atomistic modeling was not attempted on the high-pressure structure that emerges above 325 MPa, so the secondary blue-shift is not recovered in the calculations.

2.2.3. STEADY-STATE PHOTOLUMINESCENCE OF MAPI FILMS UNDER PRESSURE

The steady-state photoluminescence (PL) spectra of MAPI reveal peculiar behavior under pressure (Figure 2.4, see Figure 2.14 for complete set of PL spactra under pressure). We find that the PL spectrum is composed of two distinct peaks before the phase transition, and that one peak is sufficient to fit the data after the phase transition (see Section 2.5.1 for details). At 0 MPa, the dominating emission peak is located at around 1.61 eV,

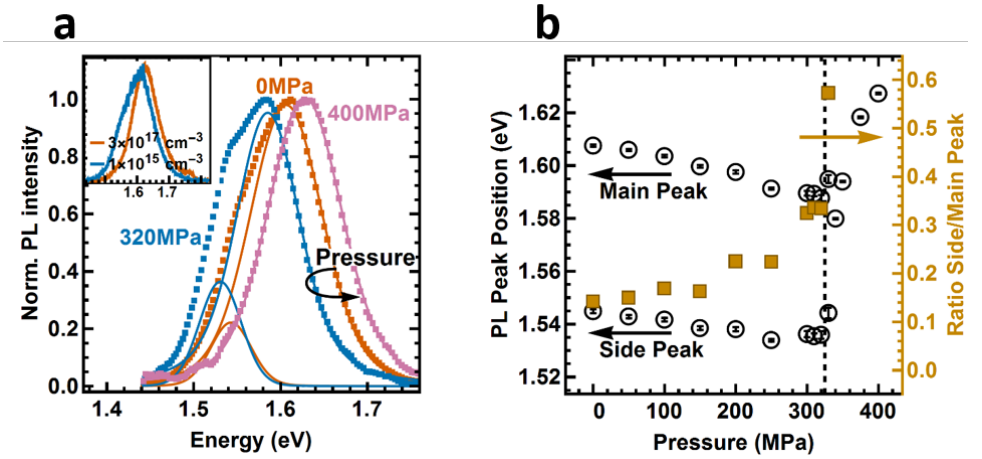

Figure 2.4: (a) Steady-state photoluminescence (PL) spectra of MAPI at three characteristic pressures, inset shows ambient pressure PL spectra of MAPI at low and high excitation densities and (b) Shift of main and side PL peaks of MAPI and the ratio between main and side peaks under pressure

while a side emission peak is located at around 1.55 eV. The side peak disappears at high excitation densities (as shown in the inset of Figure 2.4a). Many reports at high excitation densities hence do not resolve the side peak [67, 86, 87], and in reports at low excitation density the asymmetric PL spectrum is often ignored [79, 88–91]. The main peak has been assigned to band-to-band recombination and speculations about the origin of the side peak include phonon-assisted recombination [87] and exciton–phonon interaction [92]. A PL side peak has also been observed in the low-temperature orthorhombic phase of MAPI. However, that side peak has been assigned to trapped [93, 94] or bound [57, 67] charge-carrier pairs, which, as we show, is different compared to the side peak at room temperature. With increasing pressure up to 325 MPa, the main peak exhibits a red-shift by 10 meV and side peak exhibit a red-shift by 20 meV (Figure 2.4b). The main peak shows an abrupt blue-shift at the phase transition followed up by a continuous blue-shift up to 400 MPa, which is consistent with the shift of absorption edge. Following previous work [79] and from the PL peak position [93] we assign the high-pressure phase to the orthorhombic phase. In the following we will show that the side peak in the low pressure phase arises from an indirect transition 60 meV below the direct bandgap.

Recent theoretical studies have predicted that a Rashba splitting of the conduction band is present for MAPI, leading to a slightly indirect transition 50 to 75 meV below the direct bandgap28 (Figure 2.5). This is due to strong spin–orbit coupling (SOC) in the MAPI crystal. The conduction band minimum in MAPI is mainly formed by the lead (Z = 82) 6p orbitals, while the valence band maximum is mainly formed by iodine (Z = 53) 5p orbitals. As the spin-splitting scales approximately with Z^2, the valence band is less affected than the conduction band. Therefore, although a small splitting of the valence band is observed in the calculations, it is negligible compared to the large splitting in

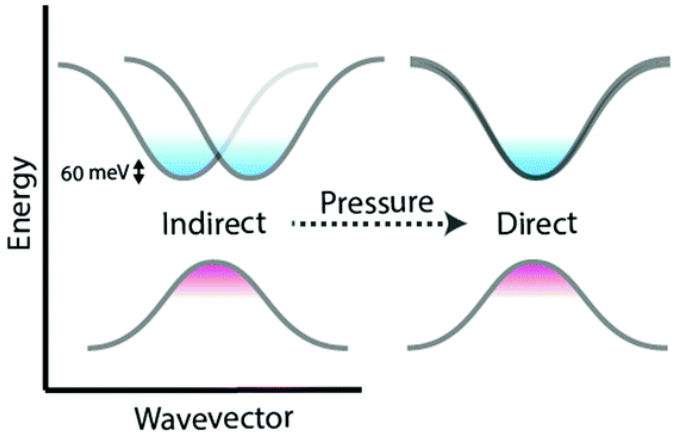

Figure 2.5: Schematic illustration of theoretical prediction of bandstructure of MAPI and pressure-induced changes

conduction band. The flattened valence band provides a large density of states that enables strong direct absorption. However, when MAPI is excited at low intensities, mainly the bottom of the conduction band will be filled, which means that (slow) indirect transitions will play a significant role.

In our PL spectra, the energy of the side peak is 60 meV below the main peak, which fits the theoretical prediction (the energy of the phonon required is small in comparison, see Section 2.5.2 for details). The ratio between the area of side and main peak is increasing with increasing pressure up to 325 MPa (Figure 2.4b). At the same time the difference in energy between the peak positions is reduced, from 60 meV to around 50 meV at 300 MPa (Figure 2.6). After the phase transition at 325 MPa only one PL peak is present. These phenomena can be understood as a result of changes in the ordering of MA ions. In-phase ordering of MA ions increases Rashba-splitting, while out-of-phase ordering decreases the splitting. The ordering of MA ions decreases at low pressure before the phase transition to decrease the occupied volume. The ambient tetragonal phase features in-phase ordering of the MA ions [95], hence the decrease in order at low pressure reduces the splitting. After the phase transition MAPI is in the orthorhombic phase, which features out-of-phase order [95], where the splitting vanishes and MAPI becomes a purely direct bandgap semiconductor.

2.2.4. INDIRECT BANDGAP IN PHOTOTHERMAL DEFLECTION SPECTROSCOPY

The indirect bandgap is also apparent in the absorption spectrum below the direct bandgap. We find that data gathered from photothermal deflection spectroscopy (PDS, data taken from [96–98]) can only be fitted with both a direct bandgap and an indirect bandgap between 46 and 60 meV below the direct gap, in addition to the Urbach tail (Figure 2.7, see Section 2.5.3 for details). Combining only a direct bandgap and the Urbach tail (dashed

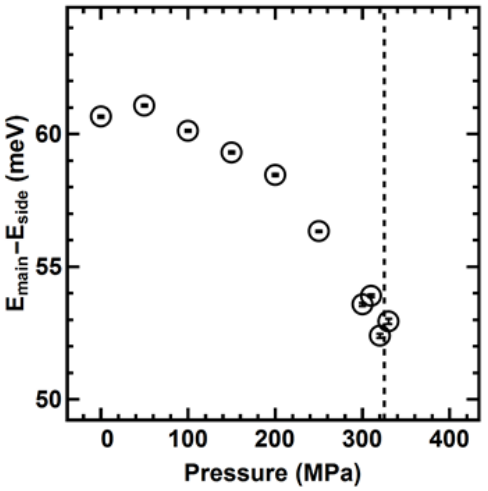

Figure 2.6: Energy difference between main and side PL Peaks of MAPI under pressure.

lines in Figure 2.7) yields a very poor fit. We note that the Tauc analysis is only valid in the absence of significant excitonic contribution to the absorption spectrum in the relevant region [99]. An excitonic and a continuum contribution following the Elliott formula can also yield a reasonable fit to the absorption spectrum, though with much larger residuals in the region where we expect the indirect bandgap (see Figure 2.15). This indicates that accurately describing the below-bandgap absorption spectrum does require an indirect bandgap. Additionally, the dramatic changes we observe under pressure cannot be explained by an excitonic contribution alone, without invoking the indirect bandgap, since the change in excitonic contribution to the absorption spectrum under pressure is small (see Section 2.2.6), in stark contrast to the strong changes in the optoelectronic properties.

2.2.5. RECOMBINATION DYNAMICS OF MAPI FILMS UNDER PRESSURE

We expect the transition towards a more direct bandgap under pressure to result in a shorter excited state lifetime. We use time-correlated single photon counting (TCSPC) to probe the excited state lifetime at different pressures. The sample is excited with a red laser at 640 nm (12 nJ cm^{-2}), at a low initial charge carrier density of around $6 \times 10^{14} cm^{-3}$. This mild excitation density reduces the filling of the conduction band and thus enhances the contribution seen from the indirect transition. The PL decay curves at representative pressures are shown in Figure 2.8a. By modelling the decay curves using the equation shown in the inset of Figure 2.8a, the monomolecular and bimolecular decay rates can be extracted. We find that both bimolecular and monomolecular decay rates increase at higher pressure (Figure 2.8b) . We note that this is contrary to the trend recently measured for MAPI powders [79]. To determine how well bimolecular recombination competes with monomolecular recombination we calculate the fraction of charge

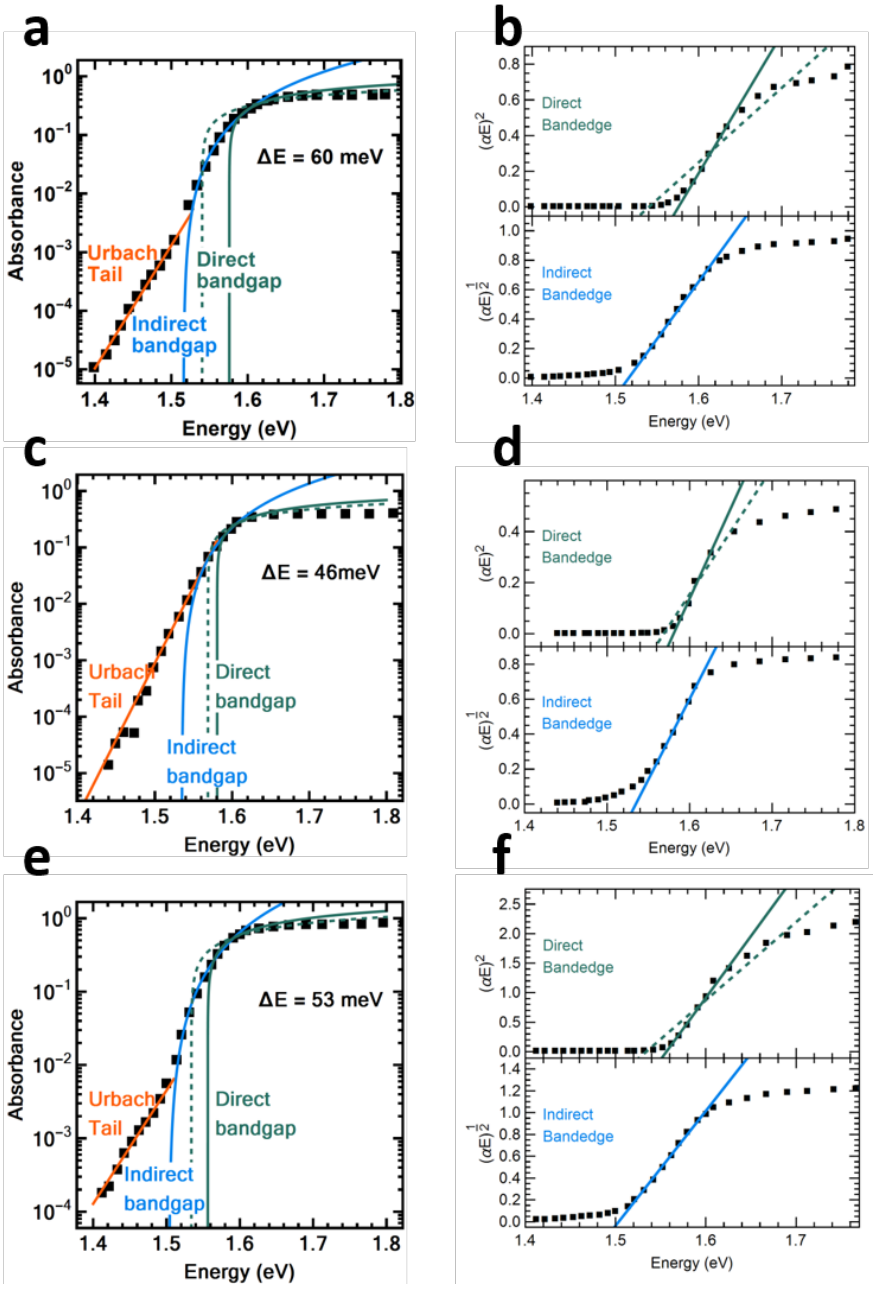

Figure 2.7: PDS data from (a) Sadhanala et al., (c) de Wolf et al. and (e) Zhang et al. fit with an exponential Urbach tail (orange) and indirect (blue) and direct (green) bandgaps. A fit of only a direct bandgap and Urbach tail is shown in dashed green. The energy distance between direct and indirect bandgap is 60, 46 and 53 meV, respectively. A large Urbach tail overlaps with the indirect bandgap. (b), (d) and (f): Linearized data according to the Tauc rule with linear fits.

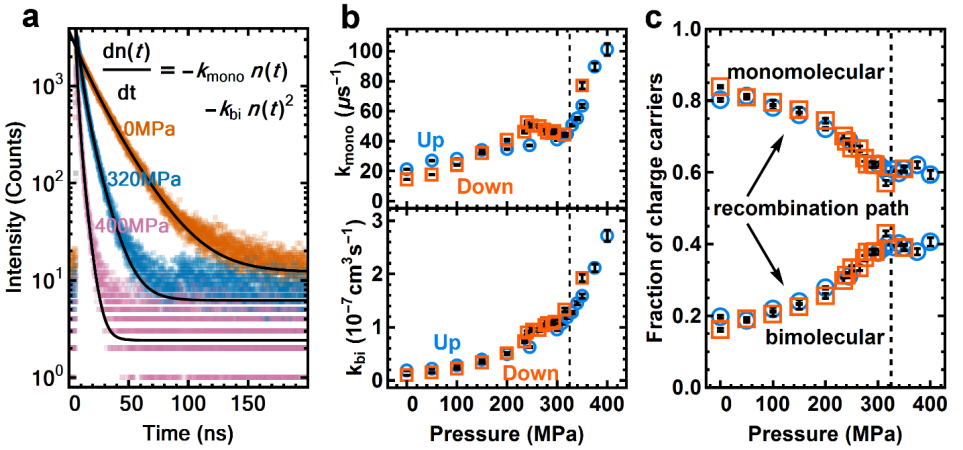

Figure 2.8: Time-Correlated Single Photon Counting (TCSPC) data of the PL of a MAPI film under pressure, excited with a 640 nm laser. (a) TCSPC data of 0 MPa, 320 MPa and 400 MPa pressure. The black line shows the fit from the model shown in the inset. (b) Monomolecular (top) and bimolecular (bottom) decay rates of the charge carriers, extracted from the fit. The bimolecular recombination rate (bottom) changes faster with pressure than the monomolecular recombination rate, with both changing slope after the phase transition at 325 MPa (dashed line). Black bars inside symbols represent the error from the fit. (c) Fraction of charge carriers that decayed through the monomolecular channel and bimolecular channel.

carriers that decayed via the bimolecular (radiative) and monomolecular (non-radiative) path (Figure 2.8c) . The internal radiative efficiency increases from 20 % at ambient pressure to 40 % at 325 MPa and remains at around 40 % from 325 to 400 MPa (Figure 2.8c). The increasing fraction of radiatively decaying charge carriers and hence increase in PLQY is a result of an increasingly direct nature of the bandgap. The cross-section for vertical electron–hole recombination is increased as Rashba splitting is decreased. This model is consistent with the strong increase in PLQY with increasing excitation density [100, 101] as higher excitation density saturates the indirect transition and enhances the direct transition (numerically shown in [80]). Similar effects can also be seen in the low-temperature orthorhombic phase of MAPI where an ordered anti-ferroelectric structure is formed that suppresses internal electric fields [88]. We therefore propose that the enhancement of PLQY at high pressure has the same microscopic origin as the recently reported low temperature optoelectronic behavior.

2.2.6. DISCUSSIONS

The PL side-peak and the slow recombination have been associated with trap states [93, 94] and excitonic effects [57, 67], and cation reorientation could also affect the PL spectrum [68]. In the following we discuss our reasoning for assigning the effects observed under pressure to the indirect bandgap instead.

We can exclude trap states as a major factor that causes the effects under pressure

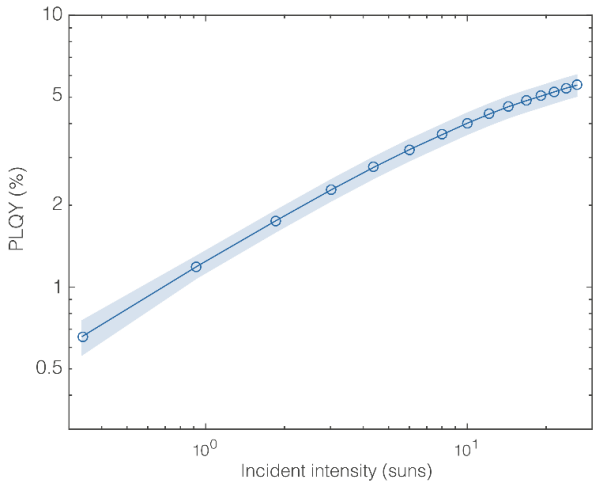

Figure 2.9: Photoluminescence quantum yield (PLQY) of MAPI as function of excitation intensity.

as trap states cannot account for the simultaneous increase in the PLQY and in the side peak contribution of the PL spectra. If the trap states were to become more relevant under pressure one would expect the PLQY to decrease instead. To confirm that the charge carrier dynamics are not dominated by trap states, we measure the external PLQY of our films (Figure 2.9, see Section 2.5.4 for details), which is comparable to values measured for films showing very high solar cell performance [89].

We also compare the PL spectra of samples made by different processing methods, and compare several samples made by the same method (see Section 2.4 for details). We observe the same PL side peak in all samples, with differences in the magnitude of the effect, and a slight difference in the energy difference between main and side peak (Figure 2.10). These differences might arise from different doping levels induced by different preparation methods.

We also observe the same behavior under pressure (Figure 2.11) for a sample prepared via dipping method (see Section 2.4 for details). It is unlikely that the same photoluminescence behaviour appears for such different samples if it came from deposition-induced traps or phase separation.

MA cation reorientation following excitation could also lead to a lower-energy state with a long lifetime. However, we think that it does not explain our dataset. For example, the absorption spectrum should show no significant features of such a low-energy transition, because the cation re-orientation only happens after charge generation. Also, the PL spectrum shows that the majority of the carriers decays via the high-energy transition, which can be easily explained by the Rashba-split conduction band, but would be very unlikely if the charge carrier protection would arise through the re-orientation of

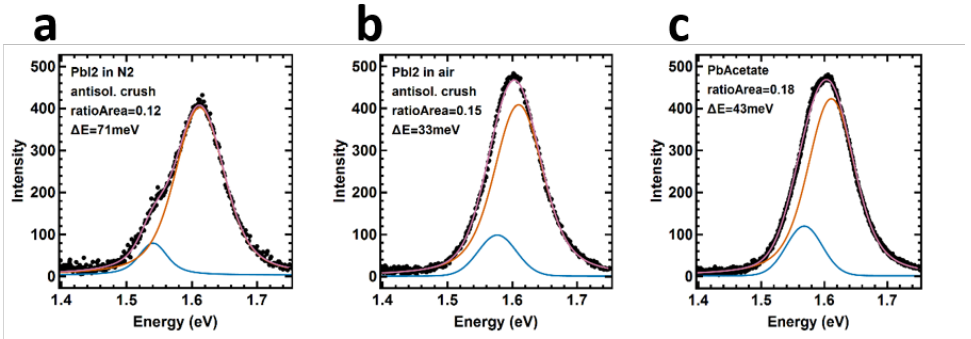

Figure 2.10: Steady-state PL spectra of MAPI film prepared via (a) one-step spin-coating using lead iodide as precursor with antisolvent treatment in glovebox and (b) in air and (c) one-step spin-coating using lead acetate as precursor.

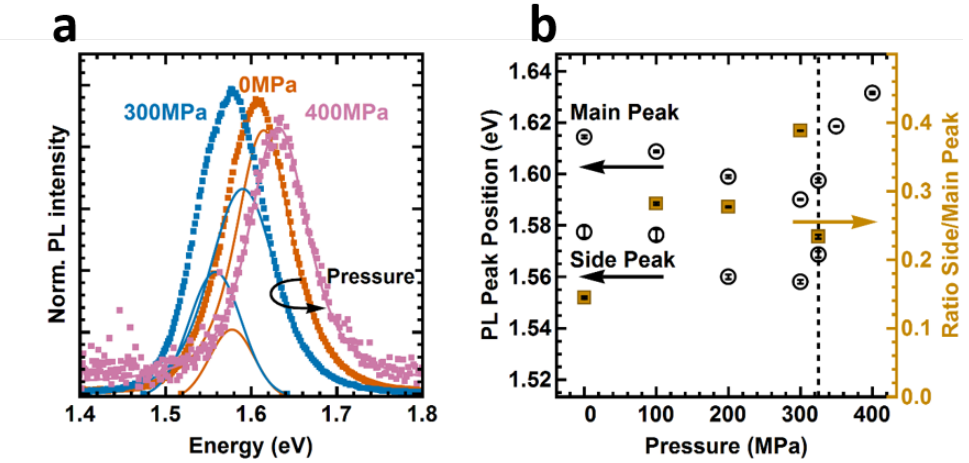

Figure 2.11: (a) Steady-state photoluminescence (PL) spectra of MAPI film prepared via dipping method at three characteristic pressures, inset shows ambient pressure PL spectra of MAPI at low and high excitation densities and (b) Shift of main and side PL peaks of MAPI and the ratio between main and side peaks under pressure.

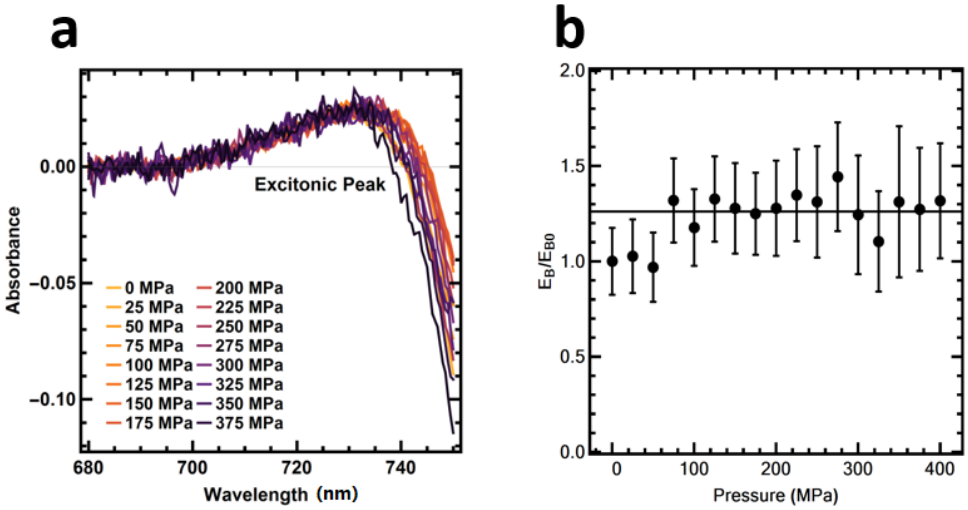

Figure 2.12: (a) Excitonic peak in absorbance data. No change in height (indicating a change in exciton binding energy) is visible in the raw data. (b) Change in exciton binding energy in percent over pressure. No structure is visible, the variation is likely from measurement noise. Black line is the mean, error bars from the noise standard deviation.

the cations. In that case the emission would come from the low-energy transition, with the exception of the very early-time PL, before the reorientation.

It is conceivable that the exciton in perovskites also stabilizes the excited state. We calculate the change of exciton binding energy over different pressures (Figure 2.12). Our data is consistent with no change in exciton binding energy over the entire pressure range, even across the phase transition, with an upper bound of a relative change of 26 %. Such mild changes are unlikely to result in a 5-fold decrease in charge carrier lifetime and a 2-fold increase in PLQY.

We note that Rashba splitting is still a controversial topic in the field. Recent experimental and theoretical studies have proposed that MAPI is a purely direct bandgap material [102–104] or a Rashba type material that behaves like a direct bandgap material [105], and that the Rashba-splitting may not be responsible for the slow recombination of charge carriers [106]. Other experimental and theoretical evidence supports the notion of an indirect behavior [91, 107, 108]. Our results, together with this intense discussion show that it is important to carefully consider the material and the measurement conditions (in particular carrier density), and that further work is needed to elucidate on both the presence of Rashba splitting, and its effect on the photophysics. Angular-resolved photoemission spectroscopy (ARPES) measurements such as done for $MAPbBr_3$ [73] and magnetic field dependent measurements could provide further insights.

We note that the reduction in recombination rate by the indirect bandgap appears beneficial for solar cells because it means that charge carriers can be extracted easily. This, however, is only the case if carrier transport is limiting device performance. In most perovskite devices transport is efficient, and then the increased radiative rate of a direct bandgap is, in fact, beneficial for a solar cell as it could increase the open-circuit voltage [109].

2.3. CONCLUSIONS

In conclusion, our results indicate that the prototype hybrid perovskite MAPI has an indirect bandgap. This arises from distortion of the lead iodide framework, which leads to an electric field across the Pb atom, splitting the conduction band (Rashba splitting). The position of the indirect transition 60 meV below the direct transition is consistent with an absorption spectrum that almost resembles a direct bandgap semiconductor. At the same time, charges thermalized in the conduction band are protected from recombination because recombination requires a change in crystal momentum. Hence, the slightly indirect bandgap explains the apparent contradiction between the long charge carrier lifetime and diffusion length, and the efficient absorption of perovskite semiconductors. Under pressure, the electric field across the Pb atom is reduced, increasing the relative strength of the direct transition, which reduces the charge carrier lifetime and increases the radiative efficiency. This tunability opens the path towards new, rational material and structural developments of perovskite semiconductors with engineered band structure. These materials could be even better suited for solar cells with a higher photovoltage, highly efficient LEDs, and lasers with low lasing threshold.

2.4. METHODS

Methylammonium lead iodide (MAPI) thin films were prepared via solution-based methods, including spincoating, spincoating in combination with antisolvent precipitation and a dipping method. All chemicals were purchased from Sigma-Aldrich and used as received. Fused silica glass substrates were sonicated with detergent Micro 90, deionized water, acetone, and isopropanol sequentially for 10 min and oxygen plasma treated at 100 W for 15 min.

For the data shown in the main text we use spincoating in combination with antisolvent precipitation following [81]. The details are described in Section 2.2.1.

To investigate the influence of trap states, impurities, and morphological changes induced by different sample preparation methods, we prepared $MAPbI_3$ thin films with various methods, namely spincoating with and without antisolvent precipitation, solution casting, and two-step dipping (lead iodide (PbI_2) used as lead precursor for all methods mentioned above) and spincoating using lead acetate ($PbAc_2$) as lead precursor. All operations were performed in a nitrogen-filled glovebox unless specified. All PL

measurements were performed under the same experimental condition as described in the main text unless mentioned specifically.

For spincoating with antisolvent precipitation, the procedure was described in Section 2.2.1. We repeat the preparation method described in the main text to estimate the sample-to-sample variation. Additionally, we prepare the same sample in air without changing other parameters.

For solution casting, 100 µL of hot (100 ºC) MAPI solution (37 %, wt.) in DMF with a molar ratio of 1:1 between PbI_2 and MAI was deposited on top of fused silica substrate that was placed on a hotplate at 100 ºC under nitrogen atmosphere for 30 min.

For using $PbAc_2$ as lead precursor, $PbAc_2$ and methylammonium iodide (MAI) were dissolved in DMF with a molar ratio of 1:3 at 100 °C to obtain a 1M solution of MAPI. The solution was then spincoated onto fused silica substrates at 2000 rpm for 45 seconds. Then the sample is left to dry at room temperature for 10 min. The dried sample was transferred to a hotplate and annealed at 100 °C for 10 min.

For the two-step dipping method, we prepare a PbI_2 solution by dissolving PbI_2 (Sigma Aldrich, 99.999 %) in DMF by stirring it at 70°C overnight. The PbI_2 solution was filtered through a 0.2 µm PTFE filter to obtain a clear solution. This PbI_2 solution was spun on a pre-heated (50 °C) silica slide at 4000 rpm for 5 s. The PbI_2 covered slide was then dipped in 15 ml of homemade MAI solution (10 mg/ml in IPA) for 10 min. After 30 s a black film, consisting of micron sized crystallites (see Figure 2.16), is formed.

Hydrostatic pressure was generated through a pressurizing liquid Fluorinert FC-72 (3M) inside a high pressure cell (ISS Inc.) using a manual pump. The pressure was first applied from ambient pressure to 400 MPa (pressure upstroke) and then down from 400 MPa to ambient pressure (pressure downstroke), both in steps of 25 MPa. A 5-7 min waiting step after application of pressure and before the measurement was chosen to allow the material to equilibrate under pressure. The pressure liquid FC-72 started to scatter a fraction of light from 300 MPa onwards (flat spectral response, see inset Figure 2.2), which we corrected for in the absorbance spectra. The PL spectra and lifetimes were unaffected. From the measurement-to-measurement variability we estimate the upper limit on the error of the pressure reading (following the 5-7 min waiting step) to be 20 MPa.

Scanning electron microscope images were taken with a FEI Verios scanning electron microscope. The acceleration voltage was set to 15 kV and the sample current was set to 100 pA. The working distance was set to 4.1 mm. The images were generated via collecting secondary electron signals using a Everhart-Thornley type detector.

Absorbance spectra of MAPI thin films were measured with a LAMBDA 750 UV/Vis/NIR Spectrophotometer (Perkin Elmer) from 550 nm to 850 nm. A correction of the absorption spectra was done for all the spectra obtained above 300 MPa by subtracting the

background signal from scattering in the liquid. The background was obtained from a fit in the region of 820 nm to 850 nm where MAPI does not absorb.

Steady-state photoluminescence (PL) was measured with a home-built setup equipped with a 640 nm continuous-wave laser as source of excitation (PicoQuant LDH-D-C-640) at a power output of 0.7 mW. The PL spectra were collected at an angle of 45°. Two Thorlabs FEL-700 highpass filters were used to remove the excitation laser from the signal. The PL was coupled in a fiber connected to a OceanOptics USB4000 spectrometer, set to an integration time of 2000 ms for each measurement. The PL spectra were fitted with either one or two Voigt profiles (see Section 2.5.1).

Time-correlated single photon counting (TCSPC) measurements were performed with a home-built setup equipped with PicoQuant PDL 828 "Sepia II" and a PicoQuant HydraHarp 400 multichannel picosecond event timer and TCSPC module. A 640 nm pulsed laser (PicoQuant LDH-D-C-640) with a repetition rate of 5 MHz was used as source of excitation and a single-photon avalanche diode (SPAD) detector (Micro Photon Devices, MPD-5CTD) was used for the detection of photoemission. A Thorlabs FEL-700 longpass filter was used to remove the excitation laser. The TCSPC data was collected over the course of 60 seconds per measurement.

The photoluminescence quantum yield (PLQY) measurement was performed with a home-built setup. A supercontinuum laser (Fianium WL-SC-390-3) was fiber coupled into an acousto-optical tunable filter (AOTF), which has a visibile output for wavelengths 400-750 nm. A Mitutoyo objective focused the light on the sample inside the integrating sphere. Light inside the integrating sphere is monitored by the integrating sphere photodetector. The incident intensity was controlled by the AOTF RF power. Thorlabs PDA100 calibrated photodiodes were used as photodetectors. The acousto-optical tunable filter (AOTF) output was modulated with a 50 percent duty cycle at 3kHz. The absorption and photoluminescence measurements were done with Thorlabs FELH0650 and FESH0650 long pass and short pass filters, and the excitation wavelength was 600 nm.

First-principles materials modelling was employed to assess the bulk response of the electronic structure to external pressure. Calculations were performed by our collaborator, Prof. Aron Walsh from Imperial College London, within the Kohn-Sham Density Functional Theory (DFT) formalism as implemented in VASP [110]. Projector-augmented-wave core potentials were combined with a kinetic energy cutoff of 600 eV for the plane wave basis set describing the valence electrons including spin-orbit coupling. A scalar-relativistic description of Pb[Xe] was used with the 5d semi-core electrons included as valence. The phonon-stable crystal structures reported previously [111] were taken as the starting point for a series of isobaric calculations with a stress tensor ranging from 0 to 500 MPa. A positive bandgap deformation was found (bandgap decrease with increasing pressure) in agreement with initial calculations31. No attempt was made to model the phase change above 325 MPa, which would require sampling changes in spatial and temporal structural disorder.

2.5. SUPPLEMENTARY INFORMATION

2.5.1. FITTING OF STEADY-STATE PL SPECTRA

Steady state PL spectra are measured as function of wavelength. For a quantitative analysis of the data, a Jacobian transformation of the spectra to an energy scale was performed following literature [112]. The PL spectra are best fitted with Voigt profiles [113], which include the contributions from both Gaussian and Lorentzian components. The Voigt profile is given by

$$P(x,y) = \frac{1}{\omega_G}\sqrt{\frac{ln2}{\pi}}K(x,y) \tag{2.1}$$

Where $K(x,y)$, the so-called "Voigt function", is given by

$$K(x,y) = \frac{y}{\pi}\int_{-\infty}^{+\infty}\frac{exp(-t^2)}{y^2+(x-t)^2}\,dt \tag{2.2}$$

with $x = \frac{\nu-\nu_0}{\omega_G}\sqrt{ln2}$, $y = \frac{\omega_L}{\omega_G}\sqrt{ln2}$ and where ω_G and ω_L are the half widths of the Gaussian and Lorentzian components respectively, ν is the wave number, and ν_0 is the wave number at the line center.

The goodness of fit is evaluated by adjusted R squared (also known as coefficient of determination). Fits with adjusted R squared between 0.95 – 1.00 are considered to be "good" fits and all the Voigt fits for PL spectra fulfill this criterion. We define our error in the peak position as the standard errors of the Voigt fit.

The Voigt profile shape is chosen because it (a) offers the best description of the data since the emission broadening is a combination of homogeneous (Lorentzian) and inhomogeneous (Gaussian) broadening [114, 115] and (b) is the most general curve shape, as it is a convolution of Gaussian and Lorentzian line shapes.

2.5.2. ESTIMATION OF PHONON ENERGY

The phonon momentum can be calculated by assuming two parabolic bands that have a 60 meV difference from the k=0 point and the band edge. The curvature of the parabolic bands is determined by the effective masses, taken from literature [85]. The resulting wave vector is k= 0.048 $Å^{-1}$. This value is comparable to k of 0.05 $Å^{-1}$ from literature [80]. To calculate the energy of an acoustic phonon with this wave vector we use the phonon dispersion relation [116]:

$$\omega = 2\sqrt{\frac{\gamma}{M}}|\sin(ka/2)| \tag{2.3}$$

where ω is the angular frequency, γ is the force constant, M is the mass of the unit cell, k is the phonon wave vector, and a is the lattice constant.

The force constant γ is connected to Young's modulus Y and the lattice parameter a via $\gamma = Y \times a$. The Young's modulus was derived from the phonon dispersion relation in literature [117] and found to be Y=(13 ± 2) GPa. The lattice parameter is a=6.4 Å [118]. The mass of the unit cell is the sum of all unit cell constituents. These values lead to a phonon energy of 0.6 meV, for a phonon with momentum such that the indirect transition can occur.

2.5.3. MODELLING OF PHOTOTHERMAL DEFLECTION SPECTROSCOPY (PDS) DATA

To fit the photothermal deflection spectroscopy data, we use equations for the direct bandgap, the indirect bandgap, and the Urbach tail. We extracted the absorption data for MAPI from [96] using the website (http://arohatgi.info/WebPlotDigitizer/) (Figure 2.7). As above, the data was then linearized according to the Tauc rule for both direct and indirect bandgaps:

$$\alpha h\nu = A(h\nu - E_G)^r \tag{2.4}$$

with the absorption coefficient α, photon energy $h\nu$, the scaling constant A, the bandgap energy E_G and the coefficient r (r = 2 for indirect allowed transition, r = ½ for direct allowed transition) [119, 120]. Then the linear region of the plot is identified and a straight line is fitted (with Mathematica using LinearModelFit) (Figure 2.7). The beginning of the absorbance can be fitted separately with an exponential, the Urbach tail, usually assigned to shallow traps and Gaussian disorder [121]. The Urbach energy we extract is 21 meV, comparable to the 15 meV measured before [96, 98].

The dashed lines depict an attempt of fitting the whole bandedge with only a direct bandedge and an Urbach tail. The fit with only a direct bandgap does not describe the data well, with non-Gaussian distributed residuals, which led us to the conclusion that an indirect bandgap is also supported from PDS absorption data.

2.5.4. DETERMINATION OF PLQY

We used an integrating sphere setup to estimate the photoluminescence quantum yield of the identical MAPI film used in the main text. We determine the absorbed power and the luminescence directly, by using a photodetector combined with a long-pass filter (for photoluminescence). The experimental approach is based on an experimental setup described by Mann et al. [122], inspired by Leyre et al. [123]. Here, the absorptance A is determined as:

$$A = 1 - \frac{P_{hit}}{P_{miss}} \tag{2.5}$$

where P_{hit} and P_{miss} are the power on the integrating sphere photodetector behind a short-pass filter, when the beam hits or misses the sample, respectively. The photoluminescence is determined by repeating the measurement, but now with a long-pass

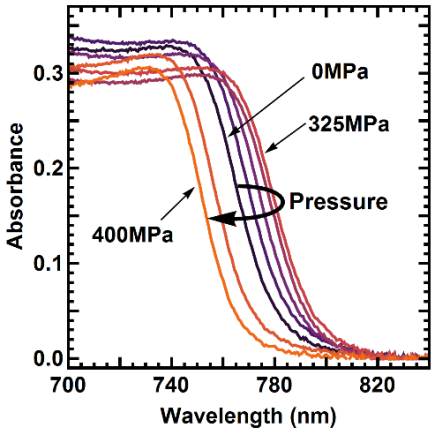

Figure 2.13: Complete set of absorption spectra of MAPI under pressure

filter. Using a calibrated photodiode the collection efficiency of the integrating sphere and the excitation power are determined, which allows us to determine the PLQY:

$$PLQY = \frac{P_{PL}}{CA} \tag{2.6}$$

where P_{PL} is the photodetector signal due to photoluminescence, and C is the collection efficiency calibration factor.

The excitation power is varied by modifying the transmission of an acousto-optic tunable filter (see below), while the normalization to suns is performed by converting the incident power to a power density. The area of the spot is determined using a knife edge measurement, and the incident flux density is normalized to the above band gap photon flux in the solar spectrum.

The errorbars are due to systematic and random errors. The systematic error is estimated from a calibration measurement on R6G+ dye and is 9 % rel., while the random error is only significant at low intensities.

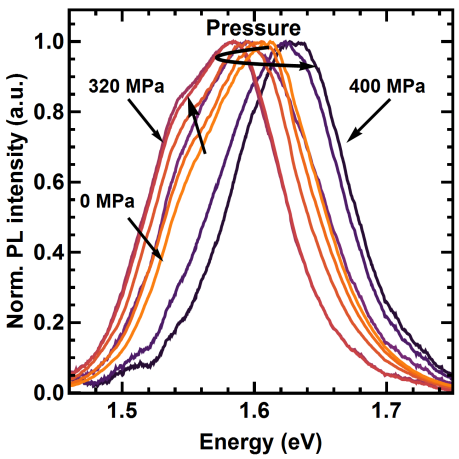

Figure 2.14: Complete set of PL spectra of MAPI under pressure

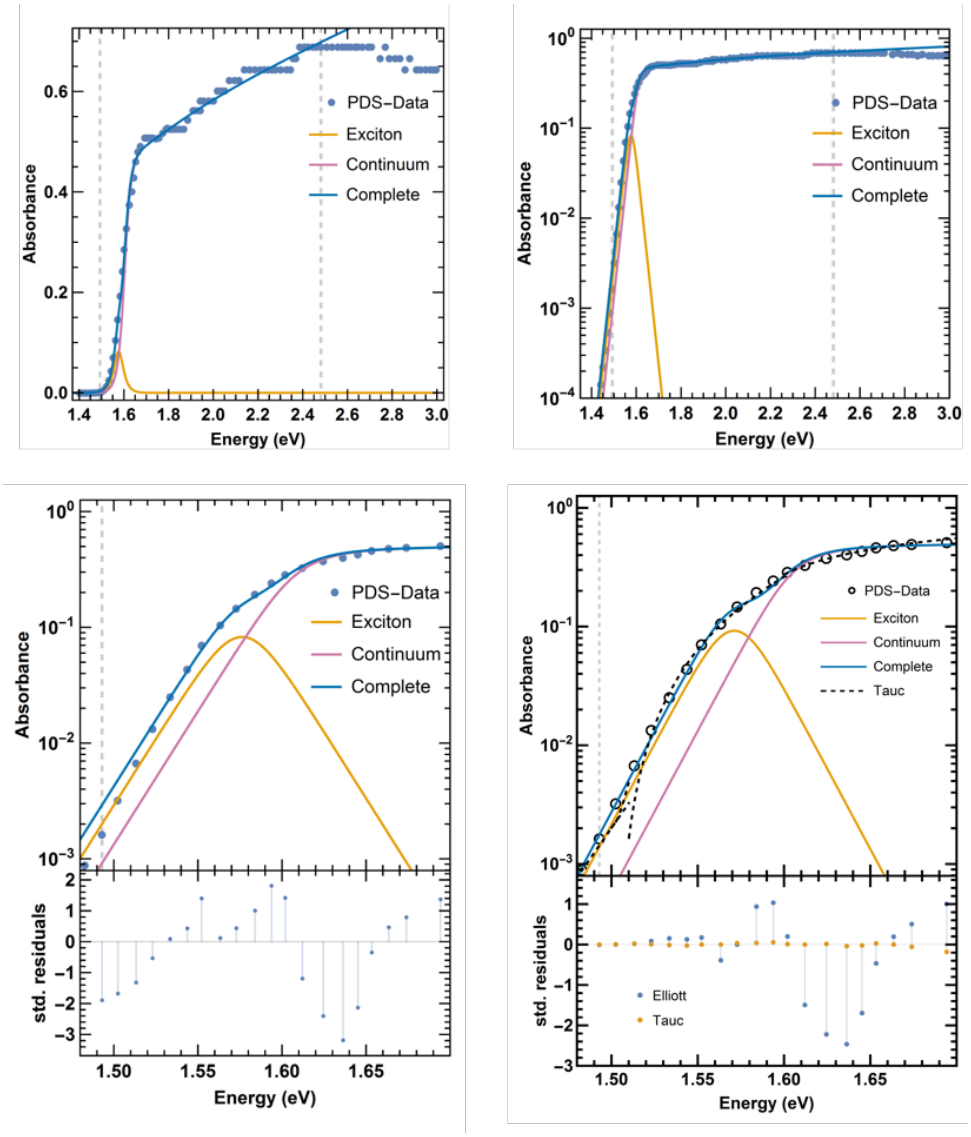

Figure 2.15: Comparison of Tauc fit and Elliott fit on PDS data of Sadhanala et al.. Left Top: Best Elliott fit with data in between dashed lines as produced by fitting with Mathematica. Right Top: The same fit as before, on a log scale. Left Bottom: Zoom in the data of the band edge. The residuals shown in the bottom panel are larger than in the Tauc fit. Right Bottom: Manually improved fitting of band edge. The band edge can be fitted better by decreasing the broadening parameter from 19 meV to 16 meV. Fitting the remaining parameters results in the blue fit,

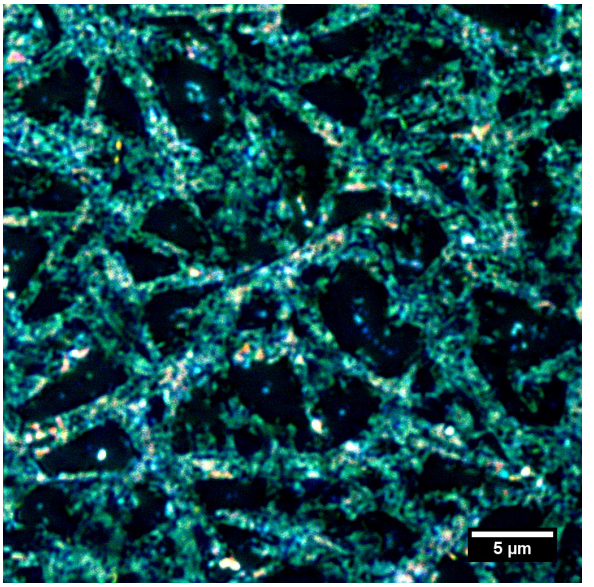

Figure 2.16: Optical micrograph of MAPI sample prepared via two-step dipping method.

3

PHOTOPHYSICS IN TWO-DIMENSIONAL LEAD HALIDE PEROVSKITES: A PRESSURE STUDY

Two-dimensional (2D) lead halide perovskites are emerging as promising light emitting materials due to their quantum confined electronic structure. Understanding the steady-state optical properties and exciton dynamics in 2D perovskites is important for improving the emission efficiency of the materials and the performance of light emitting devices. Here we study the changes in photophysics upon application of pressure. Most of the compression is absorbed in the organic spacer lyaer, changing the quantum confinement for the short spacers. We also study the Rashba splitting in 2D perovskites We find that the steady-state response of 2D perovskites to pressure strongly depends on the length of the organic spacer. Time-resolved optical measurements under pressure reveal no evidence for Rashba splitting in monolayer 2D perovskites. We propose studies on multilayer 2D perovskites under pressure for a more comprehensive understanding of Rashba splitting in 2D perovskites.

3.1. INTRODUCTION

The emergence of lead halide perovskites in recent years has shown the great potential of this type of material for optoelectronic applications. Alongside with the rapid growth in efficiency of the perovskite solar cells, where the perovskites are used as light absorbers, there are also growing interests in exploiting perovskites as light emitters for applications such as light emitting diodes (LED) and lasers. For these applications, where efficient recombination of charge carriers is needed, the variations of perovskites that have a lower dimensionality, two-dimensional (2D) perovskites, have sparked interest of researchers because of the stronger confinement of the charge carriers in these systems. Unlike the 3D perovskites, where the lead-halide cages are interconnected in a three-dimensional manner, 2D perovskites consist of mono- or multi-layers of lead halide cages which are spatially separated by organic spacers. LEDs with high external quantum efficiency have been demonstrated using 2D perovskites or a combination of 2D/3D perovskites [12, 124]. Broadband white-light emission has also been discovered in a variety of 2D perovskites [18, 125–127]. Besides the great optoelectronic properties, the 2D perovskites and the 2D/3D mixtures show an increased stability compared to the pure 3D perovskites, which is normally ascribed to a better passivation at the grain boundaries [128, 129].

While the device efficiency is advancing, there is still a lack of clear understanding of the fundamental aspects of the photophysics in 2D perovskites, especially the structure-property relationship, which is important for further improvement in materials and devices. As we have shown experimentally in Chapter 2, a Rashba splitting at the band extrema, induced by strong spin-orbit coupling, may be existent in the prototypical 3D perovskite methylammonium lead iodide. We have also shown that the degree of Rashba splitting can be tuned via the application of external pressure and the changes in Rashba splitting can have huge impact on the dynamics of charge carriers. Since the building blocks of 2D perovskites are still lead halide cages, it is of interest to see whether the Rashba effect is also existent in 2D perovskites despite the layered structure which is different from the 3D analogs. If 2D perovskites show Rashba splitting, we need to understand how the structural changes influence the degree of Rashba splitting and the photophysical properties of 2D perovskites, to utilize the tunability via the structural degree of freedom. Several reports have shown theoretical and experimental evidence of Rashba splitting in 2D perovskites [130, 131]. Yin et al. showed that for 2D perovskites separated by PEA ligands, the n=1 layer perovskite should show no significant Rashba splitting, while the n=2 material should. Similarly, n=3 layers should show no Rashba splitting [131]. This difference arises because of the different tilting angles of the Pb-I bond, which is 180 ° for n=1, 174.0° and 172.5° for n=2 and 176.3° and 177.3° for n=3. This means that the n=2 variant shows a stronger tilting, leading to breaking the inversion symmetry around the lead atom, which ultimately leads to the Rashba effect.

Since the symmetry of the lead-halide cages can be tuned with pressure, we hypothesize that we should see a difference in the pressure response of the n=1 and n=2 2D perovskites. With the increased pressure the angle between the octahedra of both sys-

tems should be close to 180°, leading to a diminished Rashba splitting. For that comparison, however, we first need to fully understand the photophysical behavior of the n=1 perovskite, where we expect no changes relating to Rashba splitting under pressure, because there is already zero tilt at ambient pressure.

In this chapter we study the photophysics of two types of n=1 2D perovskites under hydrostatic pressure, namely hexylammonium lead iodide (HA_2PbI_4) and dodecylammonium lead iodide (DA_2PbI_4) and perform steady-state and time-resolved optical measurements to track the changes in charge carrier dynamics under pressure. These materials have two ligands of very different length, and we expect the ligand spacer layer to be softer under compression compared to the inorganic 2D sheets. Comparing the two materials allows us to distinguish the effect of ligand compression from halide cage tilting. In addition, these 2D perovskite variants have shown white-light emission at low temperature, and because under pressure perovskites behave somewhat similar as under low temperature, pressure might provide a good probe to better understand the white-light emission.

We find that the ligands induce significant differences in the behavior under pressure. For the shorter (HA) ligands, we see a red-shift of the absorption and emission energy, assigned to a weaker confinement of the excitonic wavefunction, while the wavefunction in the perovskite with long DA ligands remains confined even at high pressure. As predicted, we see no evidence for the Rashba splitting in the n=1 perovskite, and, as a result, no changes under pressure in the dynamics after photoexcitation. Our results also strongly suggest that most of the deformation under pressure is in the ligands, and that the lead iodide octahedra remain relatively uncompressed. We see no white-light emission under pressure, confirming that the lead iodide octahedra are largely unaffected by pressure. Finally, we point towards experiments with n=2 and n=3 layer perovskites, and lay out the remaining challenges towards studying Rashba splitting in 2D perovskites.

3.2. RESULTS AND DISCUSSIONS

3.2.1. ABSORPTION OF HA_2PbI_4 AND DA_2PbI_4 UNDER PRESSURE

The absorption spectra of HA_2PbI_4 and DA_2PbI_4 thin films prepared via one-step spin-coating (see Section 3.4 for details) under pressure up to 400 MPa are shown in Figure 3.1. Strong excitonic features are present in both materials in the absorption spectra, which is a result of strong quantum confinement induced by the spatial separation of lead iodide octahedra. The absorption of DA_2PbI_4 at ambient pressure is blue-shifted with respect to that of HA_2PbI_4, which can be understood as a result of stronger quantum confinement effect induced by the longer length of the DA spacer. The absorption of HA_2PbI_4 shows a continuous red-shift of around 40 meV under pressure up to 400 MPa, while the absorption spectra of DA_2PbI_4 remain static despite increasing pressure. Below we discuss the possible origin of the different response of the two materials under pressure.

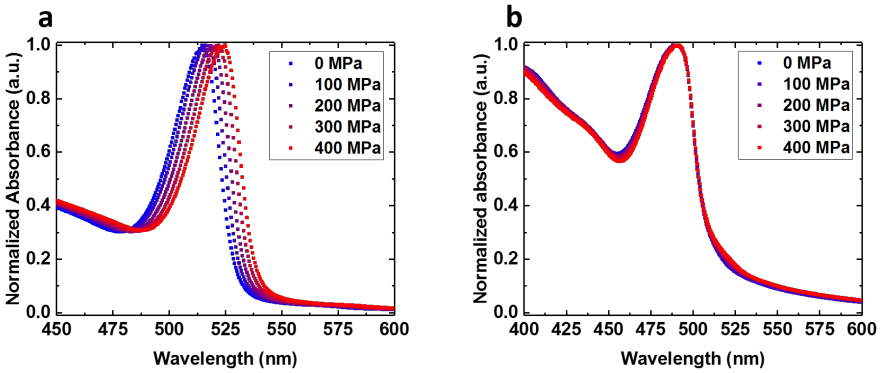

Figure 3.1: Absorption spectra of (a) HA_2PbI_4 and (b) DA_2PbI_4 under pressure.

The wavefunction in the 2D perovskite sheets is highly confined to a single layer of PbI_6 octahedra. This confinement leads to a strong blue-shift of the bandgap as compared to the 3D perovskite, and a discretization of the electronic levels, leading to a strong excitonic absorption and emission spectrum [132]. By applying pressure, we find that the absorption spectrum red-shifts. This shift is consistent with a partial release of the confinement, by a narrower distance between the 2D sheets. The wavefunction can tunnel partially into the next layer, leading to a weaker effective confinement, similar as in quantum dots, where the spacing between individual dots, induced by surface ligands, also has influence on the confinement [133].

The DA ligands (12 C-atoms) pose a larger distance between the perovskite sheets compared to the HA ligands (6 C-atoms). As a result, the wavefunction is more confined, leading to an even more blue-shifted bandgap. Under pressure we observe no changes in the absorption spectrum, suggesting that even under compression, the spacer layer between the perovskite sheets is large enough to prevent any leakage of the wavefunction into the neighboring layers.

3.2.2. STEADY-STATE PHOTOLUMINESCENCE OF HA_2PbI_4 AND DA_2PbI_4 UNDER PRESSURE

The steady-state photoluminescence (PL) spectra of HA_2PbI_4 and DA_2PbI_4 under pressure are shown in Figure 3.2. Both films show asymmetric PL line shape, which might be a result of self-absorption due to the relatively large thickness of the films. Like in absorption, the PL of DA_2PbI_4 at ambient pressure is blue shifted with respect to that of HA_2PbI_4, again confirming a higher degree of quantum confinement in DA_2PbI_4. The PL spectrum of the HA perovskite shows a similar continuous shift in the emission spectrum as in the absorption spectrum under pressure. This indicates that, besides the release of confinement, no other effects play a significant role for the emission energy. At high pressure the peaks become slightly narrower, indicating changes in the electron-phonon

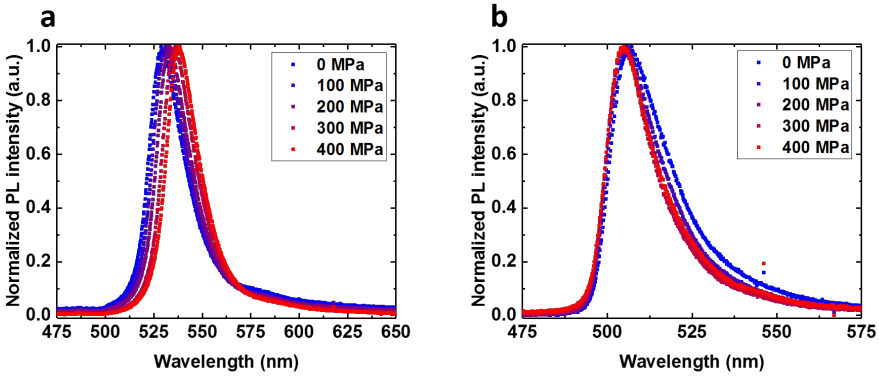

Figure 3.2: Steady-state photoluminescence spectra of (a) HA_2PbI_4 and (b) DA_2PbI_4 under pressure.

coupling [134]. The DA perovskite shows again no shift in the bandgap at elevated pressure. This is consistent with the absorption spectrum, and again shows that the compression in this case is mostly absorbed in the long DA ligands. At higher pressure, the peak width does become significantly narrower, with a strong reduction of emission at the red end of the peak. This may indicate that under high pressure, some lower-energy states (e.g. shallow trap states, disordered phases) cannot be accessed any more.

The HA and DA perovskites have shown to emit white light at low temperatures (< 100 K). This broad emission has been assigned to emission via sub-bandgap defect states, either an interstitial of iodide, or iodine related Frenkel defect states [127] . In previous experiments we could show that high pressure has a similar effect on the band structure as low temperature [91, 135], yet without changing the temperature and therefore the phonon bath. It would therefore be interesting to observe the defect emission at high pressure and room temperature. As apparent from Figure 3.2, we cannot observe the white-light emission at high pressure <400 MPa. This, again, is consistent with the picture that the lead-halide cages do not significantly strain when surrounded by soft organic ligands. For 2D lead bromide perovskites, white-light emission has been observed at much higher pressures (> 4 GPa), where presumably also the cages distort [136].

3.2.3. PHOTOLUMINESCENCE LIFETIME OF HA_2PbI_4 AND DA_2PbI_4 UNDER PRESSURE

To study the existence of Rashba splitting, we study the dynamics of the excited states in the 2D perovskites. For 3D $MAPbI_3$, the dynamics become faster at high pressure, and the emission more efficient, consistent with a reduction in Rashba splitting. Here, we study the 1-layer perovskite, where we do not expect Rashba splitting, so we would expect no changes related to the splitting in the dynamics at high pressure. The PL decay curves of HA_2PbI_4 and DA_2PbI_4 thin films under pressure are shown in Figure 3.3. Both materials show a faster decay compared to the 3D perovskites, suggesting the excitonic

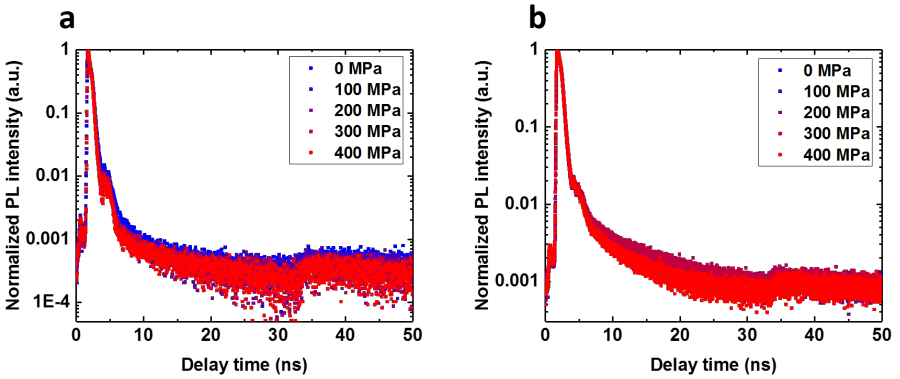

Figure 3.3: PL decay curves of (a) HA_2PbI_4 and (b) DA_2PbI_4 under pressure.

nature of the 2D perovskites, i.e. the high binding energy between the electron and the hole, accelerates the recombination of the electrons and the holes. The changes in PL lifetime of both materials under pressure seem to be minimal. As the electronic structure of perovskites are located mainly within the lead-halide octahedra, no change in the recombination dynamics might indicate that there are limited changes in the lead halide octahedra, consistent with the picture that the compression mainly takes place in the ligands.

If there were Rashba splitting in these perovskites, however, we would expect a change in the decay dynamics, even at low compression values. For example, for $MAPbI_3$ we observed a change in the dynamics already at 50 MPa [135]. Here, we see no changes, consistent with no Rashba splitting in the n=1 perovskites.

3.2.4. TRANSIENT ABSORPTION OF HA_2PbI_4 UNDER PRESSURE

To make sure that the fast dynamics that we see in the PL decay curves are not dominated by the instrument response, we exploit transient absorption (TA) spectroscopy as a tool with higher time resolution (fs to ps) to probe the ultrafast exciton dynamics under pressure. Also, with TA, all excited states become visible, not only the emissive ones. Thus, with TA we can get insights into the broad trap state distribution that has been attributed to the origin of the white-light emission.

The TA spectra of HA_2PbI_4 at ambient pressure and 400 MPa are shown in Figure 3.4. Note that the spectra are not corrected for the dispersion throughout the optical path, leading to a shift of the pump-probe delay with wavelength, as apparent from the shift in the onset of the TA signal. At ambient pressure, a sharp photo-induced absorption (PIA) and ground state bleach (GSB) feature is observed around the band edge of HA_2PbI_4, while a broad PIA feature is observed from 560 nm to 700 nm (Figure 3.5). With increasing pressure, the sharp PIA and the GSB red-shift, consistent with the changes

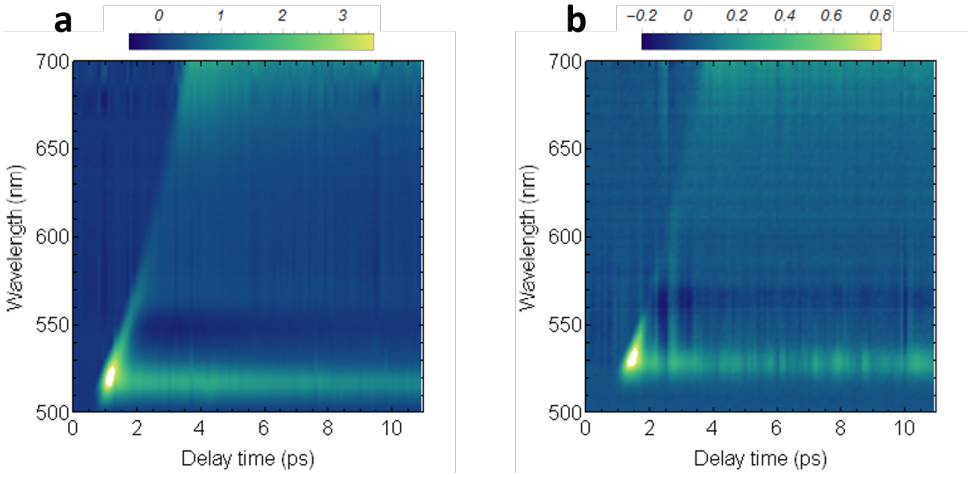

Figure 3.4: 2D transient absorption map of HA_2PbI_4 (a) at ambient pressure and (b) at 400 MPa. The scale of the colorbar is 10^{-2}.

that we observe in steady-state measurements. The reduction in signal intensity might be related to the scattering from the pressure liquid at high pressure.

The sharp PIA feature lies close to the band-edge, and it was previously shown that the dynamics of this PIA feature coincide with the dynamics of photoluminescence [127]. We find that the decay consists of two timescales, a fast decay of 0.3 ps, and a longer decay with a time constant of 7.0 ps (Figure 3.6). In the PL lifetime we can only observe the longer decay. Note that the TA spectra were taken at much higher light intensity, making a comparison of the absolute time constants difficult.

The very fast decay indicates a fast de-population of the exciton, within 1 ps. We find that the broad PIA feature does grow in on the same timescale (Figure 3.7). Also, the broad PIA feature lives longer than the sharp PIA. Both observations are consistent with a picture of fast trapping of the initial exciton population into a broad distribution of trap states. We therefore assign the broad PIA to induced absorption from a broad trap distribution. We further hypothesize that this broad trap state distribution is the same distribution that is responsible for the white-light emission at low temperature.

At elevated pressure we find that the trapping timescale and magnitude does not change. However, the decay of the trap population becomes slower at high pressure. This indicates that the high-pressure regime is somewhat closer to the low temperature regime, with a more stable trap population. We note, however, that the emission does not show white light, which shows that even at high pressure, we are far from the regime of low-T (<100 K) emission.

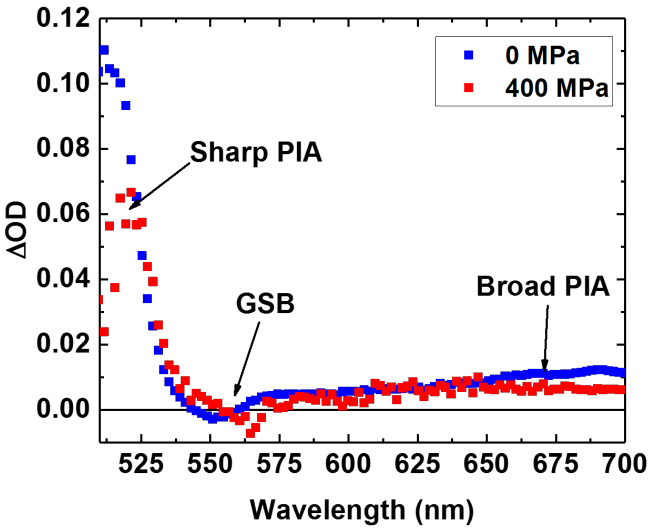

Figure 3.5: TA spectra of HA_2PbI_4 at 1 ps after excitation at ambient pressure and 400 MPa

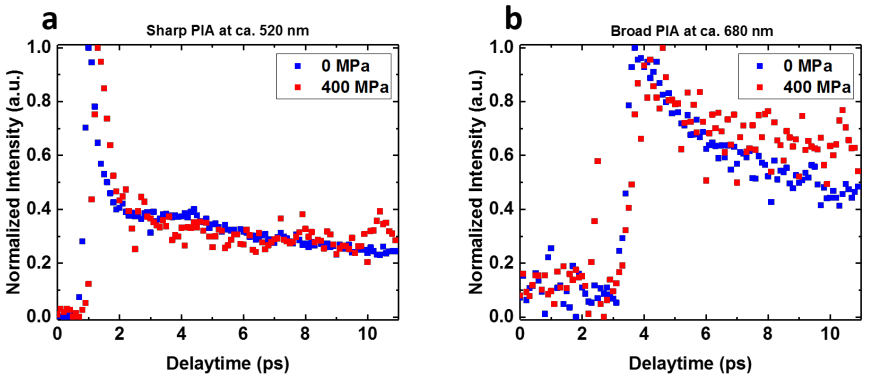

Figure 3.6: TA dynamics of (a) band-edge exciton and (b) trap states in HA_2PbI_4 at ambient pressure and at 400 MPa

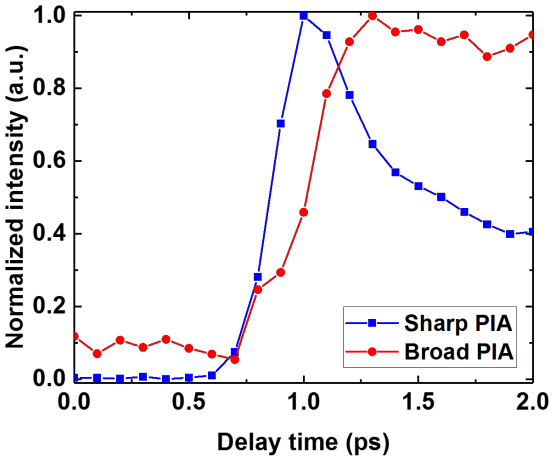

Figure 3.7: TA dynamics of band-edge exciton and trap states in HA_2PbI_4 at ambient pressure.

3.3. CONCLUSIONS AND OUTLOOK

In conclusion, we performed steady-state and time-resolved optical measurements on two 2D perovskites with different organic spacer length, namely HA_2PbI_4 and DA_2PbI_4 under hydrostatic pressure. From the steady-state absorption and PL measurements, the two materials show very different response to external pressure. For HA_2PbI_4, the absorption and PL spectrum continuously red-shift under pressure up to 400 MPa, which can be understood as a result of relaxation of quantum confinement. The shift in the absorption and PL spectra of DA_2PbI_4 is minimal until 400 MPa, which is presumably due to the compression of the spacer layer between the perovskite sheets being not large enough to cause the release of the quantum confinement. We do not observe white-light emission within the pressure range that we can reach, suggesting a much higher pressure might be needed to access the low-temperature regie of white-light emission. From the PL lifetime measurements, we do not observe significant change in the decay rate in either material, which indicates that the lead iodide octahedra are not significantly compressed or tilted, leading to no changes in the Rashba splitting, or that there is no Rashba splitting in the first place (as predicted from theory). We identify the photo-induced absorption of both the band-edge excitons and the trap states from the transient absorption measurements. The fast decay of the band-edge excitons coincides with the rise of the trap states PIA. Under pressure, the decay of the band-edge excitons remains unchanged, while the decay of the trap population becomes slower at high pressure, which could be an indication of the initialization of the trap states emission. Our results show that Rashba splitting is not present in the monolayer 2D perovskite HA_2PbI_4 and the degree of quantum confinement can be manipulated by change the interlayer distance via external pressure.

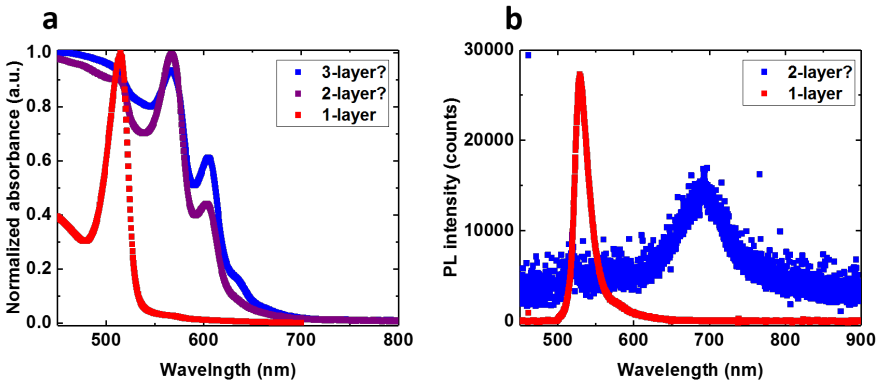

Figure 3.8: (a) Absorption and (b) PL of mono- and multi-layer 2D perovskites at ambient pressure

As Yin et al. have shown, Rashba splitting in PEA-terminated 2D perovskites could be dependent on the number of layers per sheet [131]. It is therefore interesting to see whether the layer thickness-dependence of Rashba splitting also applies in 2D perovskites with other spacers, and if it can be manipulated by pressure. We have attempted the synthesis for bilayer and trilayer 2D perovskites with HA ligands, by mixing methylammonium iodide and hexylammonium iodide in stoichiometric ratio in the precursor solution. However, the absorption spectra of the films suggest that a mixture of different thicknesses is present, rather than a homogeneous material of a monodisperse layer thickness (Figure 3.8). The PL measurements shows that the emission efficiency in the obtained films is drastically reduced compared to the monolayer 2D perovskites, and also strongly red-shifted, suggesting energy transfer to the thickest part of the material, which has the lowest quantum confinement. To have a cleaner system for the study on the layer thickness-dependence of Rashba splitting, films with better purity need to be prepared. For the study under pressure, the choice of spacer, especially the length of the spacer, is of great importance. A balance between the compression of the interlayer distance and of the lead halide octahedral needs to be considered. Also DFT calculations for the mono- and multi-layer 2D perovskites under pressure will help to understand the experimental observations.

3.4. METHODS

Sample preparation: HA_2PbI_4 and DA_2PbI_4 thin films were prepared via one-step spin-coating of a precursor solution. Two portions of 0.46 g of lead iodide (99 %, Sigma Aldrich) were first separately dissolved in 1 mL of anhydrous n-dimethylformamide (DMF) under continuous stirring at 100 °C to form a 1M solution. Then 0.46g of hexylammonium iodide and 0.62 g of dodecylammonium iodide (98 %, GreatCell Solar) were separately added into the lead iodide solution to form the stoichiometric ratio of 2:1 between the organic spacers and the lead iodide. The solution is then kept stirring at 100 °C un-

til all precursors are fully dissolved, which is indicated by a translucent yellow solution. Fused silica substrates are subsequently cleaned in ultrasonic bath with Alconox detergent, DI water and acetone for 15 min, rinsed with isopropanol and treated in oxygen plasma at 100 W for 15 min. The precursor solution was then spin-coated onto the precleaned fused silica substrates at 2000 rpm for 30 s. The substrates were transferred to a hotplate after spin-coating and annealed at 100 °C for 10 min.

For the trial on multi-layer 2D perovskites, a solution that contains only hexylammonium iodide and lead iodide was first prepared. Methylammonium iodide was later added in stoichiometric ratio into the solution to avoid formation of three-dimensional perovskites. The thin films were then prepared following the same procedure mentioned above.

Hydrostatic pressure was generated through a pressurizing liquid Fluorinert FC-72 (3M) inside a high pressure cell (ISS Inc.) using a manual pump. The pressure was first applied from ambient pressure to 400 MPa (pressure upstroke) and then down from 400 MPa to ambient pressure (pressure downstroke), both in steps of 100 MPa. A 5-7 min waiting step after application of pressure and before the measurement was chosen to allow the material to equilibrate under pressure. From the measurement-to-measurement variability we estimate the upper limit on the error of the pressure reading (following the 5-7 min waiting step) to be 20 MPa.

UV/Vis absorption: Absorbance spectra of 2D perovskite thin films were measured with a LAMBDA 750 UV/Vis/NIR Spectrophotometer (Perkin Elmer) from 350 nm to 700 nm in steps of 0.5 nm. A correction of the absorption spectra was done for all the spectra obtained above 300 MPa by subtracting the background signal from scattering in the liquid. The background was obtained from a fit in the region of 650 nm to 700 nm where the samples does not absorb, and is typically lower than 10 %.

Steady-state photoluminescence: Steady-state photoluminescence (PL) of the samples was measured with a home-built setup, while HA_2PbI_4 was excited with a 485 nm laser (PicoQuant LDH-D-C-485) in continuous-wave mode and DA_2PbI_4 was excited with a 405 nm continuous-wave laser as source of excitation (S1FC405, Thorlabs) at a power output of 2 mW. The PL of the samples was coupled in a fiber connected to an OceanOptics USB4000 spectrometer, set to an integration time of 2000 ms for each measurement.

Time-correlated single-photon counting: Time-correlated single-photon counting (TCSPC) measurements were performed with a home-built setup equipped with PicoQuant PDL 828 “Sepia II” and a PicoQuant HydraHarp 400 multichannel picosecond event timer and TCSPC module. A 485 nm laser in pulsed mode (PicoQuant LDH-D-C-485) with a repetition rate of 20 MHz was used as source of excitation and a single-photon avalanche diode (SPAD) detector (Micro Photon Devices, MPD-5CTD) was used for the detection of photoemission. A notch filter at 488 nm and a 500 nm long-pass filter were used to filter out the excitation in the detection path. The TCSPC data was

integrated over 600 seconds per measurement.

Transient absorption: Transient absorption measurements were performed with a home-built setup equipped with a Ti:Sapphire laser (Coherent, 800 nm, 1 kHz, 35 fs, 6.35 W). The 800 nm fundamental laser was split into two parts to generate the pump (400 nm) using a Barium borate (BBO) crystal and the broadband probe using a sapphire plate. The time delay between the pump and the probe is controlled via a mechanical delay stage. TA spectra at each pressure is taken in steps of 0.1 ps. An averaging of 2500 spectra was done at each delay time to yield signal to noise ratio.

4

MODULATING SINGLET FISSION EFFICIENCY IN RUBRENE BY EXTERNAL HYDROSTATIC PRESSURE: A CLEAN WAY TO CHANGE INTERMOLECULAR ELECTRONIC COUPLING

Singlet fission, the conversion from one singlet exciton into two triplet excitons, may help to boost efficiencies of conventional solar cells. Electronic coupling between chromophores plays an important role for singlet fission, but has thus far only been varied by changing the material system. Here we vary electronic coupling in amorphous and crystalline rubrene by strain using hydrostatic pressure. Under pressure we perform ultrafast transient absorption measurements to probe the induced changes in the rate and efficiency of single fission. We show that pressure can increase singlet fission efficiency in amorphous rubrene close to unity by increasing electronic coupling between chromophores. In contrast, increased coupling slows down triplet pair dissociation in crystalline rubrene where the efficiency of singlet fission is not limited by the intermolecular electronic coupling. Under pressure the energetic barrier for triplet pair dissociation increases by 50 meV with increasing electronic coupling, which leads to slower dissociation of these triplet pairs. Our results show that singlet fission dynamics can be effectively tuned via external stress, and that both electronic coupling and energetic driving force must be considered for designing highly efficient singlet fission materials.

4.1. INTRODUCTION

Singlet fission in organic semiconductors is a promising and potentially inexpensive approach to surpass the Shockley-Queisser limit of single-junction solar cells [32]. By converting one singlet exciton into two lower-energy triplet excitons, singlet fission can down-convert the high-energy light in the solar spectrum with near-unity efficiency in material systems like pentacene [21] and 1,3-diphenylisobenzofuran [137]. Highly efficient triplet transfer into inorganic semiconductor nanocrystals [36, 37] and solar cells with over 100 % external quantum efficiency [33–35] have been demonstrated utilizing polyacenes, showing the great potential of singlet fission for photovoltaic applications.

Amongst many aspects that can have an impact on the rate and efficiency of singlet fission, electronic coupling between chromophores has proven to be a critical one. By studying a variety of materials that are capable of singlet fission, Yost et al. have demonstrated that the kinetics of singlet fission are strongly dependent on the strength of coupling between bright and dark states in the systems [138]. Tayebjee et al. studied covalently linked dimers of pentacene derivatives and found that the dissociation rate of the triplet pairs is affected by the length of the linkers [42]. Le et al. modified the functional groups of perylenediimides to change the displacement between chromophores and found that electronic coupling and energetics strongly depend on the displacement and both influence singlet fission efficiency [139]. Despite these insights on the influence of electronic coupling on singlet fission, they all rely on comparisons between different material systems, where the morphologies, energetics and entropic gains would also differ alongside electronic coupling. Therefore, a method that can disentangle electronic coupling from other parameters is needed to study how singlet fission will be affected by different degrees of electronic coupling in a specific material system.

In this study, we apply hydrostatic pressure on rubrene thin films as a clean method for tuning the intermolecular distance, which affects electronic coupling without changing the material system. Rubrene has been extensively studied for organic transistors [140] and organic light emitting diodes [141] due to its high hole mobility [141] and high photoluminescence efficiency [142]. Recently, there has been a growing interest in exploring the possibility of using rubrene for singlet fission [143–149] as the triplet energy of rubrene is around 1.14 eV [150], making it ideal for triplet transfer into crystalline silicon, which has a bandgap of 1.12 eV. Pressure has been used for studying optical [151], electrical [152] and structural [153] properties of rubrene crystals, thin films and devices. Yet, a clear understanding on how pressure-induced changes in intermolecular electronic coupling influences exciton dynamics, especially the rate and efficiency of singlet fission in rubrene, is missing.

To study the effect of electronic coupling on exciton dynamics, we perform steady-state and ultrafast optical measurements on amorphous and polycrystalline rubrene films under hydrostatic pressure up to 400 MPa. We observe increased electronic coupling for both amorphous and polycrystalline rubrene films under pressure. Singlet fission efficiency is enhanced in amorphous rubrene with increasing electronic coupling,

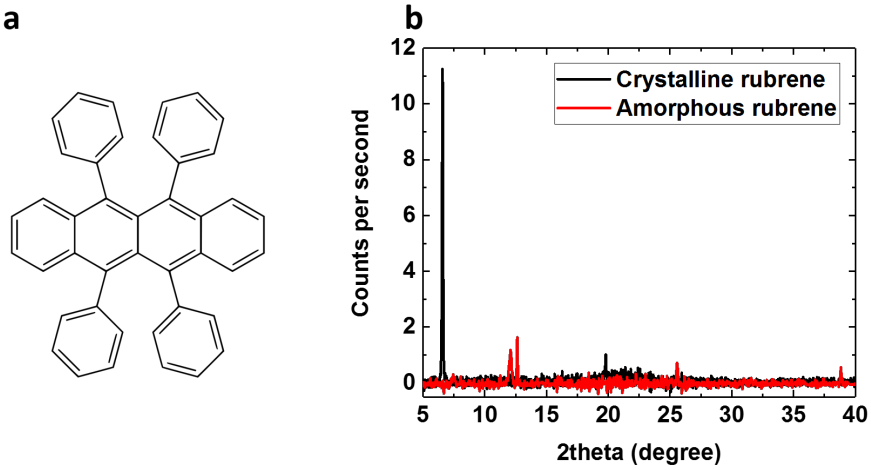

Figure 4.1: (a) Molecular structure of rubrene and (b) X-ray diffraction (XRD) spectra of crystalline and amorphous rubrene thin films

thanks to a more rapid formation of triplet pairs. In crystalline rubrene, the energy barrier between S_1 and $2T_1$ is higher with increasing electronic coupling, resulting in slower dissociation of triplet pairs. Our results provide insight for designing highly efficient singlet fission materials.

4.2. RESULTS AND DISCUSSIONS

4.2.1. SAMPLE PREPARATION

Amorphous rubrene thin films with a thickness around 100 nm are prepared via thermal evaporation on fused-silica substrates. To obtain a crystalline film, we followed a homoepitaxial method as is described in literature [154] (see Section 4.4.1 for details). A pronounced peak at 6.6 ° which corresponds to an orthorhombic structure is shown in x-ray diffraction spectra for the crystalline film, while it is missing for the amorphous film (Figure 4.1). The other, much less pronounced peaks presumably indicate short-range ordering.

4.2.2. STEADY-STATE ABSORPTION OF AMORPHOUS AND CRYSTALLINE RUBRENE UNDER PRESSURE

The films are immersed in the hydraulic liquid Fluorinert FC-72 to apply hydrostatic pressure up to 400 MPa to both amorphous and crystalline thin films. Figure 4.2 shows the UV-Vis absorption spectra of amorphous and crystalline rubrene films at ambient pressure and their evolution under pressure. The absorption spectrum of dilute rubrene solution in chloroform is shown in Figure 4.2a for comparison. Clear vibronic progres-

sions are visible for both amorphous and crystalline rubrene films. The absorption spectrum of the amorphous rubrene film shows a minor red-shift with respect to the solution spectrum, indicating a weak interaction between chromophores that leads to a slightly J-type aggregation and further confirming the amorphous nature of the film. The absorption of crystalline rubrene film is blue-shifted compared to the solution spectrum, while the transition strength of the 0-1 peak is higher than that of the 0-0 peak, indicating a H-type aggregation in the crystalline rubrene film [155]. With increasing pressure up to 400 MPa, absorption spectra of both amorphous and crystalline rubrene films show continuous red-shifts (Figure 4.2b and 4.2c) along with a broadening of the 0-0 peaks (Figure 4.2d). The red shifts and broadening of absorption peaks can be attributed to a stronger polarization effect [19] under pressure due to the reduction of intermolecular distance, indicating an increasing electronic coupling between chromophores. A red-shift of 15 meV is observed for the 0-0 vibrational peak of amorphous rubrene, while the 0-0 vibrational peak of crystalline rubrene red-shifts by 30 meV when the pressure is increased to 400 MPa (Figure 4.2e). Presumably, the increasing polarization under pressure is partly compensated by the higher degree of pi stacking between chromophores in amorphous rubrene under pressure. This increase in pi stacking is evident by the higher ratio between the transition strength of 0-1 and 0-0 vibrational peaks [155], and the increasing absorption in the 350-450 nm region which somewhat resembles the absorption of the crystalline rubrene film .

4.2.3. STEADY-STATE PHOTOLUMINESCENCE OF AMORPHOUS AND CRYSTALLINE RUBRENE UNDER PRESSURE

The steady-state photoluminescence (PL) spectrum represents the relaxed state of the excited singlet exciton (S_1). This state is produced on the fs timescale. As singlet fission in rubrene is reported to occur on ps timescale 19, the steady-state photoluminescence (PL) spectrum is a better measure for the energetic starting point of singlet fission than the absorption spectrum. The steady-state photoluminescence (PL) of amorphous and crystalline rubrene films at ambient pressure and their evolution under pressure are shown in Figure 4.3. The 0-0 and 0-1 transitions are clearly visible in the spectra of amorphous rubrene (Figure 4.3a), while the low-energy 0-1 transition is significantly suppressed in crystalline rubrene, which can be seen as a result of a H-type aggregation. As demonstrated by Spano et al. [156], the ratio between the transition strength of 0-0 and 0-1 transitions in PL of organic semiconductors provides useful information about the delocalization of singlet excitons. The higher ratio in the crystalline rubrene indicates a more delocalized singlet exciton that results from a higher level of π-stacking of the chromophores. The steady-state PL spectra of amorphous and crystalline rubrene are fit with two or three Voigt profiles to retrieve the transition strength of relevant vibronic transitions. Under pressure, the ratio of transition strength (R) between 0-0 and 0-1 transitions increases for both amorphous and crystalline rubrene (see Figure 4.8 for details). A higher R in amorphous rubrene, a weakly J-aggregate, suggests that a higher spatial coherence of the singlet exciton is facilitated by a higher level of intermolecular coupling, while a more localized exciton in crystalline rubrene, a H-aggregate, is indicated by a higher R [155]. We note that for Franck-Condon progressions, the width of

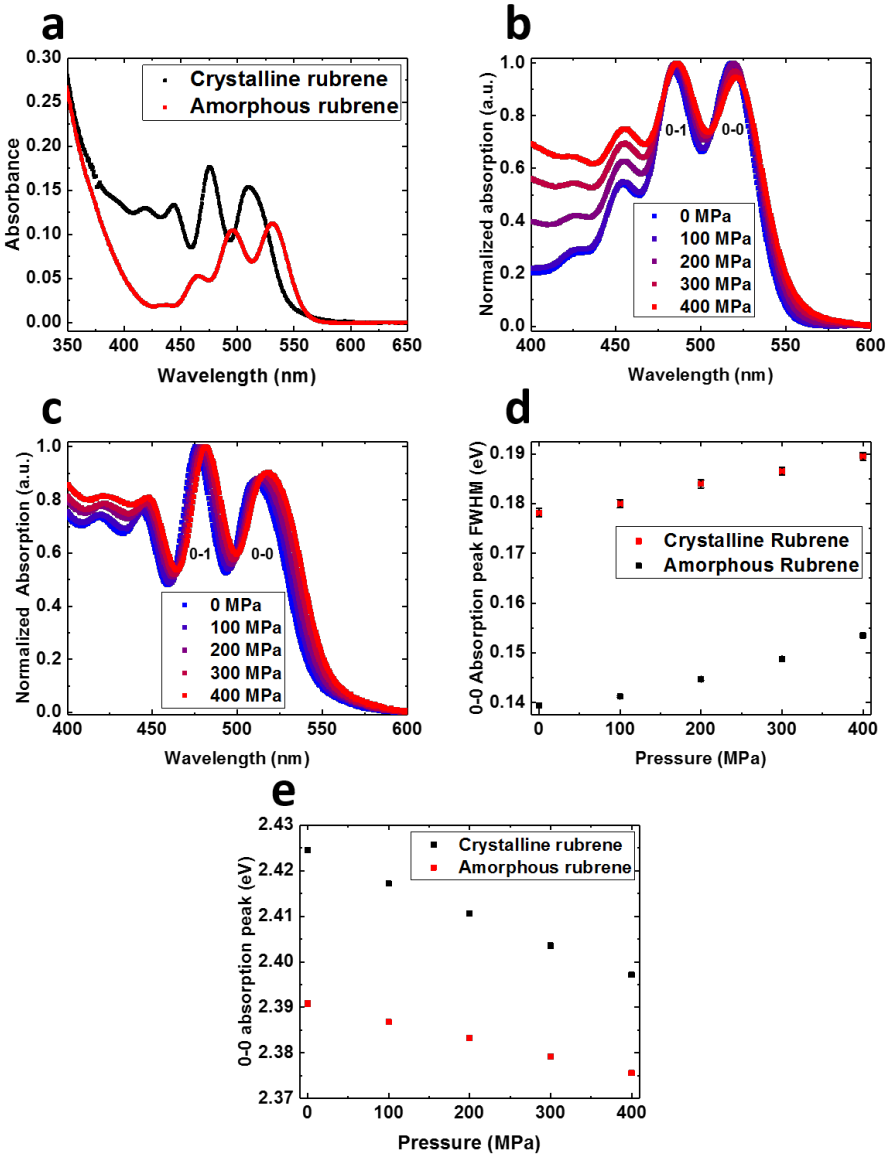

Figure 4.2: (a) Steady-state absorption spectra of amorphous and crystalline rubrene at ambient pressure; (b) Steady-state absorption spectra of amorphous rubrene from 0 to 400 MPa; (c) Steady-state absorption spectra of crystalline rubrene from 0 to 400 MPa; (d) FWHM of 0-0 absorption peak of crystalline and amorphous rubrene from 0 MPa to 400 MPa; (e) the shift of 0-0 peak position as function of applied pressure.

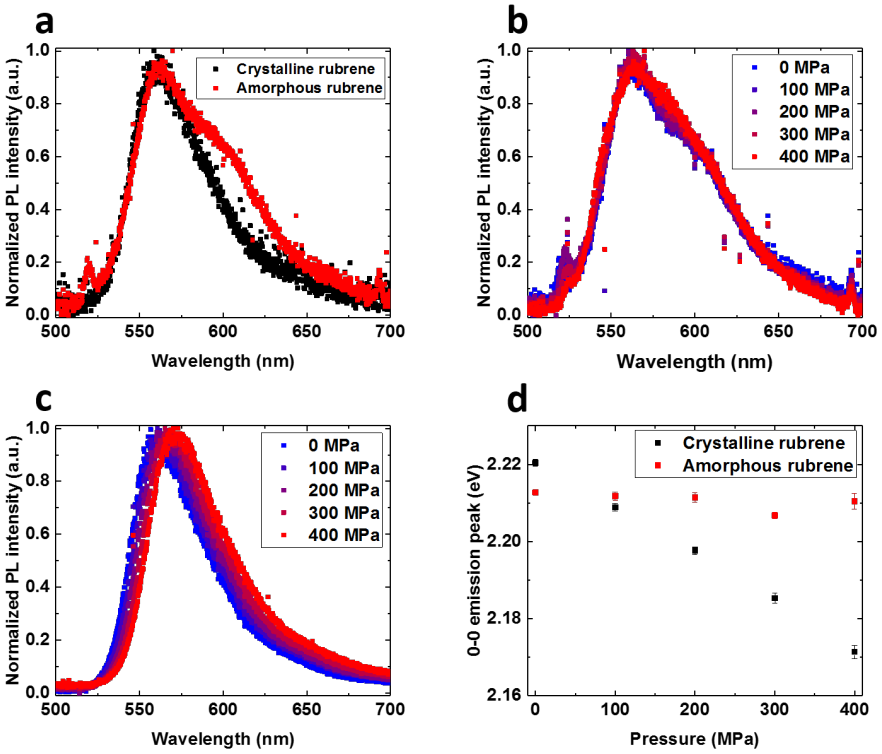

Figure 4.3: (a) Steady-state PL spectra of amorphous and crystalline rubrene at ambient pressure; (b) Steady-state PL spectra of amorphous rubrene from 0 to 400 MPa; (c) Steady-state PL spectra of crystalline rubrene from 0 to 400 MPa; (d) the shift of 0-0 emission peak position as function of applied pressure.

the vibronic peaks should be equal, while our fitting of the vibronic peaks shows different peak widths. The 0-0 emission peak of crystalline rubrene is moderately more blue (by 8 meV) compared to that of amorphous rubrene, which is consistent with the absorption spectra. Under increasing pressure up to 400 MPa, the 0-0 emission peak of dilute rubrene solution (see Figure 4.9 for details) red-shifts by 30 meV. The 0-0 emission peak amorphous rubrene barely shifts (Figure 4.3b and 4.3d), which could be attributed to the opposing contribution of an increasing polarization effect and a more H-type aggregation between chromophores, while a 50 meV red-shift is observed for crystalline rubrene (Figure 4.3c and 4.3d), indicating that the polarization effect dominates the spectral shifts while the molecular packing maintains which overall leads to a significant reduction in S_1 energy.

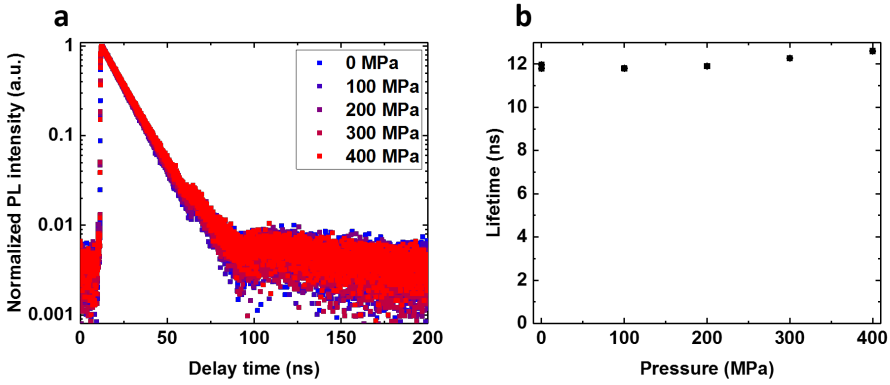

Figure 4.4: (a) PL spectra and (b) PL lifetime of dilute rubrene solution in chloroform from 0 MPa to 400 MPa

4.2.4. SINGLET FISSION DYNAMICS OF AMORPHOUS RUBRENE UNDER PRESSURE

As the wavefunction of triplet excitons are relatively localized to a single molecule [157], the energy of the first excited triplet exciton (T_1) will hardly be influenced by intermolecular electronic coupling. Thus, a higher energy barrier for singlet fission is expected for crystalline rubrene under pressure, as a result from the reduced S_1 energy. To probe the exciton dynamics in amorphous rubrene under pressure, we perform PL lifetime measurements using time-correlated single photon counting (TCSPC). The PL decay of dilute rubrene solution is mono-exponential and exhibits little change in lifetime under pressure (Figure 4.4).

Figure 4.5a shows the PL decay curves of amorphous rubrene under pressure. The PL decay in amorphous rubrene is significantly faster compared to the dilute solution due to the occurrence of intermolecular interactions, e.g. singlet fission. The decay shows no significant changes until 300 MPa. From 350 to 400 MPa, a faster decay of PL is observed. As singlet fission is a process that competes directly with fluorescence, a faster PL decay can indicate faster singlet fission. For a more quantitative analysis of the exciton dynamics, the PL decay curves are fitted with a set of coupled differential equations based on the following subsequent reactions (Equation 4.1) [158]: (see Section 4.4.2 for details):

$$S_1 + S_0 \underset{k_2}{\overset{k_{-2}}{\longleftrightarrow}} (TT)_i \underset{k_1}{\overset{k_{-1}}{\longleftrightarrow}} T_1 + T_1 \tag{4.1}$$

Where (TT) is the intermediate triplet pair state; k_{-2} is the transition rate from S_1 to (TT); k_2 is the transition rate from (TT) to S_1; k_{-1} is the transition rate from (TT) to T_1; k_1 is the transition rate from T_1 to (TT). The fitted transition rates are plotted in Figure 4.5b. While k_2, k_{-1} and k_1 show little change with increasing pressure up to 400 MPa, k_{-2} shows a two-fold increase from 300 MPa to 400 MPa, suggesting a more efficient transition from S_1 to (TT) under high pressure. It is worth noting that all emission is assumed to come from the S_1 in this model, while a recent report shows that (TT) states could also

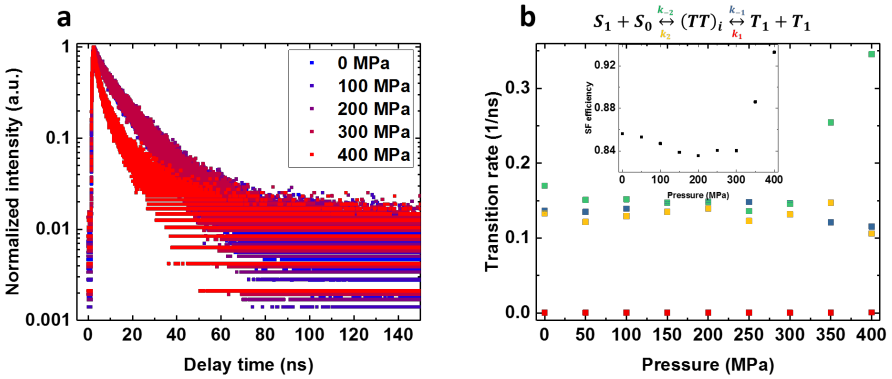

Figure 4.5: ((a) PL decay curves of amorphous rubrene from 0 to 400 MPa; (b) Fitted transition rates between relevant excited states from 0 to 400 MPa, colors of transition rates in reaction equation correspond to the data points in the plot, inset shows the calculated singlet fission efficiency as a function of pressure.

be emissive in polyacene derivatives [159, 160]. Also, the generation rate of S_1 is not included in the model, which may lead to an additional uncertainty in the values of fitted rates. With the fitted rates, the population of the different states can be derived from the kinetic model assuming equilibrium between the different states and steady-state conditions (see Section 4.4.2 for details).

The efficiency of singlet fission is represented by the fraction of T_1 population among total population. We find that the singlet fission efficiency increases from 84.0 % to 93.3 % when the pressure is increased from 300 MPa to 400 MPa (inset of Figure 4.5b), indicating that an increase of the electronic coupling between the chromophores is beneficial for singlet fission in amorphous rubrene. We note that the assumptions (equilibrium populations, no S_1 generation) are not entirely satisfied in the experiment, and hence the kinetic modelling allows only for an estimate of the relative efficiency changes. We also note that the term singlet fission efficiency is used ambiguously in the literature, in some instances it only refers to the efficiency of (TT) formation from S_1, while here we consider the full $S_1 \rightarrow 2T_1$ efficiency.

4.2.5. SINGLET FISSION DYNAMICS OF CRYSTALLINE RUBRENE UNDER PRESSURE

PL decay curves of crystalline rubrene under pressure are also measured via TCSPC (Figure 4.6). The prompt fluorescence decays significantly faster compared to amorphous rubrene, suggesting that singlet fission process proceeds more efficiently in crystalline rubrene, while the delayed fluorescence appears to have a slower decay.

The changes of prompt fluorescence in decay curves for crystalline rubrene under pressure is minimal, presumably due to the time-resolution of our instrument (0.5 ns).

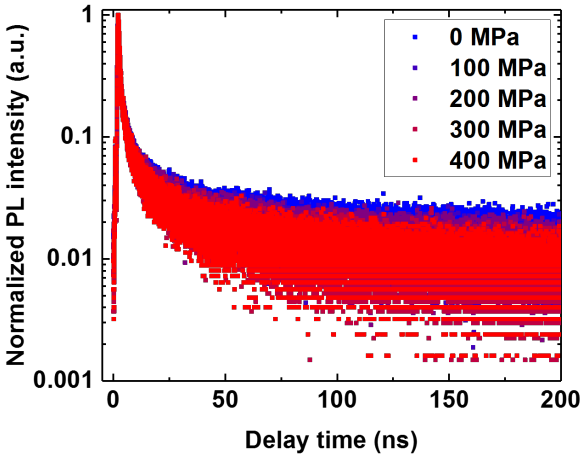

Figure 4.6: PL decay curves of crystalline rubrene from 0 MPa to 400 MPa.

Transient absorption spectroscopy (TA) is thus exploited to resolve the exciton dynamics under pressure with picosecond time resolution. TA spectra could not be measured on amorphous rubrene films due to rapid photo-degradation of the samples. Figure 4.7a and 4.7b show the TA spectra of crystalline rubrene from 500 nm to 700 nm at various delay times at ambient pressure and 400 MPa, respectively (see Figure 4.10 for spectra at other pressures). Following Miyata et al. [145], we assign the sharp photo-induced absorption (PIA) feature at 525 nm to the transition of the (TT) state to a higher lying triplet pair state, and the broad PIA feature centered around 580 nm to the transition of S1 state to a higher lying singlet state. A red-shift of the PIA features for both $(TT)_1 \rightarrow (TT)_n$ and $S_1 \rightarrow S_n$ is observed for the high-pressure spectra, consistent with increasing intermolecular coupling under pressure, for both the singlet and (TT) manifolds. The dynamics of S_1 and (TT) states under pressure are plotted in Figure 4.7c and 4.7d. We find that the decay of S_1 states and generation of (TT) states are independent of applied pressure, while the decay of (TT) is notably slower with increasing pressure, indicating a slower generation of uncorrelated triplets from the triplet pair state. As shown above from steady-state PL measurements, S_1 is stabilized by around 50 meV under pressure. The (TT) state shares a similar spin and spatial nature with S_1 [161], and should hence be similarly stabilized. The red shift of the PIA feature in the TA spectrum is also consistent with that assignment. The more localized T_1 states should be relatively unaffected by intermolecular coupling under pressure. Therefore, the stabilization of triplet pairs leads to to an increased energy barrier between (TT) and $2T_1$ and therefore a slower transition from (TT) to $2T_1$. Another factor that can influence the separation of triplet pairs is the degree of localization of singlet excitons. Previous studies [162, 163] have suggested that a delocalized singlet exciton is beneficial for the separation of triplet pairs. As is shown above, a more localized singlet excition in crystalline rubrene is indicated by a higher 0-0/0-1 transition strength ratio under pressure. As a result, the higher localization of

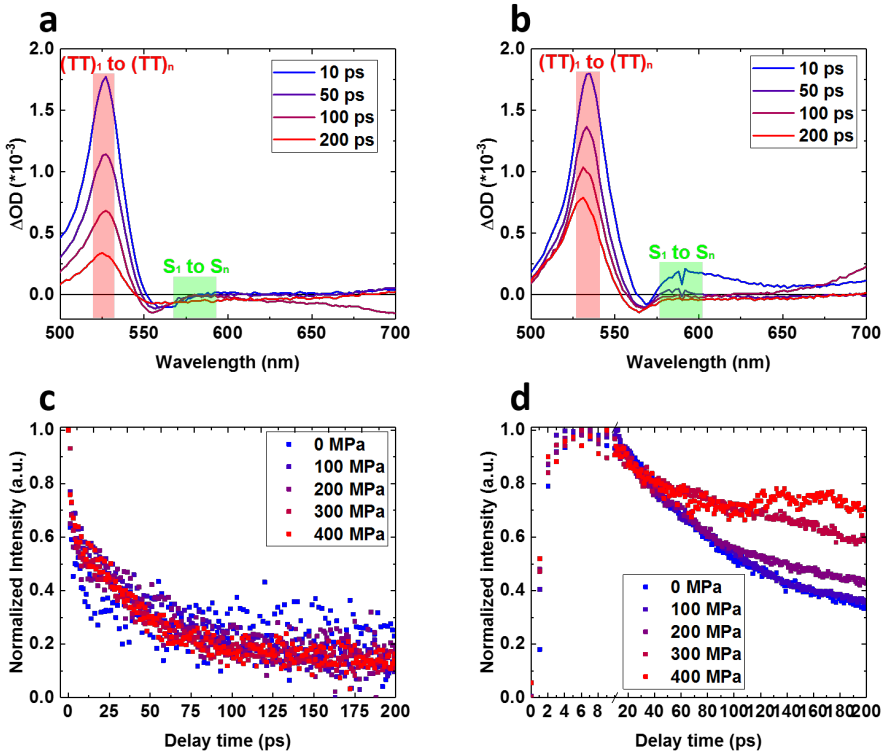

Figure 4.7: (a) TA spectra of crystalline rubrene at various delay times at ambient pressure; (b) TA spectra of crystalline rubrene at various delay times at 400 MPa; (c) Singlet exciton dynamics from 0 to 400 MPa; (d) Triplet pair dynamics from 0 to 400 MPa.

singlet excitons may additionally contribute to the longer lifetime of the triplet pairs in crystalline rubrene.

4.3. CONCLUSIONS

In conclusion, we find that by applying a moderate external stress, dynamics of singlet fission can be tuned effectively. Increasing electronic coupling between chromophores plays different roles for singlet fission in material systems with different morphologies, namely amorphous and crystalline rubrene. For amorphous rubrene, the efficiency of singlet fission shows a significant increase from 300 MPa onwards, which is facilitated by an increased transition rate from the first excited singlet state (S_1) to the intermediate triplet pair (TT). For crystalline rubrene we observe no change in the efficiency of (TT) formation, indicating that the electronic coupling does not limit the singlet fission rate. On the contrary, we observe a slower dissociation of the triplet pair as revealed by transient absorption measurements under pressure, as a result of a 50 meV decrease in

S_1 energy. Our results show that increasing electronic coupling can play different roles in material systems with different morphologies and that both the relative energy levels of relevant excited states and the intermolecular coupling need to be considered for designing highly efficient singlet fission materials.

4.4. SUPPLEMENTARY INFORMATION

4.4.1. EXPERIMENTAL METHODS

Sample preparation: Rubrene (sublimed grade, 99.99 % purity) was purchased from Sigma Aldrich and used as received. Fused silica glass substrates were sonicated with Alconox detergent, deionized water, acetone, and isopropanol sequentially for 10 min and treated with oxygen plasma at 100 W for 15 min. Amorphous rubrene thin films were prepared via thermal evaporation (Angstrom Engineering) under a vacuum of 1.5×10^{-7} Torr at a deposition rate of 0.5 Å/s. To obtain crystalline rubrene thin films, 20 nm-thick amorphous films were first deposited at the same rate as for the amorphous films. The thin amorphous films were annealed at 170 °C for 180 s in a nitrogen atmosphere. A mild opacity in the rubrene films was visible after annealing. Another 80 nm-thick rubrene was then deposited on top of the annealed films to yield a 100 nm-thick crystalline film. All rubrene films are kept in nitrogen atmosphere before optical measurements.

Pressure generation and measurements: Hydrostatic pressure was generated through a pressurizing liquid Fluorinert FC-72 (3M) inside a high-pressure cell (ISS Inc.) using a manual pump. before using the liquid, degassing procedure was performed at liquid nitrogen temperature to remove the oxygen dissolved in the pressure liquid. The pressure was applied from ambient pressure to 400 MPa in steps of 100 MPa. In order to stabilize the applied pressure and allow the material to equilibrate, a 5-7 min waiting time is taken between measurements at two adjacent pressure points. A 20 MPa error is estimated for the pressure reading based on measurement to measurement variability.

UV/Vis absorption: Absorbance spectra of rubrene thin films were measured with a LAMBDA 750 UV/Vis/NIR Spectrophotometer (Perkin Elmer) from 350 nm to 700 nm in steps of 0.5 nm. A correction of the absorption spectra was done for all the spectra obtained above 300 MPa by subtracting the background signal from scattering in the liquid. The background was obtained from a fit in the region of 660 nm to 700 nm where rubrene does not absorb, and is typically lower than 10 %.

Steady-state photoluminescence: Steady-state photoluminescence (PL) was measured with a home-built setup equipped with a 405 nm continuous-wave laser as source of excitation (S1FC405, Thorlabs) at a power output of 2 mW. The PL of the samples was coupled into a fiber connected to an OceanOptics USB4000 spectrometer, set to an integration time of 1000 ms for each measurement. The PL spectra were fitted with two or three Voigt profiles.

Time-correlated single-photon counting: Time-correlated single-photon counting

(TCSPC) measurements were performed with a home-built setup equipped with PicoQuant PDL 828 "Sepia II" and a PicoQuant HydraHarp 400 multichannel picosecond event timer and TCSPC module. A 485 nm pulsed laser (PicoQuant LDH-D-C-485) with a repetition rate of 5 MHz was used as source of excitation and a single-photon avalanche diode (SPAD) detector (Micro Photon Devices, MPD-5CTD) was used for the detection of photoemission. The TCSPC data was integrated over 600 seconds per measurement.

Transient absorption: Transient absorption measurements were performed with a home-built setup equipped with a Ti:Sapphire laser (Coherent, 800 nm, 1 kHz, 35 fs, 6.35 W). The 800 nm fundamental laser was split into two parts to generate the pump (400 nm) using a Barium borate (BBO) crystal and the broadband probe using a sapphire plate. The time delay between the pump and the probe is controlled via a mechanical delay stage. TA spectra at each pressure is taken in steps of 1 ps. An averaging of 5000 spectra was done at each delay time to yield a higher signal to noise ratio.

4.4.2. ANALYSIS OF TSCPC DATA OF AMORPHOUS RUBRENE

To quantitatively model the TCSPC data of amorphous rubrene under pressure, we use the reaction equation from Figure 4.5b, from which we obtain following set of coupled differential equations:

$$\frac{dN_s}{dt} = -(k_S + k_{-2})N_S + k_2 N_{(TT)} \tag{4.2}$$

$$\frac{dN_{(TT)}}{dt} = -(k_2 + k_{-1})N_{(TT)} + k_{-2}N_S + k_1 N_T^2 \tag{4.3}$$

$$\frac{dN_T}{dt} = -(k_T + k_1)N_T + k_{-1}\sqrt{N_{(TT)}} \tag{4.4}$$

Where N_S, $N_{(TT)}$ and N_T are the population of the first excited singlet state (S_1), the intermediate triplet pair state ((TT)) and the first excited triplet state (T_1), respectively; k_{-2} is the transition rate from S_1 to (TT); k_2 is the transition rate from (TT) to S_1; k_{-1} is the transition rate from (TT) to T_1; k_1 is the transition rate from T_1 to (TT)). k_S and k_T are the intrinsic decay rates of S_1 and T_1; The above-mentioned transition rates can then be extracted from the fitting. Using the fitted rates, we perform kinetic modeling using the following equilibrium equations:

$$-k_{-1}N_S + k_1 N_{(TT)} = 0 \tag{4.5}$$

$$k_{-2}N_{TT} + k_2 {N_T}^2 = 0 \tag{4.6}$$

$$k_{-1}N_S - k_1 N_{(TT)} + k_2 {N_T}^2 - k_{-2}N_{TT} = 0 \tag{4.7}$$

$$N_S + N_{(TT)} + 2N_T = 1 \tag{4.8}$$

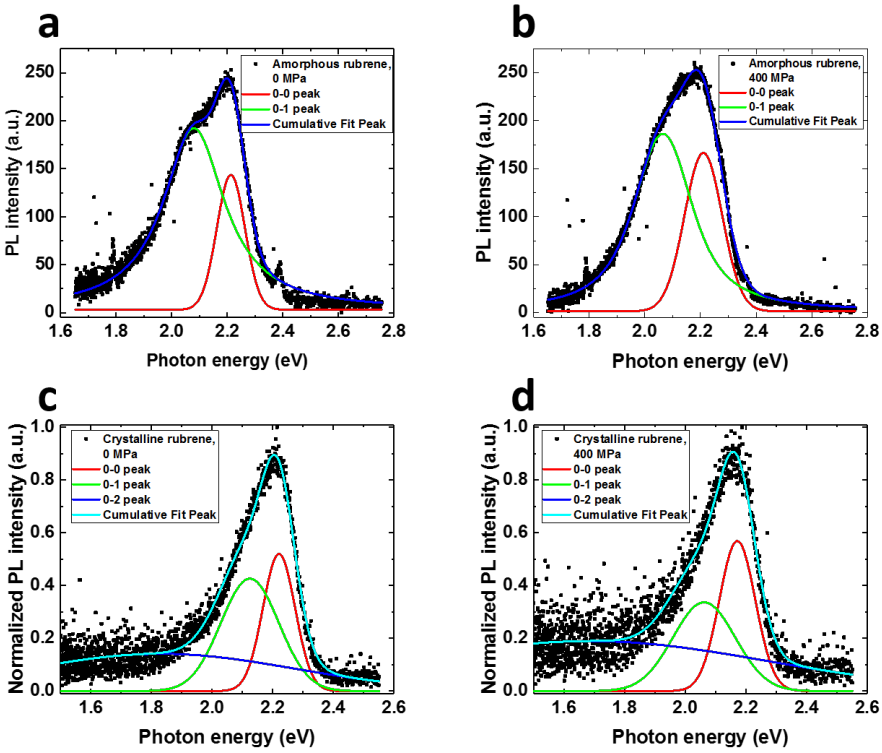

Figure 4.8: PL spectra of crystalline and amorphous rubrene with fitting at 0 MPa and 400 MPa: (a) amorphous, 0 MPa; (b) amorphous, 400 MPa; (c) crystalline, 0 MPa; (d) crystalline, 400 MPa.

The efficiency can then be calculated by taking the fraction of triplet population among the total population of all excited states.

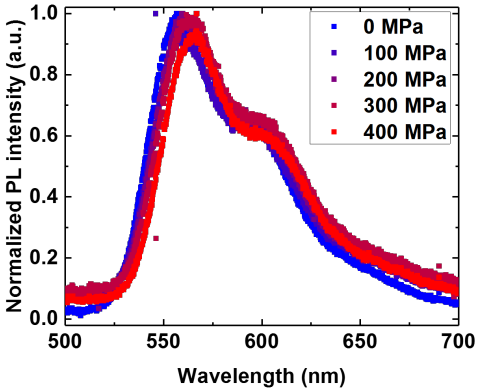

Figure 4.9: PL spectra of dilute rubrene solution in chloroform from 0 MPa to 400 MPa.

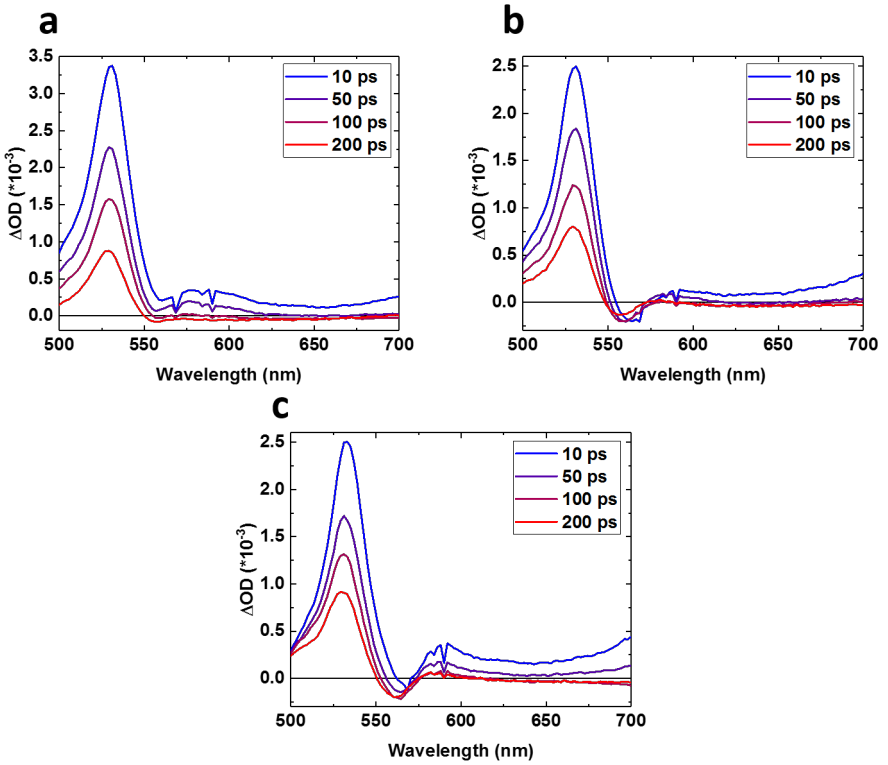

Figure 4.10: TA spectra of crystalline rubrene at various delay times at (a) 100 MPa, (b) 200 MPa and (c) 300 MPa.

5

PHOTON UPCONVERSION IN AN IONIC LIQUID: A PRESSURE STUDY

Photon upconversion presents a way to circumvent the Shockley-Queisser limit for solar cells by allowing sub-bandgap photons to be used for power generation. An ionic liquid capable of photon upconversion by triplet-triplet annihilation was characterized using spectroscopy, magnetic fields and hydrostatic pressure. The system was found to be more strongly electronically coupled under pressure, reflecting decreased intermolecular distances. The response of the upconversion to a magnetic field was surprisingly solid-like. The threshold intensity of upconversion was determined as 18.0 mW/cm^2. Since efforts to determine the dependence of the threshold intensity on pressure were inconclusive, suggestions are given for further research.

Work in this chapter is a combined effort with Arnoud Jongelling. Upconverting ionic liquid is kindly provided by Shota Hisamitsu and Dr. Nobuhiro Yanai from Kyushu University.

5.1. INTRODUCTION

Photon upconversion is the process that converts low-energy photons into higher-energy photons. Great research attention has been attracted to photon upconversion due to its wide range of potential applications in solar cells [44, 164], light-emitting diodes [45] and biomedical therapy [43]. For solar cells, the upconverted light can be utilized to reduce the spectrum losses due to photons with energy lower than the absorber's bandgap. Up to today most upconversion systems are solution based [46]. A solid-state upconversion system that can convert infrared photons to visible photons has recently been developed by researchers from MIT [48], while an intermediate band solar cell with enhanced sub-bandgap has also been demonstrated by researchers from Princeton University using photon upconversion [165], showing the potential of photon upconversion for photovoltaics.

Both inorganic materials and organic molecules can be used for photon upconversion. For inorganic materials, especially lanthanide-containing nanoparticles, the major limitation is the low quantum efficiency of the upconversion process (usually lower than 1 %). Photon upconversion in organic molecules typically shows higher efficiency, and is based on a different process, named triplet-triplet annihilation (TTA) (Figure 5.1). The process of upconversion by TTA begins with the absorption of photons by a sensitizer, initially exciting it to a singlet excited state. The sensitizer usually contains one or more heavy elements such as Platinum, Palladium and Iridium that induce strong spin-orbit coupling, which allows rapid intersystem crossing from the singlet state to the triplet state. Thus, through intersystem crossing, the sensitizer produces triplet excitons from the photoexcitation.

These triplets are then transferred to an emitter, often polyacene derivatives. Exchange of triplet excitons happens through the Dexter energy transfer mechanism, which involves the simultaneous transfer of the electron and hole from one chromophore to another. The process is dependent on wavefunction overlap between molecules and thus the transfer rate decreases exponentially with distance. As radiative decay from the triplet state is spin-forbidden and there is no strong spin-orbit coupling in the emitter, triplet excitons cannot easily decay to the ground state. Through Dexter transfer of triplets between emitters, and molecular diffusion of emitters if the system is in solution, two triplet excitons can collide. The emitter molecule is selected so that the energy of the first triplet state is approximately half that of the first singlet excited state. The electrons in two triplet excitons can rearrange to one singlet exciton and one singlet ground state while conserving total spin angular momentum, so the combination is spin-allowed as well as energetically favorable. The rearrangement proceeds through an intermediate triplet pair ((TT)). With the radiative decay of the resultant singlet exciton, emitting a higher-energy photon, the triplet-triplet annihilation is complete and photon upconversion is achieved (Figure 5.1).

The process of upconversion by TTA is characterized by two regimes [167]. At low light intensities and thus low triplet concentrations, the probability that two triplets will

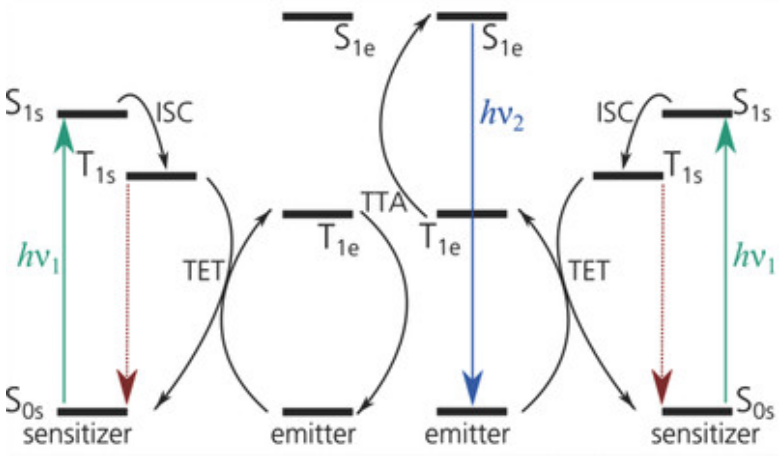

Figure 5.1: Graphical illustration of TTA-based photon upconversion process. Image adapted from [166].

annihilate is a quadratic function of the triplet concentration, as the probability that a given triplet will collide with another before decaying increases linearly with triplet concentration, and two particles are involved in the collision. At higher intensities, the time before colliding with another triplet is significantly shorter than the triplet lifetime and the probability that a given triplet is upconverted no longer depends on the concentration. The rate law becomes first-order in this case, a linear function of the triplet concentration. Any loss mechanisms that affect either the triplet or the multiexciton can decrease the triplet lifetime or quantum efficiency, but only alter the overall quadratic and linear behavior if the loss mechanisms are concentration dependent. While the transition between these two regimes is not sharp but rather continuous, a value known as the threshold intensity can be found by extrapolating the quadratic and linear regimes and finding the intersection point. The more desirable regime for the operation of a TTA upconversion system is the high-intensity regime since the system is at its peak quantum efficiency then. Therefore, a low threshold intensity would be greatly beneficial for the realistic operation of a TTA upconversion system, e.g. at solar intensity.

The TTA-based photon upconversion can reach a maximum theoretical quantum efficiency of 50 %. Although molecular systems in solution have shown high quantum efficiency [46], the quantum efficiency of solid-state TTA upconversion systems is significantly lower than the solution systems, largely due to the reabsorption of the upconverted light. The low efficiency of solid-state TTA upconversion systems strongly hinders application in solid-state devices like solar cells and LEDs. Liquid systems are also technologically difficult to implement on large-area. Therefore, a solid-state or solid-state-like materials system with high upconversion efficiency is highly desirable.

Hisamitsu et al. [168] reported the synthesis of a TTA upconversion system based on an ionic liquid, with platinum octaethylporphyrin (PtOEP) as the sensitizer and diphenylanthracene (DPA) as the emitter in 2015 (Figure 5.2). Because the DPA chromophore is

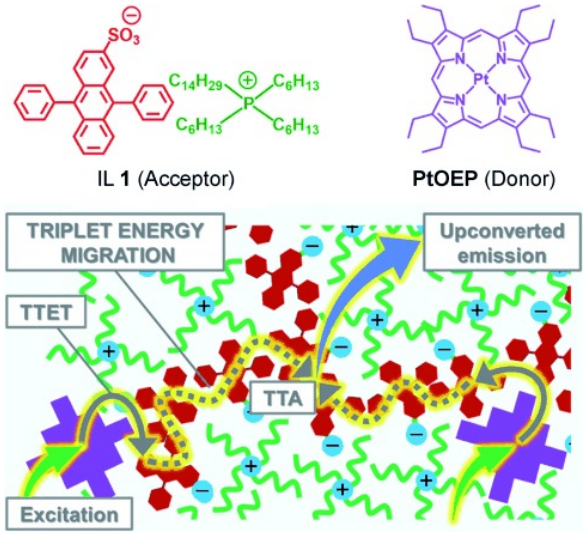

Figure 5.2: Emitter and Sensitizer present in the ionic liquid and schematic illustration of TTA upconversion in ionic liquid. Image adapted from [168].

covalently bound to the negatively charged sulfonate group, it has a strong energetic incentive to remain dispersed in the liquid. The counterion is a tetraalkylphosphonium structure whose tails act to keep the system liquid at room temperature. This approach circumvents problems with solubility limits of the emitter, which is usually a significant limiting factor. While not strictly a solid, the ionic liquid is highly viscous (2760 Pa s) and might be considered pseudo-solid state and a realistic form factor for a practical upconversion system. Considering the high viscosity and consequently slow molecular diffusion, Dexter-type energy transfer is the dominant mechanism in triplet diffusion, as was demonstrated by operating the system in frozen form. The threshold intensity was remarkably low at 3.0 mW/cm^2. The low value might be a result of the formation of a bi-continuous structure in the liquid, with the alkyl tails of the cations and the DPA chromophores of the anions forming interlocking, contiguous structures. This densely packed arrangement of emitters would allow for easy transfer of triplets between adjacent molecules, while the continuous structure ensures that all triplets can reach one another. The driving force for the assembly of this structure would be the difference in cohesive energy between the aromatic DPA and aliphatic alkyl chains, as well as the electrostatic attraction of the ions.

Despite the desirable properties demonstrated, the understanding of basics for TTA upconversion in the ionic liquid is still lacking, especially how the microstructure of the ionic liquid influences the energetics of the involved excited states, the rates of triplet transfer and the overall kinetics and efficiency.

To investigate the influence of intermolecular distances on processes such as triplet energy transfer from the sensitizer to the emitter and between emitters, one possible way

is to alter the chemical structure of the system under study [139]. While effective, this approach requires the time-consuming synthesis and characterization of an entirely new compound, which might have very different energetics and entropy in the system.

In this chapter, we use hydrostatic pressure up to 400 MPa as a clean tool to change the intermolecular interactions of the TTA upconversion ionic liquid mentioned above. We measure the steady-state absorption and upcoversion photoluminescence as a function of pressure. Of particular interest is the pressure dependence of the threshold intensity, which we also measure. We also study the effect of an external magnetic field on the upconversion process as a further characterization for the molecular ordering in the ionic liquid system.

5.2. RESULTS AND DISCUSSIONS

5.2.1. UV-VIS ABSORPTION OF UPCONVERSION IONIC LIQUID UNDER PRERSSURE

The absorption spectra for the ionic liquid both with (Figure 5.3a) and without PtOEP sensitizer (Figure 5.3b) under pressure up to 400 MPa are shown in Figure 5.3. The vibronic absorption peaks of DPA [169] are clearly visible between 300 and 450 nm. The different peaks in this structure represent the molecule being excited to the same electronic state (the first singlet excited state), but in different states of molecular vibration. The spectra are also in good agreement with the original work [168]. At increased pressure, a small but significant redshift is observed in the absorption spectra. The peak between 200 and 300 nm represents a transition to a higher electronic excited state. The much lower height of this peak in the pure ionic liquid at 0 MPa is considered an artifact of measuring such high absorbance values as the detector is operating with very few photons then. The difference in peak heights between the two samples is due to variation in sample thickness, which could only be controlled qualitatively due to the high viscosity of the ionic liquid. At 350 and 400 MPa the absorption appears to increase at all wavelengths; the apparent increase is due to scattering caused by the partial solidification of the hydraulic fluid, nucleating the formation of a sol at these pressures. The scattering from the pressure liquid is deemed a minor, spectrally broad effect that does not invalidate the acquired spectra. Spectra taken on the down stroke (Figure 5.4) confirmed that there is no significant hysteresis with respect to pressure and there was no significant degradation of the samples during measurement.

The main absorption peak of PtOEP around 530 nm [170] was detected in the sample in which it was present, but was only resolved in samples much thicker (around 1 mm) than the ones used for the pressure measurements owing to the low PtOEP concentration in the ionic liquid (Figure 5.5). The presence or absence of PtOEP absorption was the only difference between the two samples; the absorption peaks of the DPA chromophore were unaffected. In these thicker samples, the absorption of the DPA chromophore was so high that no appreciable amount of radiation shorter than 450 nm could reach the detector and a plateau appeared at those wavelengths. Even the valley around 300 nm was not detected. The different appearance of the plateaus in Figure 5.5 is due to variance

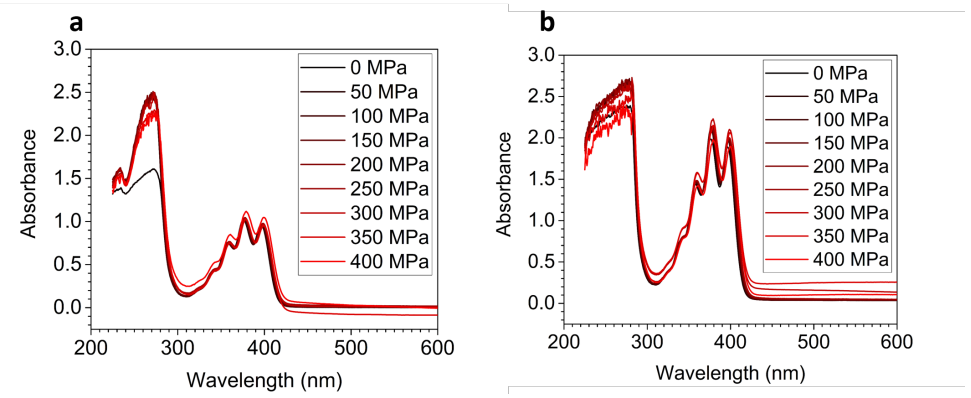

Figure 5.3: The absorption spectra for the ionic liquid (a) with and (b) without PtOEP sensitizer under pressure up to 400 MPa.

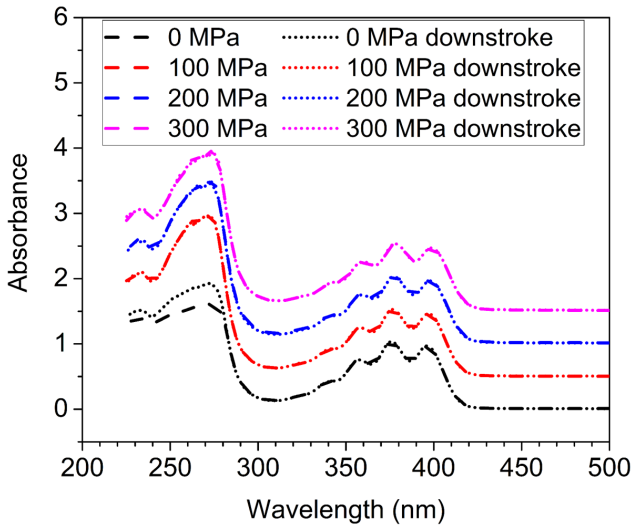

Figure 5.4: The absorption spectra for the ionic liquid without PtOEP sensitizer in the pressure up- and downstroke. The spectra are offset for clarity.

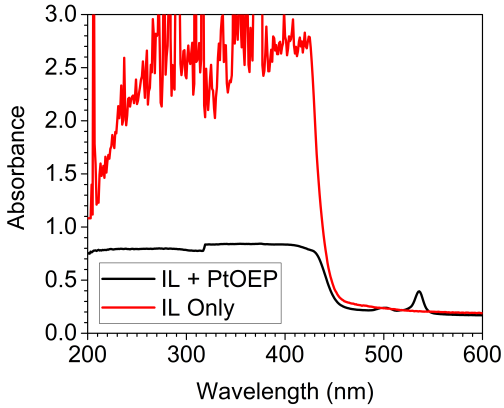

Figure 5.5: The absorption spectra for the ionic liquid without PtOEP sensitizer in the pressure up- and downstroke. The spectra are offset for clarity.

in sample geometry; the thicker samples were prepared without sandwiching and the ionic liquid formed droplets over time. The pure ionic liquid sample blocked the beam entirely while the sample with PtOEP obstructed only a part of the beam area, so that the measured absorbance values were lower and enough photons reached the detector to not appear as a noisy signal.

By modeling each spectrum as a system of Gaussian peaks, the effects of pressure can be quantified. The shoulder visible around 375 nm was consistently fitted as a peak and is known to correspond to a real vibronic transition [171], hence the decision to use a five-peak system. The shifts of the vibronic peaks under pressure are shown in Figure 5.6. The central energy of each peak slightly but consistently decreases with pressure, with a slope that is similar for each peak. Generally, the slope is around -70 μeV/MPa. The lack of abrupt changes or other features in the relationship between energy and pressure is an indication that no dramatic structural changes are caused by the high pressure and the intermolecular distances are being varied smoothly as intended. Crucially, the redshift is an indication that the strength of electronic coupling between the molecules is increased under pressure. In the liquid state or in a solvent, peaks from electronic transitions are typically redshifted compared to the vapor phase since excited states are electric dipoles and a polarizable medium acts to stabilize that dipole [19]. In this case, the smaller intermolecular distances at high pressure act to increase the stabilizing effect of the polarizability of the surrounding medium. The observed redshift is consistent with the observation in the original work that the absorption of the neat ionic liquid is redshifted compared to a solution of the ions in methanol, again indicating a stronger interaction of the chromophores. This observation was taken as indirect evidence of the bicontinuous structure of the liquid.

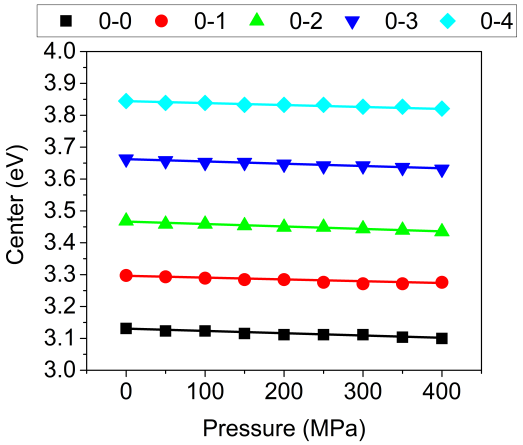

Figure 5.6: The shifts of vibronic peaks of DPA in the ionic liquid with PtOEP sensitizer.

5

5.2.2. STEADY-STATE PHOTOLUMINESCENCE OF UPCONVERSION IONIC LIQUID UNDER PRERSSURE

To confirm the capability of upconversion for the ionic liquid with PtOEP sensitizer under ambient conditions, we perform steady-state photoluminescence measurements using a continuous-wave solid-state laser at 532 nm as excitation source. Figure 5.7a shows a top-view image of the upconverted PL of the sample with sensitizer immersed in the pressure liquid Fluorinert FC-72. A cyan to white emission form the sample is observed while excited with a green laser, qualitatively showing that the system is capable of upconversion. The upconversion photoluminescence spectrum can be seen in Figure 5.7b and has a strong component with shorter wavelengths than the excitation laser at 532 nm. The spectral shape is in good agreement with the original work [168] In the ionic liquid without the PtOEP sensitizer, no detectable photoluminescence was observed while excited at the same wavelength, confirming that PtOEP sensitizer is required for initiating the upconversion process.

The spectra in Figure 5.7b are taken with a 500 nm shortpass and 550 nm longpass filter. As a result, no emission is detected between 500 and 550 nm. In samples that were exposed to air for several days, the color turned to magenta as an additional peak appeared in the spectrum around 650 nm, corresponding to the phosphorescence of PtOEP [172], and the intensity of upconversion photoluminescence decreased significantly. This is a strong indication of less efficient triplet transfer from the sensitizer to the emitter, which could be a result of the degradation of the emitter.

To confirm that the nature of the upconversion is indeed via triplet-triplet annihilation, the influence of an external magnetic field on the intensity of upconversion photoluminescence was measured. The results of this measurement are plotted in Figure 5.8. Around 3000 Gauss there is a disturbance that appears to have affected all subsequent measurements, including the reverse field scan. The discontinuity could be a result of

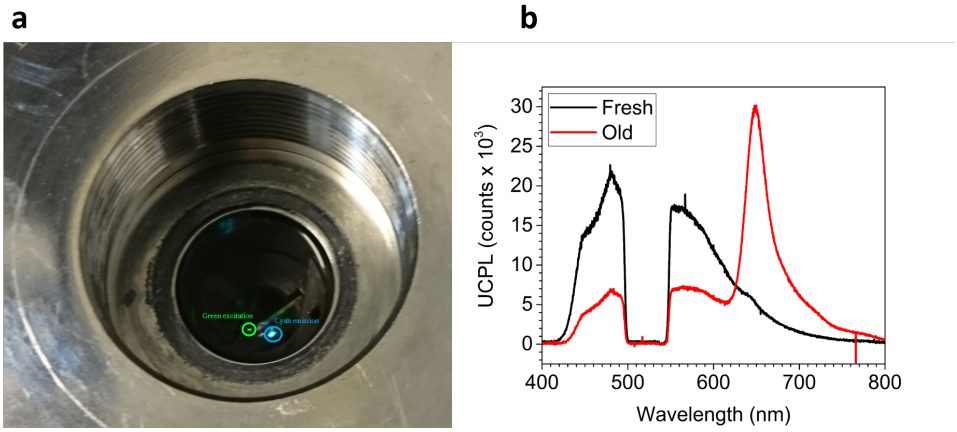

Figure 5.7: (a) The upconversion photoluminescence from a sample with PtOEP in the pressure cell and (b) PL spectra from a freshly prepared sample and a sample that was exposed to air for seven days.

mechanical movement of some optical components, e.g. lens, out of the alignment due to the strong magnetic field. Despite this, the measurements up to the disturbance appear to be valid and will be treated as such.

The overall shape of the curve up to the disturbance shows an initial slight increase in upconversion photoluminescence, followed by a sharper decrease and eventual saturation. This is consistent with triplet-triplet annihilation in crystalline solid films [173]. In such an ordered system, the multiexciton state can be interpreted in terms of wavefunction symmetry with respect to exchange of the two constituent triplets [174]. This separates the even states, which are overall singlets, quintets, and mixtures thereof, from odd states which are overall triplets. At zero field, three of the nine multiexciton states have singlet character and can participate in upconversion, while a magnetic field of intermediate strength mixes the singlet and quintet in such a manner that all six even states have singlet character. At high field strength, the singlet character is concentrated into two states so that the upconversion efficiency is reduced. The reduction at high field depends on the ratio of the dissociation rate and annihilation rate of the multiexciton, and is one third if annihilation is greatly favored.

Conversely, in solutions and glassy solids the molecules are oriented randomly and the exchange symmetry approach is no longer valid [173]. At zero field, all nine states have nonzero singlet character while at high field, the singlet character is again concentrated into two states. Thus solution systems show upconversion that decreases monotonically with an increase in magnetic field strength [175], where the maximum reduction is one ninth, again if annihilation is favored over dissociation. The initial increase seen in the ionic liquid indicates that while the system is a liquid, there is some preferred orientation to the DPA chromophores. Since this ordering is unlikely to be complete, the behavior probably lies between the two extremes of crystalline and disordered. Because

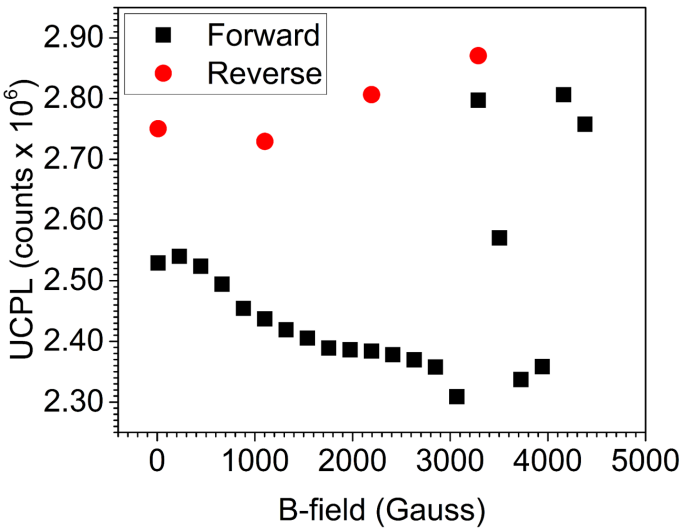

Figure 5.8: Intensity of upconverted PL as function of external magnetic field at ambient pressure.

the size of the initial increase depends not only on the degree of ordering but also the branching ratio between dissociation and annihilation, the degree of ordering cannot be determined exactly from this data.

The dependence of the upconversion photoluminescence on the excitation power density at different pressures is shown in Figure 5.9. The data above 200 MPa is not measured as the accurate PL intensity could not be determined due to the scattering of pressure liquid at higher pressure. The overall shape of the curves is as expected for a TTA upconversion system: quadratic at low intensity (appearing linear with slope two on a log-log plot), transitioning to linear at high intensity (linear with slope one). This shape is due to triplet-triplet annihilation being limited by triplet decay at low triplet densities and thus having bimolecular kinetics, but limited by formation of the singlet exciton from two bound triplets at high intensities and having unimolecular kinetics then.

The overall intensity of the curves appears to decrease with increasing pressure, but the curves taken on the down stroke have lower intensity still. The mismatch between up stroke and down stroke measurements at the same pressures indicates an irreversible degradation of the upconversion system, probably due to photobleaching of the sensitizer during the high-intensity measurements despite efforts to minimize the exposure times. Photo-oxidation could be an additional degradation channel as the pressure liquid tends to dissolve a significant amount of oxygen [176]. Figure 5.10a illustrates the process used to find the threshold intensities: the four lowest and the four highest intensity data points were used for fitting of linear functions (using the logarithms of both

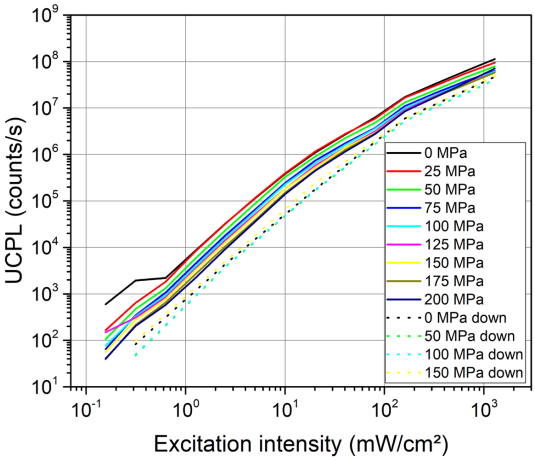

Figure 5.9: Intensity of upconverted PL versus excitation density, at different pressures.

coordinates) of slopes two and one, respectively. The threshold intensity was then given by the intersection of those functions. The threshold intensities at different pressures can be seen in Figure 5.10b. At ambient pressure, the threshold intensity is determined to be 18.0 mW/cm^2. This is in rough correspondence with the original work [168], where the value was determined as 3.0 mW/cm^2. The difference could be due to a number of reasons, such as the lower PL collection efficiency in the pressure cell, the triplet concentration being different at the same laser intensity due to a difference in sample thickness, or differences in the way the beam spot diameter was determined. Just as the total photoluminescence decreased constantly during data acquisition, the threshold intensity appears to have mostly increased, with the down stroke measurement at 0 MPa being a notable exception. The magnitude of the disagreement between the up and down strokes appears to follow no easily identifiable pattern.

As is shown in Figure 5.11, the measured UCPL intensity and threshold intensity roughly follow a negative correlation: points with lower UCPL intensity tend to have higher threshold intensity. The degradation during measurement makes it nontrivial to make reliable statements about the pressure-dependent behavior. Through the effects of the degradation, the two lowest-pressure data points of the downstroke measurements suggest a possible upward trend in the threshold intensity with pressure, contrarily to what was predicted. To determine the behavior of the threshold intensity under pressure more conclusively, a more refined version of the experiment is necessary. An increase in the threshold intensity at high pressure would imply that any decrease in threshold intensity due to longer triplet diffusion length is offset by another pressure dependent phenomenon. One possibility is that hydrostatic pressure changes the relative orientations of the molecules in such a way that triplet diffusion is impeded or triplet decay is facilitated. It is also possible that the molecules are forced into a more ordered configu-

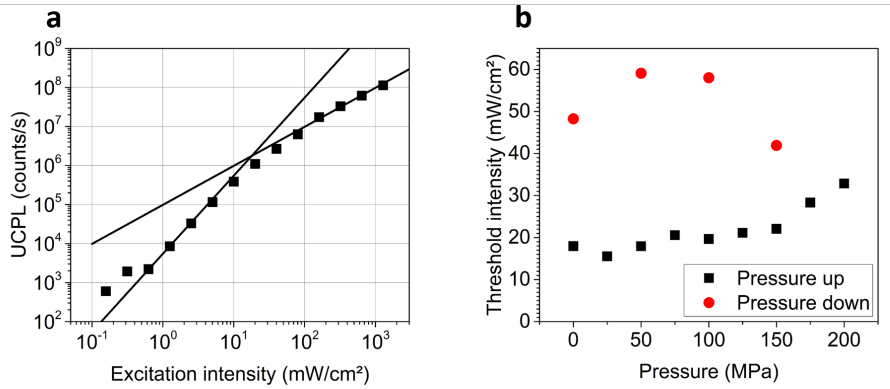

Figure 5.10: (a) Determination of threshold intensity and (b) Threshold intensity of the upconversion system as function of pressure.

ration, thus concentrating the singlet character into fewer states of the multiexciton and rendering annihilation to a singlet less likely. While no phase changes are thought to occur in the relevant pressure range, a continuous rearrangement is still a possibility, as happens in liquid water close to its freezing point. Furthermore, the two triplets resulting from such a dissociation could remain entangled as an overall triplet for some time and be unable to annihilate on subsequent collisions [177]. Thus, each triplet must travel further on average to find a suitable annihilation partner, leading to a higher threshold intensity.

Possibly the two lowest-pressure down stroke points are faulty; since the linear fit was done on the basis of two intensity measurements for the down stroke, a single measurement error could invalidate the value found for the threshold intensity. Furthermore these data points should be considered the least reliable of all as the sample was the most damaged for these measurements. Thus possibly the threshold intensity generally decreases with pressure. This would be more in line with expectations as the emitter molecules come into closer contact, as verified by the UV-vis spectroscopy, and Dexter transfer of triplet excitons between emitters is facilitated, thus increasing their diffusion length and requiring lower triplet concentration to reach the threshold.

5.3. CONCLUSIONS

To conclude, the ionic liquid upconversion system was found to be more strongly electronically coupled at high pressures, which is evident by the red-shifting of absorption spectra by around 70 μeV/MPa due to the higher polarizability of the molecules induced by the shorter intermolecular distances in the ionic liquid. The upconversion in the system was also found to have a solid-like response to a magnetic field, showing a slight increase in photoluminescence with magnetic field strength, followed by a stronger decrease and eventual saturation. This pattern implies high symmetry in the orientation

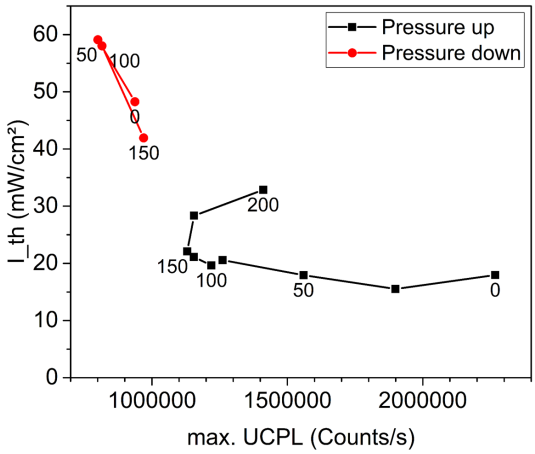

Figure 5.11: Relationship of calculated threshold intensity, UCPL at maximum excitation intensity (1288 mW/cm2) and pressure (inset labels).

of emitter molecules and thus a high degree of ordering in the structure of the material, despite it being able to flow as a viscous liquid.

At ambient pressure, the threshold intensity of upconversion, at which the dependence on incident light intensity transitions from quadratic to linear and the system reaches its peak quantum efficiency, was measured as 18.0 mW/cm^2. The measurements at increased pressure were largely rendered inconclusive due to degradation induced by photo-bleaching and photo-oxidation. An increase in the threshold intensity at high pressure could be ascribed to the structure of the material becoming more ordered, thus leading to unfavorable spin statistics that would increase the probability of two bound triplets dissociating. Conversely, a decrease in the threshold intensity could be due to more efficient triplet diffusion, so that triplets travel further before decaying and are more likely to collide.

Overall, the upconversion in the ionic liquid seems to be governed by its characteristics that are intermediate between solid and liquid state; the response to magnetic fields is solid-like but the system has superior quantum efficiency and threshold intensity to typical solid upconversion systems. More research is necessary to determine the solid or liquid character of the system at high pressure and its influence on the upconversion behavior.

5.4. FUTURE PERSPECTIVES

5.4.1. REFINEMENT OF INTENSITY PLOT

To determine the upconversion behavior under pressure more conclusively, the pressure and intensity dependence experiment is to be refined. Specifically, measures must be taken to limit the time the sample is exposed to the high-intensity excitation laser. Besides yielding reliable values for the threshold intensity, this refinement would allow the absolute photoluminescence curves to be compared and statements to be made about the efficiency of the system. Protection of the sample could be achieved using a mechanical shutter in the excitation beam line that would only open briefly for each measurement (in this work, blocking the beam was done manually). Another approach would be to move the beam spot across the sample between measurements, thus limiting the exposure of any particular parcel of ionic liquid to the beam. A material system with higher photo-stability would also be favorable not only for lab testing, but also for potential applications.

5.4.2. TRANSIENT ABSORPTION UNDER PRESSURE

Transient absorption spectroscopy would provide a wealth of data about the system by effectively revealing the absorption spectra of excited states, including triplet excitons and the multiexciton [160]. In addition to elucidating the upconversion mechanics at ambient conditions, the experiment could be done with the pressure cell to characterize how the mechanics change with pressure.

5.4.3. MAGNETIC FIELD MEASUREMENTS UNDER PRESSURE

Pressure was hypothesized to force the molecules in the liquid into a more ordered state, thus rendering the spin statistics of TTA more alike to a solid-state system. This could be confirmed by repeating the magnetic field dependence experiment under pressure and comparing the intensity curves. If the initial increase in the upconversion PL becomes more pronounced, it would provide evidence for more solid-like behavior and could explain the possibly increased threshold intensity at high pressure.

5.4.4. STRUCTURAL STUDIES UNDER PRESSURE

When reasoning about the bicontinuity of the liquid and the orientation of its molecules, a clear picture of the structure would be most helpful. Nuclear magnetic resonance (NMR) experiments might be able to provide this information. In NMR, the sample is subjected to a magnetic field sufficiently strong to affect the energies of the spin states of the atomic nuclei and the degree of splitting of the energy levels is probed using radio waves. NMR experiments can assess the chemical structure and purity of compounds, as was done at Kyushu University to verify the successful synthesis of the components of the ionic liquid. A NOESY (nuclear Overhauser effect spectroscopy) experiment can reveal the proximity in real space of the different protons (hydrogen nuclei) in a given substance. This information could be used to determine the typical orientations that

the DPA chromophores assume. In addition, there is precedent for NMR at pressure ranges similar to that used in this study [178] so that this structural information could be acquired for the entire pressure range and any changes in molecular ordering revealed.

5.5. METHODS

Sample preparation and pressure application: All substrates were 15 × 15 mm fused quartz slides that were sonicated in deionized water and detergent for 15 minutes, washed with deionized water, sonicated in acetone for 15 minutes, washed with isopropanol, and treated with oxygen plasma at 100 W for 10 minutes. All cover slips used were 15 × 15 mm borosilicate glass slips and were cleaned in the same manner. Sample preparation is performed under an inert atmosphere. For the UV-vis absorption measurements, the ionic liquid was used as received from Kyushu University and placed between two substrates using a syringe needle. The thickness was reduced by pressing the slides together with 100 N of force for three hours, at a temperature of 70 °C under inert atmosphere. This approach is necessary because dilution is no option for studying the properties of the neat liquid. Both the pure ionic liquid and the ionic liquid with PtOEP were prepared as described above.

For the magnetic field dependent upconversion photoluminescence (UCPL) measurements, the ionic liquid sample with PtOEP was used as received from Kyushu University. A droplet was applied to a substrate using a needle and covered with a cover glass. For the pressure and intensity dependent UCPL, the sample of ionic liquid with PtOEP was re-dissolved in dichloromethane under inert atmosphere and dried in high vacuum by heating to 70 °C for 3 hours under vacuum before use, to avoid aggregation of the PtOEP. A droplet of the sample was then applied to a substrate using a needle and covered with a cover glass. Pressure was applied to the samples using an ISS stainless steel pressure cell with sapphire windows and manual pump, using FC-72 (perfluorohexane) as the pressure fluid. After each pressure point was reached, the system was left to equilibrate for 10 minutes before starting the corresponding measurement. All pressures reported are gauge pressures, measured relative to ambient pressure.

UV-vis absorption: The sample was placed in the pressure cell, which was mounted in a PerkinElmer Lambda 750 UV-Vis-NIR absorption spectrometer. The absorption spectrum between 200 and 600 nm was measured with wavelength increments of 0.5 nm, at pressures between 0 and 400 MPa in 50 MPa increments on the up stroke and 100 MPa decrements on the downstroke to measure any hysteresis. This was done with both the pure ionic liquid and the ionic liquid with PtOEP.

Spectra were further analyzed by fitting a system of five Gaussian peaks to the absorption structure between 300 and 450 nm, using photon energy rather than wavelength on the x-axis. The peak central energies, peak widths at half maximum (FWHM), and relative peak areas were compared at every pressure point.

Magnetic field dependence of upconversion photoluminescence: The sample was mounted between the poles of an electromagnet (GMW Magnet Systems, model 3470)

and illuminated with a 532 nm laser (same as above) at 1.00 mW, which was focused onto the sample using a 100 mm focal length lens. The upconverted light was focused with a 30 mm focal length lens, passed through a 500 nm short pass filter and coupled into a multi-mode optical fiber. This fiber coupled the light into the spectrometer (same as above). The dependence of the magnetic field between the poles on the electric current applied to the magnet was determined using a gaussmeter (AlphaLab Inc., model GM-1-ST). The current in the electromagnet was varied from 0 to 4 A in increments of 200 mA, and back to 0 A in decrements of 1000 mA. At each magnetic field strength, the upconversion spectrum was recorded with an integration time of 1 s. The upconversion spectra were analyzed by background subtraction and by integrating the counts between 400 and 500 nm. This gave the UCPL intensity for every magnetic field strength.

Pressure and intensity dependence of upconversion photoluminescence: The sample was placed in the pressure cell at 45 degrees with respect to the excitation laser (532 nm, 147.5 mW, Laserglow Technologies), which was passed through a continuously variable optical density filter and focused onto the sample with a 100 mm focal length lens. The upconverted light from the sample was focused with a 30 mm focal length lens, passed through a 500 nm shortpass filter and coupled into a multi-mode optical fiber. This fiber coupled the light into the spectrograph (Princeton Instruments Acton SpectraPro 2300i) with liquid nitrogen cooled CCD sensor (Princeton Instruments LN/CCD).

Due to scattering effect in the pressure fluid at pressures greater than 250 MPa, the upconversion spectra were recorded at pressures between 0 and 200 MPa in 25 MPa increments on the up stroke and 50 MPa decrements on the down stroke to measure any hysteresis. For each up stroke measurement, the excitation intensity was varied exponentially, doubling the intensity each time, between 0.5 μW and 4096 μW by adjusting the variable density filter and by adding and removing an additional neutral density filter with optical density 3.0. On the down stroke, the intensity was varied between 1 μW and 4096 μW with eightfold increments. The intensity was verified using an optical power meter (Thorlabs PM200) whose photodiode was on a flip mount between the neutral density filters and the focusing lens. To obtain suitable spectra across seven orders of magnitude of photoluminescence strength, the integration time on the CCD was varied from 200 s at 0.5 and 1 μW of excitation power, to 20 s at 2 and 4 μW, to 2 s at 8 and 16 μW, to 200 ms between 32 and 256 μW, to 20 ms between 512 and 4096 μW.

The beam spot was characterized after the measurement by removing the pressure cell and placing a CCD beam profiler (Thorlabs BC106N) in the beam line at the position of the image of the sample, considering the different refractive indices of air, sapphire and perfluorohexane. Dense media reduce the apparent depth of immersed objects proportionally to their refractive index when the interfaces are flat, so 6.4 mm of sapphire (n = 1.76 [179]) window appears the same as 3.64 mm of air. Similarly 11 mm of perfluorohexane (n = 1.25 [179]) appears as 8.8 mm of air. The apparent position of the sample is thus 4.96 mm closer to the entry window than the actual position and the beam profiler was placed at this apparent position. The effective spot diameter was then determined by the $1/e^2$ level of the marginal distributions of the beam power as in [168], while ac-

counting for the elliptical shape of the spot due to the angle of incidence.

The UCPL intensity was obtained from each spectrum by background subtraction and integration of the spectral range between 400 and 500 nm. These values were divided by the integration time to give a uniform measure of UCPL intensity. The threshold intensity was found by fitting linear functions of slope two and one respectively to the four lowest and highest values of the logarithms of the UCPL intensity and excitation intensity. For the measurements taken on the down stroke, instead the two lowest and highest values were taken. The intersection of the two linear functions gave the threshold intensity.

6

Application perspective: Singlet fission sensitized perovskite solar cells

6.1. SINGLET FISSION SENSITIZED PEROVSKITE SOLAR CELLS

In pervious chapters we discussed the fundamental aspects of singlet fission in organic semiconductors and hybrid perovskites. Taking the potential of both into consideration, we propose a singlet fission sensitized perovskite solar cell which can potentially lead to highly efficient solar cells with low production costs.

6.1.1. WORKING PRINCIPLE AND BENEFITS

The schematic structure of a singlet fission sensitized perovskite solar cell is shown in Figure 6.1 and is similar to quantum dot solar cell sensitized by singlet fission [180]. The light is first transmitted through a transparent conducting electrode and absorbed in the singlet fission layer. The photons with energies lower the bandgap of the singlet fission materials are not absorbed and transmitted to the perovskite layer.

The high-energy light absorbed in the singlet fission layer generates singlet excitons. The singlet excitons undergo singlet fission and generate low-energy triplet excitons. The triplet excitons are then transported to the interface, either transfer their energy to the perovskite layer for charge generation or dissociate in to free charges at the interface and inject one of the charges into the perovskite layer. An interlayer may need to be inserted in between the singlet fission layer and the perovskite layer to enhance the charge/energy transfer efficiency. The charges generated in the perovskite layer are then transported to the corresponding electrodes and collected.

The biggest benefit of singlet fission sensitized solar cells compared to a conventional single-junction solar cell is the significant reduction in thermalization losses. As the high-energy photons can generate a maximum of two electron-hole pairs, the photocurrent of such devices will be enhanced without suffering from voltage losses, leading to overall a higher efficiency. Additionally, as the high-energy, especially the ultraviolet photons are absorbed in the singlet fission layer before reaching the perovskite layer, the stability of the perovskite layer may be improved. Compared to multi-junction solar cells, singlet fission sensitized perovskite solar cells show advantages in the following aspects: first, there is no requirement for current matching, simplifying the device fabrication process; second, all the layers of the device are present in the form of thin films, making the fabrication of flexible devices a possibility; last but not least, many of the layers are, in principle, solution processable, which could lead to a reduction in the cost of production. In addition to the practical benefits, the singlet fission sensitized perovskite solar cells can have multiple colours other than the black or blue colour of traditional silicon solar cells, making them more appealing for applications like building-integrated photovoltaics.

6.1.2. MATERIAL REQUIREMENTS

For an efficiently working device, several requirements need to be fulfilled at the same time: a highly efficient singlet fission material with ideally near-unity triplet yield, a

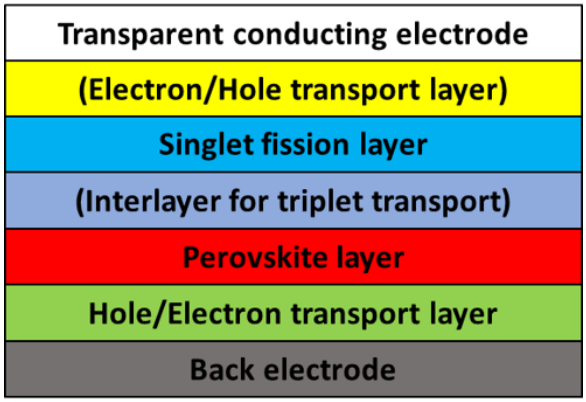

Figure 6.1: Schematic structure of a singlet fission sensitized perovskite solar cell.

triplet energy close to the bandgap of perovskite and efficient triplet energy or charge transfer from the singlet fission layer to the perovskite layer. Additionally, the energy levels of all the materials need to be suitable for charge extraction.

Near-unity singlet fission efficiency has been discovered in a variety of materials, including pentacene, tetracene, and 1, 3-diphenylisobenzofuran [21, 137, 181]. The triplet energy of pentacene is around 0.86 eV [182], which is too low for energy transfer into most perovskite absorbers (with a bandgap of 1.2 eV or higher) that are suitable for efficient photovoltaics. The triplet energy of 1, 3-diphenylisobenzofuran is higher than 1.5 eV, however the high triplet yield can only be reached at low temperature (around 77 K), which makes it difficult for application in realistic devices [137]. The extremely high sensitivity of 1, 3-diphenylisobenzofuran to oxygen further impedes the application in devices [183]. Tetracene has a triplet energy of 1.25 eV [37], making it suitable for energy transfer into low-bandgap perovskites. Also, film formation of tetracene is well-studied, and many derivatives such as TIPS-tetracene allow for solution processing. Tetracene is, however, not very stable, and novel singlet fission materials with a similar triplet energy, such as perylene diimide derivatives [184] and terrylenes [185] are more stable but fabrication protocols are currently less well-established.

The low-bandgap perovskite solar cells currently have lower efficiencies (around 17 %) [186] and low stability compared to solar cells based on perovskites with higher bandgap. Most research is currently focused on the top cell for a perovskite/silicon tandem geometry, which requires a larger bandgap. Considering the quick development of these perovskite solar cells it is feasible to assume a similarly quick development of low-bandgap perovskites once the need arises.

The best performing perovskite solar cells are fabricated with either methylammonium lead iodide (bandgap of 1.61 eV) [56] or perovskites with mixed A-site cations and halides (bandgap of 1.7 eV) [187]. Aiming for the highest efficiency of the singlet fission

sensitized perovskite solar cells based on these materials, highly stable singlet fission materials that have a triplet energy higher than 1.5 eV and near unity triplet yield need to be developed. It has been suggested that the rate and efficiency of singlet fission will be greatly enhanced if the fission process is exothermic, i.e. $2E(T_1)<E(S_1)$, as it can outcompete other decay channels. The energy difference between the singlet and triplet originates from the exchange energy, which scales with the overlap between the lowest unoccupied molecular orbital (LUMO) and the highest occupied molecular orbital (HOMO) of a molecule. For efficient singlet fission, the molecule's LUMO and HOMO should have ample overlap so that the $2E(T_1)<E(S_1)$ requirement is met, yet the difference is not too large so that the triplet energy is not too low. Considering the recent success of designing thermally activated delayed fluorescence (TADF) molecules [188] where the difference between the singlet and triplet energy is minimized by spatially separating the LUMO and HOMO, the opposite direction, aiming for a higher overlap between the LUMO and HOMO should not be impossible. We note, however, that for a triplet energy around 1.5 eV, the exchange energy needs to be on a similar level, something that is rarely observed even in relatively symmetric molecules such as the polyacene series. In addition to methods like density functional theory, the search for novel singlet fission materials may be greatly accelerated with the astonishing development in computer science, especially in machine learning and artificial intelligence.

Highly efficient triplet transfer from polyacenes to lead chalcogenide nanocrystals have been demonstrated [36, 37]. Yet, efficient triplet transfer to bulk semiconductors like silicon seems to remain elusive [189]. Charge trasnfer from TIPS-pentacene to methylammonium lead iodide perovskite [190] has been reported while trial on triplet transfer from tetracene to low bandgap perovskite shows no significant energy transfer [191]. Thus, an interlayer may be needed to facilitate and improve the transfer efficiency. Colloidal nanocrystals may be used in the interlayer for a radiative energy transfer [192]. Two-dimensional (2D) materials, such as transition metal dichalcogenides, graphene oxide or hexagonal boron nitride could be another option. As the wavefunction of the triplet excitons is relatively localized, 2D materials may help to increase the wavefunction overlap between the triplets and the perovskite layer. For materials in which singlet fission is endothermic, e.g. tetracene, the prevention of radiative and non-radiative singlet transfer also needs to be considered. A triplet-transporting singlet-blocking layer may help to reduce the probability of singlet transfer [193].

6.1.3. STABILITY

While commercial silicon solar panels have proven more than 20 years of lifetime, perovskite solar cells are still less stable, despite considerable improvements [194]. Adding an organic singlet fission layer on top will no doubt further increase the difficulty of maintaining a stable device. Here we discuss a few approaches that might be helpful for building a stable singlet fission sensitized perovskite solar cell. For the singlet fission layer, despite the fact that efficient singlet fission has been discovered in disordered molecular systems, a highly ordered packing of the singlet fission molecules will enhance the overall resistance to photo-degradation as well as the transport of ex-

cited states [195]. Due to the intrinsic vulnerability of organic semiconductors to photodegradation, it might be worth considering building the singlet fission part of the device in a detachable way so that it can be easily replaced when its lifetime is reached. For the perovskite part of the device, organic transport layers should be avoided if possible. The organic cations in the perovskite layer should be partly or fully replaced by inorganic cations. Ion migration in the device should also be minimized. For the whole device, encapsulation is a vital step towards high stability. A highly compact encapsulation that has ultralow gas and water permeability is desirable. In addition to the conventional encapsulation methods used for silicon solar cells, methods like atomic layer deposition may be utilized for a more robust encapsulation. If a completely stable and efficient singlet fission material can be found, then the singlet fission layer in itself could act as an encapsulation for the perovskite underneath, because the organic layers are often highly compact and hydrophobic.

SUMMARY

While inorganic semiconductors still play important roles in industry and our daily lives, various types of organic and organic-inorganic hybrid semiconductors are gradually rising either as alternative or complementary materials for the inorganic semiconductors in electronics and optoelectronics, with more being developed and improved. First devices based on organic and hybrid semiconductors, such as organic light-emitting diodes (OLEDs), have been integrated into our daily lives.

To further improve the performance of such devices and reduce the production costs, a clear and thorough understanding of the fundamental aspects of organic and hybrid semiconductors is needed. As the structure of these materials determines their properties to a large extend, it is important to understand the structure-property relationship of these materials.

Hydrostatic pressure is a powerful tool for manipulating the structure of a material while maintaining other factors like temperature, shape, ordering etc.. By studying the optoelectronic properties of organic and hybrid semiconductors under pressure, a clear structure-property relationship can be established. This understanding is not only interesting for the research community, but also beneficial for the optimization of devices based on these materials and the development of new materials with improved properties.

In this thesis, we apply mild pressure on device-scale organic and hybrid semiconductor samples with a special focus on organic and inorganic hybrid perovskites and small organic molecular crystals and perform steady-state and time-resolved optical measurements to study the absorption, emission and charge carrier/exciton dynamics in these material systems. We begin with an introduction to the materials and discuss the problems that need to be solved. We then motivate the use of hydrostatic pressure.

In Chapter 2, we focus on the Rashba-splitting in the prototypical perovskite material for photovoltaics, methylammonium lead triiodide (MAPI) under pressure. We found experimental evidence for the existence of Rashba splitting in MAPI from steady-state photoluminescence and photothermal deflection measurements, suggesting that MAPI might have a slightly indirect bandgap as predicted by theory. With increasing pressure, an increase in recombination rates and radiative efficiency from photoluminescence lifetime measurements is consistent with the picture of a reduction of Rashba splitting. A phase transition occurs at 325 MPa, leading a purely direct bandgap semiconductor. Our results provide a possible explanation for the coexistence of a high absorption and a long carrier lifetime in MAPI, and insights into developing semiconductors with engineered bandstructure.

In Chapter 3, we switch to a lower dimensional perovskite, namely the two-dimensional perovskites. Through steady-state optical measurements under pressure we find that the response of the 2D perovskites strongly depends on the length of the spacer between the lead halide octahedra sheets. Most of the compression under pressure is absorbed by the spacer layer. For the system with short spacers, the quantum confinement effect is relaxed under pressure, presumably due to a leakage of the wavefunction into the neighboring sheets, while the system with long spacers appears insensitive to applied pressure. This is because the long spacer separates the wavefunction to within the sheets, even at high pressure. We find no evidence for Rashba splitting in the any of the monolayer 2D perovskites, at ambient and elevated pressure from the time-resolved measurements. We propose future experiments on multilayer 2D perovskites for a more thorough study on Rashba splitting in 2D perovskites.

We change our focus to small organic molecules capable of singlet fission, namely rubrene, in Chapter 4. We study the influence of intermolecular electronic coupling on the rate and efficiency of singlet fission by applying hydrostatic pressure on amorphous and polycrystalline thin films of rubrene. Singlet fission is a carrier multiplication processes by which a single spin-singlet exciton is converted into two triplet excitons. The steady-state measurements under pressure show no significant change in singlet energy for the amorphous rubrene, while the singlet energy of crystalline rubrene red-shifts by 50 meV. PL lifetime measurements suggest that the efficiency of singlet fission increases by 8 per cent for amorphous rubrene with pressure up to 400 MPa, while a slower dissociation of the triplet pair is observed in crystalline rubrene. Our results suggest that an increase in electronic coupling between singlet fission chromophores might play a different role in molecular systems with different morphology and a balance between energetics and electronic coupling needs to be considered for the designing of efficient singlet fission materials.

In Chapter 5, we investigate the role of microstructure on the light upconversion efficiency of an ionic liquid system. The mechanism of upconversion here is triplet-triplet annihilation, the inverse process of singlet fission. We find the electronic coupling between the chromophores is enhanced with increasing pressure. Despite the liquid nature, the response of the system is highly solid-like in the magnetic field. The changes in upconverting properties under pressure, especially the threshold intensity for upconversion, are rendered inconclusive due to the degradation in the sensitizers induced by photo-bleaching and photo-oxidation. A more clean and stable material is needed for fully understanding the properties of upconversion under pressure.

In Chapter 6, we propose a singlet fission sensitized perovskite solar cell as a potentially cheap and efficient alternative for market-dominating silicon solar cells. We discuss the working principle and the potential benefits of such devices and formulate requirements for the materials and suggestions for improving stability of the devices.

In summary, we demonstrate the power of hydrostatic pressure for studying the structure-

property relationship of organic and hybrid semiconductors. Even mild pressure can significantly change the properties of an organic/hybrid material. The results of this thesis provide insights into design of novel organic/hybrid semiconductors, and suggests potential approaches of improving (flexible) devices by building-in strain, for example by epitaxial growth of active layers.

SAMENVATTING

Hoewel anorganische halfgeleiders een belangrijke rol spelen in zowel industrie als ons dagelijks leven, komen verschillende types organische en organisch-anorganische hybride halfgeleiders op als alternatieve danwel complementaire materialen voor de anorganische halfgeleiders in elektronica en opto-elektronica. Daarnaast worden steeds meer organische en hybride halfgeleiders ontwikkeld en verbeterd. De eerste apparaten gebaseerd op organische en hybride halfgeleiders worden reeds in ons dagelijks leven toegepast, bijvoorbeeld als organische licht-emitterende diodes (OLEDs).

Om de prestaties van dergelijke toepassingen te verbeteren en de productiekosten te verminderen, is een volledig begrip van de fundamentele aspecten van organische en hybride halfgeleiders nodig. Omdat de structuur van deze materialen de eigenschappen voor een groot deel bepaalt, is het belangrijk om de relatie tussen de eigenschappen en de structuur van deze materialen te begrijpen. Hydrostatische druk is een krachtig instrument om de structuur van een materiaal te manipuleren, terwijl andere factoren als temperatuur, vorm en ordening constant blijven. Door de opto-elektronische eigenschappen van organische en hybride halfgeleiders onder druk te bestuderen, kan een duidelijke relatie tussen de structuur en de eigenschappen van het materiaal vastgesteld worden. Het begrijpen van deze relatie is niet alleen interessant voor de academische gemeenschap, maar ook voordelig voor de optimalisatie van toepassingen gebaseerd op deze materialen en de ontwikkeling van nieuwe materialen met verbeterde eigenschappen.

In dit proefschrift bestuderen we verschillende organische en hybride halfgeleiders, op de schaal van potentiële toepassingen, onder milde druk, waarbij we ons in het bijzonder toeleggen op organische en inorganische hybride perovskieten en kristallen van kleine organische moleculen We voeren steady-state en tijdsopgeloste optische metingen uit om de absorptie, emissie en dynamiek van ladingsdragers/excitonen in deze systemen te bestuderen. We beginnen met een introductie van de materialen en bespreken de problemen die opgelost moeten worden, waarna het gebruik van hydrostatische druk gemotiveerd wordt.

In hoofdstuk 2 leggen wij ons toe op de Rashbasplitsing onder druk in het prototypische perovskiet materiaal voor fotovoltaïsche toepassingen: methylammonium lood tri-jodide (MAPI). We vonden experimenteel bewijs voor de aanwezigheid van Rashbasplitsing in MAPI met behulp van steady-state fotoluminescentie- en fotothermische afbuigingsmetingen, die aanduidden dat MAPI een licht indirecte band gap heeft, zoals wordt voorspeld door theorie. De toename van recombinatiesnelheid en stralingsefficiëntie veroorzaakt door een toename van druk is consistent met een vermindering van Rashbasplitsing. Bij 325 MPa doet zich een faseverandering voor, wat leidt tot een puur

directe band gap halfgeleider. Onze resultaten geven een mogelijke uitleg voor de coexistentie van een hoge absorptie en een lange levensduur van ladingsdragers in MAPI, evenals inzichten voor de ontwikkeling van halfgeleiders met een ontworpen bandstructuur.

In hoofdstuk 3 verleggen we onze focus naar een perovskiet met een lagere dimensie, namelijk de tweedimensionale perovskieten. Met optische steady-state metingen onder druk vinden we dat de reactie van 2D perovskieten sterk afhangt van de lengte van de tussenlaag tussen de octaëders van de loodhalide laag. Het grootste deel van de compressie onder druk wordt geabsorbeerd door deze tussenlaag. Voor systemen met kleine tussenlagen neemt het kwantum opsluitingseffect af onder druk, vermoedelijk door een verspreiding van de golffunctie naar naastgelegen lagen, terwijl het systeem met grotere tussenlagen ongevoelig lijkt te zijn voor uitgeoefende druk. Dit komt door dat de grote tussenlaag de golffunctie scheidt tot in de loodhalide lagen zelf, zelfs onder hoge druk. Met tijdsopgeloste metingen op kamer- en verhoogde druk vinden we geen bewijs voor Rashbasplitsing in de enkellaagse 2D perovskieten. We stellen toekomstige experimenten voor op meerlaagse 2D perovskieten voor een grondigere bestudering van Rashbasplitsing in 2D perovskieten.

We verleggen in hoofdstuk 4 onze focus naar kleine organische moleculen, namelijk rubreen, dat tot singlet splitsing in staat is. We bestuderen de invloed van intermoleculaire elektronische koppeling op de snelheid en efficiëntie van singlet splitsing door een hydrostatische druk uit te oefenen op amorfe en polykristallijne dunne films van rubreen. Singlet splitsing is een proces waarbij ladingsdragers vermenigvuldigd worden doordat een enkel spin-singlet exciton wordt omgezet naar twee spin-triplet excitonen. De steady state metingen onder druk laten geen significante verandering zien in de singlet energie van amorf rubreen, terwijl de singlet energie van kristallijn rubreen een roodverschuiving ondergaat van 50 meV. Metingen van de fotoluminescentielevensduur onder druk tot en met 400 MPa duiden erop dat de efficiëntie van singlet splitsing stijgt met 8 procent voor amorf rubreen, terwijl langzamere dissociatie van het triplet paar wordt geobserveerd in kristallijn rubreen. Onze resultaten geven aan dat een toename van elektronische koppeling tussen singlet splitsende chromoforen een verschillende rol zouden kunnen spelen in moleculaire systemen met verschillende morfologie en dat een balans tussen energetica en elektronische koppeling in overweging genomen moet worden bij het ontwerpen van efficiënte singlet splitsende materialen.

In hoofdstuk 5 onderzoeken we de rol van de microstructuur bij de opconversie-efficiëntie van een vloeibaar ionisch systeem. In dit systeem is het mechanisme van opconversie de samenvoeging van twee triplets, het omgekeerde proces van singlet splijting. We vinden dat de elektronische koppeling tussen de chromoforen wordt versterkt met een toenemende druk. Ondanks zijn vloeibare aard, is de reactie van het systeem op een magnetisch veld sterk gelijkend op die van een vaste stof. De veranderingen in de eigenschappen van de opconversie onder druk, met name de intensiteitsdrempel voor opconversie, worden als niet eenduidig afgedaan door de degradatie in de sensitizer, die wordt veroorzaakt door fotobleking en foto-oxidatie. Een zuiverder en stabieler materi-

aal is nodig om de eigenschappen van upconversion onder druk volledig te begrijpen.

In hoofdstuk 6 stellen we een singlet fission sensitized perovskiete zonnecel voor als een potentieel goedkoop en efficiënt alternatief voor de dominerende silicium zonnecel. We bespreken het principe en de potentiële voordelen van deze cellen en formuleren een pakket van eisen voor de materialen en doen suggesties om de stabiliteit te verbeteren.

Samenvattend hebben we de kracht gedemonstreerd van het gebruik van hydrostatische druk om de relatie tussen structuur en eigenschappen van organische en hybride halfgeleiders te bestuderen. Zelfs lichte druk kan de eigenschappen van een organisch/hybride materiaal significant veranderen. De resultaten van dit proefschrift verschaffen inzichten in het ontwerp van nieuwe organische/hybride halfgeleiders en stellen strategieën voor om (flexibele) apparaten te verbeteren door deformaties in te bouwen, bijvoorbeeld door epitaxiale groei van actieve lagen.

ACKNOWLEDGEMENTS

This thesis would not have been possible without the help of many people. I would like to take the opportunity to express my gratitude to all the people who have kindly provided their support.

First of all, I am indebt to my supervisor, Bruno Ehrler. I am grateful for the opportunity to be the first PhD student in your group. Your careful planning of the lab and projects made a smooth start of my PhD without delay. And you gave me ample freedom for the research topics and great patience when I am learning new techniques. Moreover, you gave me the opportunity to attend many international conferences and introduced me to many great collaborators. Most importantly, you showed me the interdisciplinarity of science and the courage to tackle challenging scientific questions. I sincerely thank you for these experiences and believe that they are valuable for my future career.

The opportunity to do my PhD at AMOLF would not have been possible without the Light Management in New Photovoltaic Materials (LMPV) programme, which is initiated and managed by Albert Polman. Albert, thank you for being my promotor and organizing the scientific and social activities of LMPV. I also would like to thank the other two group leaders of LMPV, Erik Garnett and Esther Alarcon Llado. Thank you for fostering a collaborative environment and kindly giving me access to the equipment in your labs.

As the first student of the Hybrid Solar Cells group, I had the opportunity to witness the lab from empty to fully packed and to work with many group members. I would like to thank the two master students that I have worked with, Benjamin Daiber and Arnoud Jongeling. Benjamin, it was a great pleasure to work with you and to see you staying as a PhD student in the group. Thank you for your help with the TCSPC setup, Mathematica and many discussions that we had, which I learned a lot from. Arnoud, thank you for your hard effort on the ionic liquid project and your contributions to the designing of the magnet for the pressure cell. Thanks also go to Ju Min Lee for the help with evaporator and chats on Eastern Asian topics and Christian Dieleman for the help with Schlenk line. And it was fun to do experiments with Moritz Futscher, Maria Mione, Maarten Mennes and Stefan Tabernig. Thanks to Joris Bodin and Christian Dieleman for translating the summary of this thesis to Dutch. It was also a pleasure to have Le Yang, Luis Pazos-Outon and Andrew Pun as visitors in the group, who brought valuable knowledge and refreshing atmosphere. Thanks to all the former and current group members for making the group running as it is today.

AMOLF provides an interdisciplinary environment for research, making it possible to learn from scientists with different backgrounds. I would like to thank Sarah Brittman for sharing her knowledge on chemical synthesis and semiconductors, and Alexei Halpin

for the tips and tricks for transient absorption spectroscopy.

Collaboration was an important part of my PhD. At AMOLF, I would like to thank Sander Mann, Jan Versluis, Huib Bakker, Zhou Geng and Said Rodriguez for the opportunity to collaborate on a variety of different topics. I also would like to thank our international collaborators: Aron Walsh and Jarvist Frost from Imperial College London for the collaboration on hybrid perovskites, Shota Hisamitsu and Nobuhiro Yanai from Kyushu University for the collaboration on upconverting ionic liquid and Jiale Feng and Dan Credgington from University of Cambridge for the collaboration on highly efficient OLED materials.

AMOLF has a great support team that saves a lot of trouble for the PhD students, including myself. I would like to thank all the technical support staff, especially Marc Duursma, Hinco Schoenmaker, Andries Lof, Ricardo Struik, Henk-Jan Boluijt, Dirk-Jan Spaanderman, Ivo Klinkert, Luc Blom, Duncan Verheijde, Idsart Attema, Wiebe de Boer, Mark Willemse, Tom Brouwer, Wessel Zwart, Wouter van der Weijden and Wim Brouwer for their technical support and Tatiana van der Ben, Arnelli Scharbaai, Roos Luthart, Reshma Bual and Wouter Harmsen for the help on administrative issues and paper work.

I enjoyed the view from office 2.52 during my PhD as well as the conversations in the office. I would like to thank Timmo van der Beek, Arkabrata Bhattacharya, Christiaan Mennes, Nasim Tavakoli, Chris Hoekmeijer, Noor Veenhoven, Sylvianne Roscam Abbing, Ilse Wenniger, Andrea Pollastri and Eitan Oksenberg for a relaxing working environment in the office.

Finally, I would like to thank my parents and grandparents for their emotional support without which my journey in Amsterdam would not have been possible.

List of Publications

This Thesis is based on the following publications:

3. **T. Wang**, B. Daiber, J. M. Lee, J. Versluis, I. Klinkert, H. J. Bakker, and B. Ehrler, *Modulating singlet fission efficiency in rubrene by external hydrostatic pressure: a clean way to change intermolecular electronic coupling*, submitted. **(Chapter 4)**

2. **T. Wang** and B. Ehrler, *Photophysics of 2D perovskites under pressure*, under preparation. **(Chapter 3)**

1. **T. Wang***, B. Daiber*, J. M. Frost, S. A. Mann, E. C. Garnett, A. Walsh and B. Ehrler, *Indirect to direct bandgap transition in methylammonium lead halide perovskite*, Energy and Environmental Science **10**, 509-515 (2017). (*equal contribution) **(Chapter 2)**

Other publications by the author:

5. M. H. Futscher, J. M. Lee, L. McGovern, L. A. Muscarella, **T. Wang**, M. I. Haider, A. Fakharuddin, L. Schmidt-Mende and Bruno Ehrler, *Quantification of ion migration in $CH_3NH_3PbI_3$ perovskite solar cells by transient capacitance measurements*, under review.

4. S. W. Tabernig*, B. Daiber*, **T. Wang**, B. Ehrler, *Enhancing silicon solar cells with singlet fission: the case for Förster resonant energy transfer using a quantum dot intermediate*, Journal of Photonics for Energy **8(2)**, 022008 (2018). (*equal contribution)

3. L. Song, **T. Wang**, V. Körstgens, W. Wang, N. Saxena, C. J. Schaffer, T. Fröschl, N. Hüsing, S. Bernstorff, P. Müller-Buschbaum, *Wet Imprinting of Channel-Type Superstructures in Nanostructured Titania Thin Films at Low Temperatures for Hybrid Solar Cells*, ChemSusChem **11**, 1179-1186 (2018).

2. L. Song, A. Abdelsamie, C. J. Schaffer, V. Körstgens, W. Wang, **T. Wang**, E. D. Indari, T. Fröschl, N. Hüsing, T. Haeberle, P. Lugli, S. Bernstorff, P. Müller-Buschbaum, *A Low Temperature Route toward Hierarchically Structured Titania Films for Thin Hybrid Solar Cells*, Advanced Functional Materials **26**, 7084-7093 (2016).

1. W. Wang, C. J. Schaffer, L. Song, V. Körstgens, S. Pröller, E. D. Indari, **T. Wang**, A. Abdelsamie, S. Bernstorff and P. Müller-Buschbaum, *In operando morphology investigation of inverted bulk heterojunction organic solar cells by GISAXS*, Journal of Materials Chemistry A **3**, 8324-8331 (2015).

BIBLIOGRAPHY

[1] IPCC, *Global Warming of 1.5° C*, Tech. Rep. (2018).

[2] *Solar Panel Price Index,* (2018).

[3] *Renewable Infrastructure Investment Handbook: A Guide for Institutional Investors*, Tech. Rep. (World Economic Forum, 2016).

[4] *NREL PV Efficiency Chart,* (2018).

[5] W. Shockley and H. J. Queisser, *Detailed balance limit of efficiency of p-n junction solar cells,* J. Appl. Phys. (1961), 10.1063/1.1736034, arXiv:9809069v1 .

[6] T. Tiedje, E. Yablonovitch, G. D. Cody, and B. G. Brooks, *Limiting Efficiency of Silicon Solar Cells,* IEEE Trans. Electron Devices (1984), 10.1109/T-ED.1984.21594.

[7] H. L. Wells, *über die Cäsium- und Kalium-Bleihalogenide,* Z. Für Anorg. Chem. (1893), 10.1002/zaac.18930030124.

[8] A. Kojima, K. Teshima, Y. Shirai, and T. Miyasaka, *Organometal halide perovskites as visible-light sensitizers for photovoltaic cells,* J. Am. Chem. Soc. (2009), 10.1021/ja809598r, arXiv:nn504795v .

[9] M. Liu, M. B. Johnston, and H. J. Snaith, *Efficient planar heterojunction perovskite solar cells by vapour deposition,* Nature (2013), 10.1038/nature12509, arXiv:arXiv:1011.1669v3 .

[10] K. Lin, J. Xing, L. N. Quan, F. P. G. de Arquer, X. Gong, J. Lu, L. Xie, W. Zhao, D. Zhang, C. Yan, W. Li, X. Liu, Y. Lu, J. Kirman, E. H. Sargent, Q. Xiong, and Z. Wei, *Perovskite light-emitting diodes with external quantum efficiency exceeding 20 per cent, Nature*, (2018), 10.1038/s41586-018-0575-3.

[11] Y. Cao, N. Wang, H. Tian, J. Guo, Y. Wei, H. Chen, Y. Miao, W. Zou, K. Pan, Y. He, H. Cao, Y. Ke, M. Xu, Y. Wang, M. Yang, K. Du, Z. Fu, D. Kong, D. Dai, Y. Jin, G. Li, H. Li, Q. Peng, J. Wang, and W. Huang, *Perovskite light-emitting diodes based on spontaneously formed submicrometre-scale structures, Nature*, (2018), 10.1038/s41586-018-0576-2.

[12] B. Zhao, S. Bai, V. Kim, R. Lamboll, R. Shivanna, F. Auras, J. M. Richter, L. Yang, L. Dai, M. Alsari, X. J. She, L. Liang, J. Zhang, S. Lilliu, P. Gao, H. J. Snaith, J. Wang, N. C. Greenham, R. H. Friend, and D. Di, *High-efficiency perovskite–polymer bulk heterostructure light-emitting diodes, Nature Photonics*, (2018), 10.1038/s41566-018-0283-4, arXiv:1804.09785 .

[13] W. A. Dunlap-Shohl, Y. Zhou, N. P. Padture, and D. B. Mitzi, *Synthetic Approaches for Halide Perovskite Thin Films,* Chem. Rev. (2018), 10.1021/acs.chemrev.8b00318.

[14] L. Protesescu, S. Yakunin, M. I. Bodnarchuk, F. Krieg, R. Caputo, C. H. Hendon, R. X. Yang, A. Walsh, and M. V. Kovalenko, *Nanocrystals of Cesium Lead Halide Perovskites ($CsPbX_3$, X = Cl, Br, and I): Novel Optoelectronic Materials Showing Bright Emission with Wide Color Gamut,* Nano Lett. (2015), 10.1021/nl5048779, arXiv:0402594v3 .

[15] H. Zhu, Y. Fu, F. Meng, X. Wu, Z. Gong, Q. Ding, M. V. Gustafsson, M. T. Trinh, S. Jin, and X. Y. Zhu, *Lead halide perovskite nanowire lasers with low lasing thresholds and high quality factors,* Nat. Mater. (2015), 10.1038/nmat4271, arXiv:arXiv:1011.1669v3 .

[16] R. Brenes, D. Guo, A. Osherov, N. K. Noel, C. Eames, E. M. Hutter, S. K. Pathak, F. Niroui, R. H. Friend, M. S. Islam, H. J. Snaith, V. Bulović, T. J. Savenije, and S. D. Stranks, *Metal Halide Perovskite Polycrystalline Films Exhibiting Properties of Single Crystals,* Joule (2017), 10.1016/j.joule.2017.08.006.

[17] D. Shi, V. Adinolfi, R. Comin, M. Yuan, E. Alarousu, A. Buin, Y. Chen, S. Hoogland, A. Rothenberger, K. Katsiev, Y. Losovyj, X. Zhang, P. A. Dowben, O. F. Mohammed, E. H. Sargent, and O. M. Bakr, *Low trap-state density and long carrier diffusion in organolead trihalide perovskite single crystals,* Science (2015), 10.1126/science.aaa2725, arXiv:1409.6478 .

[18] D. H. Cao, C. C. Stoumpos, O. K. Farha, J. T. Hupp, and M. G. Kanatzidis, *2D Homologous Perovskites as Light-Absorbing Materials for Solar Cell Applications,* J. Am. Chem. Soc. (2015), 10.1021/jacs.5b03796.

[19] A. Köhler and H. Bässler, *Electronic Processes in Organic Semiconductors: An Introduction* (2015) arXiv:arXiv:1011.1669v3 .

[20] M. B. Smith and J. Michl, *Singlet fission,* Chem. Rev. (2010), 10.1021/cr1002613, arXiv:arXiv:1011.1669v3 .

[21] M. W. B. Wilson, A. Rao, J. Clark, R. S. S. Kumar, D. Brida, G. Cerullo, and R. H. Friend, *Ultrafast dynamics of exciton fission in polycrystalline pentacene,* J. Am. Chem. Soc. (2011), 10.1021/ja201688h.

[22] S. Singh, W. J. Jones, W. Siebrand, B. P. Stoicheff, and W. G. Schneider, *Laser generation of excitons and fluorescence in anthracene crystals,* J. Chem. Phys. (1965), 10.1063/1.1695695.

[23] C. E. Swenberg and W. T. Stacy, *Bimolecular radiationless transitions in crystalline tetracene,* Chem. Phys. Lett. (1968), 10.1016/0009-2614(68)80087-9.

[24] R. E. Merrifield, P. Avakian, and R. P. Groff, *Fission of singlet excitons into pairs of triplet excitons in tetracene crystals,* Chem. Phys. Lett. (1969), 10.1016/0009-2614(69)80144-2, arXiv:1702.00001 .

[25] N. Geacintov, M. Pope, and F. Vogel, *Effect of magnetic field on the fluorescence of tetracene crystals: Exciton fission,* Phys. Rev. Lett. (1969), 10.1103/PhysRevLett.22.593.

[26] J. J. Burdett and C. J. Bardeen, *The dynamics of singlet fission in crystalline tetracene and covalent analogs, Accounts of Chemical Research,* (2013), 10.1021/ar300191w.

[27] S. N. Sanders, E. Kumarasamy, A. B. Pun, M. L. Steigerwald, M. Y. Sfeir, and L. M. Campos, *Singlet Fission in Polypentacene,* Chem (2016), 10.1016/j.chempr.2016.08.016, arXiv:arXiv:1403.7175v1 .

[28] Y. Kasai, Y. Tamai, H. Ohkita, H. Benten, and S. Ito, *Ultrafast Singlet Fission in a Push-Pull Low-Bandgap Polymer Film,* J. Am. Chem. Soc. (2015), 10.1021/jacs.5b09361.

[29] A. J. Musser, M. Al-Hashimi, M. Maiuri, D. Brida, M. Heeney, G. Cerullo, R. H. Friend, and J. Clark, *Activated singlet exciton fission in a semiconducting polymer,* J. Am. Chem. Soc. (2013), 10.1021/ja405427j.

[30] A. J. Musser, M. Maiuri, D. Brida, G. Cerullo, R. H. Friend, and J. Clark, *The nature of singlet exciton fission in carotenoid aggregates,* J. Am. Chem. Soc. (2015), 10.1021/jacs.5b01130.

[31] D. Dexter, *Two ideas on energy transfer phenomena: Ion-pair effects involving the OH stretching mode, and sensitization of photovoltaic cells,* Journal of Luminescence **18-19**, 779 (1979).

[32] M. C. Hanna and A. J. Nozik, *Solar conversion efficiency of photovoltaic and photoelectrolysis cells with carrier multiplication absorbers,* J. Appl. Phys. (2006), 10.1063/1.2356795.

[33] D. N. Congreve, J. Lee, N. J. Thompson, E. Hontz, S. R. Yost, P. D. Reusswig, M. E. Bahlke, S. Reineke, T. Van Voorhis, and M. A. Baldo, *External quantum efficiency above 100% in a singlet-exciton-fission-based organic photovoltaic cell,* Science (2013), 10.1126/science.1232994, arXiv:20 .

[34] N. J. Thompson, D. N. Congreve, D. Goldberg, V. M. Menon, and M. A. Baldo, *Slow light enhanced singlet exciton fission solar cells with a 126% yield of electrons per photon,* Appl. Phys. Lett. (2013), 10.1063/1.4858176.

[35] L. M. Pazos-Outón, J. M. Lee, M. H. Futscher, A. Kirch, M. Tabachnyk, R. H. Friend, and B. Ehrler, *A Silicon-Singlet Fission Tandem Solar Cell Exceeding 100% External Quantum Efficiency with High Spectral Stability, ACS Energy Letters,* (2017), 10.1021/acsenergylett.6b00678, arXiv:1512.07466 .

[36] M. Tabachnyk, B. Ehrler, S. Gélinas, M. L. Böhm, B. J. Walker, K. P. Musselman, N. C. Greenham, R. H. Friend, and A. Rao, *Resonant energy transfer of triplet excitons from pentacene to PbSe nanocrystals,* Nat. Mater. (2014), 10.1038/NMAT4093.

[37] N. J. Thompson, M. W. B. Wilson, D. N. Congreve, P. R. Brown, J. M. Scherer, T. S. Bischof, M. Wu, N. Geva, M. Welborn, T. V. Voorhis, V. Bulović, M. G. Bawendi, and M. A. Baldo, *Energy harvesting of non-emissive triplet excitons in tetracene by emissive PbS nanocrystals,* Nat. Mater. (2014), 10.1038/nmat4097.

[38] W. L. Chan, M. Ligges, A. Jailaubekov, L. Kaake, L. Miaja-Avila, and X. Y. Zhu, *Observing the multiexciton state in singlet fission and ensuing ultrafast multielectron transfer,* Science (2011), 10.1126/science.1213986, arXiv:1512.00567 .

[39] J. J. Burdett and C. J. Bardeen, *Quantum beats in crystalline tetracene delayed fluorescence due to triplet pair coherences produced by direct singlet fission,* J. Am. Chem. Soc. (2012), 10.1021/ja301683w.

[40] N. Monahan and X.-Y. Zhu, *Charge Transfer–Mediated Singlet Fission,* Annu. Rev. Phys. Chem. (2015), 10.1146/annurev-physchem-040214-121235.

[41] L. R. Weiss, S. L. Bayliss, F. Kraffert, K. J. Thorley, J. E. Anthony, R. Bittl, R. H. Friend, A. Rao, N. C. Greenham, and J. Behrends, *Strongly exchange-coupled triplet pairs in an organic semiconductor,* Nat. Phys. (2017), 10.1038/nphys3908.

[42] M. J. Tayebjee, S. N. Sanders, E. Kumarasamy, L. M. Campos, M. Y. Sfeir, and D. R. McCamey, *Quintet multiexciton dynamics in singlet fission,* Nat. Phys. (2017), 10.1038/nphys3909, arXiv:0611025v2 .

[43] S. H. C. Askes, A. Bahreman, and S. Bonnet, *Activation of a photodissociative ruthenium complex by triplet-triplet annihilation upconversion in liposomes,* Angew. Chem. - Int. Ed. (2014), 10.1002/anie.201309389.

[44] A. Nattestad, Y. Y. Cheng, R. W. Macqueen, T. F. Schulze, F. W. Thompson, A. J. Mozer, B. Fückel, T. Khoury, M. J. Crossley, K. Lips, G. G. Wallace, and T. W. Schmidt, *Dye-sensitized solar cell with integrated triplet-triplet annihilation upconversion system,* J. Phys. Chem. Lett. (2013), 10.1021/jz401050u.

[45] D. Y. Kondakov, T. D. Pawlik, T. K. Hatwar, and J. P. Spindler, *Triplet annihilation exceeding spin statistical limit in highly efficient fluorescent organic light-emitting diodes,* J. Appl. Phys. (2009), 10.1063/1.3273407.

[46] Y. Y. Cheng, T. Khoury, R. G. Clady, M. J. Tayebjee, N. J. Ekins-Daukes, M. J. Crossley, and T. W. Schmidt, *On the efficiency limit of triplet-triplet annihilation for photochemical upconversion,* Phys. Chem. Chem. Phys. (2010), 10.1039/b913243k, arXiv:jz100566u .

[47] X. Jiang, X. Guo, J. Peng, D. Zhao, and Y. Ma, *Triplet–Triplet Annihilation Photon Upconversion in Polymer Thin Film: Sensitizer Design,* ACS Appl. Mater. Interfaces **8**, 11441 (2016).

[48] M. Wu, D. N. Congreve, M. W. B. Wilson, J. Jean, N. Geva, M. Welborn, T. Van Voorhis, V. Bulović, M. G. Bawendi, and M. A. Baldo, *Solid-state infrared-to-visible upconversion sensitized by colloidal nanocrystals,* Nature Photonics **10**, 31 (2015).

[49] S. Dubey, J. N. Sarvaiya, and B. Seshadri, *Temperature dependent photovoltaic (PV) efficiency and its effect on PV production in the world - A review,* in *Energy Procedia* (2013).

[50] R. P. Dias and I. F. Silvera, *Observation of the Wigner-Huntington transition to metallic hydrogen,* Science (2017), 10.1126/science.aal1579, arXiv:1704.07601 .

[51] W. F. Kuhs, E. Hensel, and H. Bartels, *Gas pressure cells for elastic and inelastic neutron scattering,* in *Journal of Physics Condensed Matter* (2005).

[52] W. Chang, G. M. Akselrod, and V. Bulović, *Solid-state solvation and enhanced exciton diffusion in doped organic thin films under mechanical pressure,* ACS Nano (2015), 10.1021/acsnano.5b00938.

[53] Y. Wu, A. R. Chew, G. A. Rojas, G. Sini, G. Haugstad, A. Belianinov, S. V. Kalinin, H. Li, C. Risko, J. L. Brédas, A. Salleo, and C. D. Frisbie, *Strain effects on the work function of an organic semiconductor,* Nat. Commun. (2016), 10.1038/ncomms10270.

[54] L. Etgar, P. Gao, Z. Xue, Q. Peng, A. K. Chandiran, B. Liu, M. K. Nazeeruddin, and M. Grätzel, *Mesoscopic $CH_3NH_3PbI_3/TiO_2$ heterojunction solar cells,* J. Am. Chem. Soc. (2012), 10.1021/ja307789s, arXiv:ja307789s .

[55] H. S. Kim, J. W. Lee, N. Yantara, P. P. Boix, S. A. Kulkarni, S. Mhaisalkar, M. Grätzel, and N. G. Park, *High efficiency solid-state sensitized solar cell-based on submicrometer rutile TiO_2 nanorod and $CH_3NH_3PbI_3$ perovskite sensitizer,* Nano Lett. (2013), 10.1021/nl400286w.

[56] J. H. Im, I. H. Jang, N. Pellet, M. Grätzel, and N. G. Park, *Growth of $CH_3NH_3PbI_3$ cuboids with controlled size for high-efficiency perovskite solar cells,* Nat. Nanotechnol. (2014), 10.1038/nnano.2014.181, arXiv:nn504795v .

[57] G. Xing, N. Mathews, S. S. Lim, N. Yantara, X. Liu, D. Sabba, M. Grätzel, S. Mhaisalkar, and T. C. Sum, *Low-temperature solution-processed wavelength-tunable perovskites for lasing,* Nat. Mater. (2014), 10.1038/nmat3911, arXiv:nmat3911 .

[58] S. Yakunin, M. Sytnyk, D. Kriegner, S. Shrestha, M. Richter, G. J. Matt, H. Azimi, C. J. Brabec, J. Stangl, M. V. Kovalenko, and W. Heiss, *Detection of X-ray photons by solution-processed lead halide perovskites,* Nat. Photonics (2015), 10.1038/nphoton.2015.82.

[59] Y. Bi, E. M. Hutter, Y. Fang, Q. Dong, J. Huang, and T. J. Savenije, *Charge Carrier Lifetimes Exceeding 15 ms in Methylammonium Lead Iodide Single Crystals,* J. Phys. Chem. Lett. (2016), 10.1021/acs.jpclett.6b00269.

[60] Q. Dong, Y. Fang, Y. Shao, P. Mulligan, J. Qiu, L. Cao, and J. Huang, *Electron-hole diffusion lengths 175 mm in solution-grown $CH_3NH_3PbI_3$ single crystals,* Science (2015), 10.1126/science.aaa5760, arXiv:arXiv:1011.1669v3 .

[61] H. S. Kim, C. R. Lee, J. H. Im, K. B. Lee, T. Moehl, A. Marchioro, S. J. Moon, R. Humphry-Baker, J. H. Yum, J. E. Moser, M. Grätzel, and N. G. Park, *Lead iodide perovskite sensitized all-solid-state submicron thin film mesoscopic solar cell with efficiency exceeding 9%,* Sci. Rep. (2012), 10.1038/srep00591.

[62] T. Baikie, Y. Fang, J. M. Kadro, M. Schreyer, F. Wei, S. G. Mhaisalkar, M. Graetzel, and T. J. White, *Synthesis and crystal chemistry of the hybrid perovskite $CH_3NH_3PbI_3$ for solid-state sensitised solar cell applications,* J. Mater. Chem. A (2013), 10.1039/c3ta10518k, arXiv:arXiv:1011.1669v3 .

[63] A. Cuevas and D. Macdonald, *Measuring and interpreting the lifetime of silicon wafers,* Sol. Energy (2004), 10.1016/j.solener.2003.07.033.

[64] D. W. DeQuilettes, S. M. Vorpahl, S. D. Stranks, H. Nagaoka, G. E. Eperon, M. E. Ziffer, H. J. Snaith, and D. S. Ginger, *Impact of microstructure on local carrier lifetime in perovskite solar cells,* Science (2015), 10.1126/science.aaa5333, arXiv:arXiv:1011.1669v3 .

[65] X. Y. Zhu and V. Podzorov, *Charge Carriers in Hybrid Organic-Inorganic Lead Halide Perovskites Might Be Protected as Large Polarons, Journal of Physical Chemistry Letters,* (2015), 10.1021/acs.jpclett.5b02462, arXiv:arXiv:1507.02179v1 .

[66] T. W. Crothers, R. L. Milot, J. B. Patel, E. S. Parrott, J. Schlipf, P. Müller-Buschbaum, M. B. Johnston, and L. M. Herz, *Photon Reabsorption Masks Intrinsic Bimolecular Charge-Carrier Recombination in $CH_3NH_3PbI_3$ Perovskite,* Nano Lett. (2017), 10.1021/acs.nanolett.7b02834.

[67] H. H. Fang, R. Raissa, M. Abdu-Aguye, S. Adjokatse, G. R. Blake, J. Even, and M. A. Loi, *Photophysics of organic-inorganic hybrid lead iodide perovskite single crystals,* Adv. Funct. Mater. (2015), 10.1002/adfm.201404421.

[68] C. Motta, F. E. Mellouhi, S. Kais, N. Tabet, F. Alharbi, and S. Sanvito, *Revealing the role of organic cations in hybrid halide perovskites $CH_3NH_3PbI_3$,* Nat. Commun. (2015), 10.1038/ncomms8026, arXiv:1410.8365 .

[69] F. Brivio, K. T. Butler, A. Walsh, and M. Van Schilfgaarde, *Relativistic quasiparticle self-consistent electronic structure of hybrid halide perovskite photovoltaic absorbers,* Phys. Rev. B - Condens. Matter Mater. Phys. (2014), 10.1103/PhysRevB.89.155204, arXiv:1401.6993 .

[70] T. Etienne, E. Mosconi, and F. De Angelis, *Dynamical Origin of the Rashba Effect in Organohalide Lead Perovskites: A Key to Suppressed Carrier Recombination in Perovskite Solar Cells?* J. Phys. Chem. Lett. (2016), 10.1021/acs.jpclett.6b00564.

[71] M. Kepenekian, R. Robles, C. Katan, D. Sapori, L. Pedesseau, and J. Even, *Rashba and Dresselhaus Effects in Hybrid Organic-Inorganic Perovskites: From Basics to Devices,* ACS Nano (2015), 10.1021/acsnano.5b04409.

[72] F. Zheng, L. Z. Tan, S. Liu, and A. M. Rappe, *Rashba spin-orbit coupling enhanced carrier lifetime in $CH_3NH_3PbI_3$,* Nano Lett. (2015), 10.1021/acs.nanolett.5b01854, arXiv:1505.04212 .

[73] D. Niesner, M. Wilhelm, I. Levchuk, A. Osvet, S. Shrestha, M. Batentschuk, C. Brabec, and T. Fauster, *Giant Rashba Splitting in $CH_3NH_3PbBr_3$ Organic-Inorganic Perovskite,* Phys. Rev. Lett. (2016), 10.1103/PhysRevLett.117.126401, arXiv:1606.05867 .

[74] F. J. Manjón, A. Segura, V. Muñoz-Sanjosé, G. Tobías, P. Ordejón, and E. Canadell, *Band structure of indium selenide investigated by intrinsic photoluminescence under high pressure,* Phys. Rev. B - Condens. Matter Mater. Phys. (2004), 10.1103/PhysRevB.70.125201.

[75] D. Errandonea, E. Bandiello, A. Segura, J. J. Hamlin, M. B. Maple, P. Rodriguez-Hernandez, and A. Muñoz, *Tuning the band gap of $PbCrO_4$ through high-pressure: Evidence of wide-to-narrow semiconductor transitions,* J. Alloys Compd. (2014), 10.1016/j.jallcom.2013.10.179.

[76] T. Ou, J. Yan, C. Xiao, W. Shen, C. Liu, X. Liu, Y. Han, Y. Ma, and C. Gao, *Visible light response, electrical transport, and amorphization in compressed organolead iodine perovskites,* Nanoscale (2016), 10.1039/c5nr07842c.

[77] A. Jaffe, Y. Lin, C. M. Beavers, J. Voss, W. L. Mao, and H. I. Karunadasa, *High-pressure single-crystal structures of 3D lead-halide hybrid perovskites and pressure effects on their electronic and optical properties,* ACS Cent. Sci. (2016), 10.1021/acscentsci.6b00055, arXiv:arXiv:1011.1669v3 .

[78] S. Jiang, Y. Fang, R. Li, H. Xiao, J. Crowley, C. Wang, T. J. White, W. A. Goddard, Z. Wang, T. Baikie, and J. Fang, *Pressure-dependent polymorphism and band-gap tuning of methylammonium lead iodide perovskite,* Angew. Chem. - Int. Ed. (2016), 10.1002/anie.201601788.

[79] L. Kong, G. Liu, J. Gong, Q. Hu, R. D. Schaller, P. Dera, D. Zhang, Z. Liu, W. Yang, K. Zhu, Y. Tang, C. Wang, S.-H. Wei, T. Xu, and H.-k. Mao, *Simultaneous band-gap narrowing and carrier-lifetime prolongation of organic–inorganic trihalide perovskites,* Proc. Natl. Acad. Sci. (2016), 10.1073/pnas.1609030113.

[80] P. Azarhoosh, S. McKechnie, J. M. Frost, A. Walsh, and M. Van Schilfgaarde, *Research Update: Relativistic origin of slow electron-hole recombination in hybrid halide perovskite solar cells,* APL Mater. (2016), 10.1063/1.4955028, arXiv:1604.04500 .

[81] M. L. Petrus, T. Bein, T. J. Dingemans, and P. Docampo, *A low cost azomethine-based hole transporting material for perovskite photovoltaics,* J. Mater. Chem. A (2015), 10.1039/c5ta03046c.

[82] J. Feng, *Mechanical properties of hybrid organic-inorganic $CH_3NH_3BX_3$ (B = Sn, Pb; X = Br, I) perovskites for solar cell absorbers,* APL Mater. (2014), 10.1063/1.4885256.

[83] J. Tauc, *Optical properties and electronic structure of amorphous Ge and Si,* Mater. Res. Bull. (1968), 10.1016/0025-5408(68)90023-8, arXiv:arXiv:1011.1669v3 .

[84] S. H. Wei and A. Zunger, *Electronic and structural anomalies in lead chalcogenides,* Phys. Rev. B - Condens. Matter Mater. Phys. (1997), 10.1103/PhysRevB.55.13605.

[85] J. M. Frost, K. T. Butler, F. Brivio, C. H. Hendon, M. Van Schilfgaarde, and A. Walsh, *Atomistic origins of high-performance in hybrid halide perovskite solar cells,* Nano Lett. (2014), 10.1021/nl500390f, arXiv:1402.4980 .

[86] R. L. Milot, G. E. Eperon, H. J. Snaith, M. B. Johnston, and L. M. Herz, *Temperature-Dependent Charge-Carrier Dynamics in $CH_3NH_3PbI_3$ Perovskite Thin Films,* Adv. Funct. Mater. (2015), 10.1002/adfm.201502340.

[87] K. Wu, A. Bera, C. Ma, Y. Du, Y. Yang, L. Li, and T. Wu, *Temperature-dependent excitonic photoluminescence of hybrid organometal halide perovskite films,* Phys. Chem. Chem. Phys. (2014), 10.1039/c4cp03573a.

[88] G. Grancini, A. R. Srimath Kandada, J. M. Frost, A. J. Barker, M. De Bastiani, M. Gandini, S. Marras, G. Lanzani, A. Walsh, and A. Petrozza, *Role of microstructure in the electron-hole interaction of hybrid lead halide perovskites,* Nat. Photonics (2015), 10.1038/nphoton.2015.151.

[89] J. T. W. Wang, Z. Wang, S. Pathak, W. Zhang, D. W. Dequilettes, F. Wisnivesky-Rocca-Rivarola, J. Huang, P. K. Nayak, J. B. Patel, H. A. Mohd Yusof, Y. Vaynzof, R. Zhu, I. Ramirez, J. Zhang, C. Ducati, C. Grovenor, M. B. Johnston, D. S. Ginger, R. J. Nicholas, and H. J. Snaith, *Efficient perovskite solar cells by metal ion doping,* Energy Environ. Sci. (2016), 10.1039/c6ee01969b, arXiv:arXiv:1103.6228v1 .

[90] D. Li, G. Wang, H. C. Cheng, C. Y. Chen, H. Wu, Y. Liu, Y. Huang, and X. Duan, *Size-dependent phase transition in methylammonium lead iodide perovskite microplate crystals,* Nat. Commun. (2016), 10.1038/ncomms11330, arXiv:arXiv:1011.1669v3 .

[91] E. M. Hutter, M. C. Gélvez-Rueda, A. Osherov, V. Bulović, F. C. Grozema, S. D. Stranks, and T. J. Savenije, *Direct-indirect character of the bandgap in methylammonium lead iodide perovskite,* Nat. Mater. (2017), 10.1038/nmat4765.

[92] V. D'Innocenzo, G. Grancini, M. J. P. Alcocer, A. R. S. Kandada, S. D. Stranks, M. M. Lee, G. Lanzani, H. J. Snaith, and A. Petrozza, *Excitons versus free charges in organo-lead tri-halide perovskites,* Nat. Commun. (2014), 10.1038/ncomms4586, arXiv:arXiv:0710.1245v2 .

[93] C. Wehrenfennig, M. Liu, H. J. Snaith, M. B. Johnston, and L. M. Herz, *Charge carrier recombination channels in the low-temperature phase of organic-inorganic lead halide perovskite thin films,* APL Mater. (2014), 10.1063/1.4891595.

[94] X. Wu, M. T. Trinh, D. Niesner, H. Zhu, Z. Norman, J. S. Owen, O. Yaffe, B. J. Kudisch, and X. Y. Zhu, *Trap states in lead iodide perovskites,* J. Am. Chem. Soc. (2015), 10.1021/ja512833n.

[95] M. T. Weller, O. J. Weber, P. F. Henry, A. M. Di Pumpo, and T. C. Hansen, *Complete structure and cation orientation in the perovskite photovoltaic methylammonium lead iodide between 100 and 352 K,* Chem. Commun. (2015), 10.1039/c4cc09944c.

[96] A. Sadhanala, F. Deschler, T. H. Thomas, S. E. Dutton, K. C. Goedel, F. C. Hanusch, M. L. Lai, U. Steiner, T. Bein, P. Docampo, D. Cahen, and R. H. Friend, *Preparation of single-phase films of $CH_3NH_3Pb(I_{1-x}Br_x)_3$ with sharp optical band edges,* J. Phys. Chem. Lett. (2014), 10.1021/jz501332v.

[97] W. Zhang, M. Saliba, D. T. Moore, S. K. Pathak, M. T. Hörantner, T. Stergiopoulos, S. D. Stranks, G. E. Eperon, J. A. Alexander-Webber, A. Abate, A. Sadhanala, S. Yao, Y. Chen, R. H. Friend, L. A. Estroff, U. Wiesner, and H. J. Snaith, *Ultrasmooth organic-inorganic perovskite thin-film formation and crystallization for efficient planar heterojunction solar cells,* Nat. Commun. (2015), 10.1038/ncomms7142, arXiv:arXiv:1011.1669v3 .

[98] S. De Wolf, J. Holovsky, S. J. Moon, P. Löper, B. Niesen, M. Ledinsky, F. J. Haug, J. H. Yum, and C. Ballif, *Organometallic halide perovskites: Sharp optical absorption edge and its relation to photovoltaic performance,* J. Phys. Chem. Lett. (2014), 10.1021/jz500279b, arXiv:1511.06984 .

[99] M. A. Green, Y. Jiang, A. M. Soufiani, and A. Ho-Baillie, *Optical Properties of Photovoltaic Organic-Inorganic Lead Halide Perovskites, Journal of Physical Chemistry Letters,* (2015), 10.1021/acs.jpclett.5b01865.

[100] M. Saba, M. Cadelano, D. Marongiu, F. Chen, V. Sarritzu, N. Sestu, C. Figus, M. Aresti, R. Piras, A. Geddo Lehmann, C. Cannas, A. Musinu, F. Quochi, A. Mura, and G. Bongiovanni, *Correlated electron-hole plasma in organometal perovskites,* Nat. Commun. (2014), 10.1038/ncomms6049.

[101] F. Deschler, M. Price, S. Pathak, L. E. Klintberg, D. D. Jarausch, R. Higler, S. Hüttner, T. Leijtens, S. D. Stranks, H. J. Snaith, M. Atatüre, R. T. Phillips, and R. H. Friend, *High photoluminescence efficiency and optically pumped lasing in solution-processed mixed halide perovskite semiconductors,* J. Phys. Chem. Lett. (2014), 10.1021/jz5005285, arXiv:arXiv:1011.1669v3 .

[102] C. L. Davies, M. R. Filip, J. B. Patel, T. W. Crothers, C. Verdi, A. D. Wright, R. L. Milot, F. Giustino, M. B. Johnston, and L. M. Herz, *Bimolecular recombination in methylammonium lead triiodide perovskite is an inverse absorption process,* Nat. Commun. (2018), 10.1038/s41467-017-02670-2.

[103] V. Sarritzu, N. Sestu, D. Marongiu, X. Chang, Q. Wang, S. Masi, S. Colella, A. Rizzo, A. Gocalinska, E. Pelucchi, M. L. Mercuri, F. Quochi, M. Saba, A. Mura, and G. Bongiovanni, *Direct or Indirect Bandgap in Hybrid Lead Halide Perovskites?* Adv. Opt. Mater. (2018), 10.1002/adom.201701254.

[104] K. Frohna, T. Deshpande, J. Harter, W. Peng, B. A. Barker, J. B. Neaton, S. G. Louie, O. M. Bakr, D. Hsieh, and M. Bernardi, *Inversion symmetry and bulk Rashba effect in methylammonium lead iodide perovskite single crystals,* Nat. Comm (2018), 10.1038/s41467-018-04212-w.

[105] J. M. Richter, K. Chen, A. Sadhanala, J. Butkus, J. P. Rivett, R. H. Friend, B. Monserrat, J. M. Hodgkiss, and F. Deschler, *Direct Bandgap Behavior in Rashba-Type Metal Halide Perovskites, Advanced Materials,* (2018), 10.1002/adma.201803379.

[106] C. Zheng, S. Yu, and O. Rubel, *Structural dynamics in hybrid halide perovskites: Bulk Rashba splitting, spin texture, and carrier localization,* Phys. Rev. Mater. **2**, 114604 (2018).

[107] D. Niesner, M. Hauck, S. Shrestha, I. Levchuk, G. J. Matt, A. Osvet, M. Batentschuk, C. Brabec, H. B. Weber, and T. Fauster, *Structural fluctuations cause spin-split states in tetragonal (CH_3NH_3)PbI_3 as evidenced by the circular photogalvanic effect,* Proc. Natl. Acad. Sci. (2018), 10.1073/pnas.1805422115.

[108] F. Ambrosio, J. Wiktor, F. De Angelis, and A. Pasquarello, *Origin of low electron-hole recombination rate in metal halide perovskites,* Energy Environ. Sci. (2018), 10.1039/c7ee01981e.

[109] T. Kirchartz and U. Rau, *Decreasing Radiative Recombination Coefficients via an Indirect Band Gap in Lead Halide Perovskites,* J. Phys. Chem. Lett. (2017), 10.1021/acs.jpclett.7b00236.

[110] G. Kresse and D. Joubert, *From ultrasoft pseudopotentials to the projector augmented-wave method,* Phys. Rev. B **59**, 1758 (1999).

[111] F. Brivio, J. M. Frost, J. M. Skelton, A. J. Jackson, O. J. Weber, M. T. Weller, A. R. Goñi, A. M. Leguy, P. R. Barnes, and A. Walsh, *Lattice dynamics and vibrational spectra of the orthorhombic, tetragonal, and cubic phases of methylammonium lead iodide,* Phys. Rev. B - Condens. Matter Mater. Phys. (2015), 10.1103/PhysRevB.92.144308, arXiv:1504.07508 .

[112] J. Mooney and P. Kambhampati, *Get the Basics Right: Jacobian Conversion of Wavelength and Energy Scales for Quantitative Analysis of Emission Spectra,* J. Phys. Chem. Lett. **4**, 3316 (2013).

[113] B. Armstrong, *Spectrum line profiles: The Voigt function,* Journal of Quantitative Spectroscopy and Radiative Transfer **7**, 61 (1967).

[114] A. D. Wright, C. Verdi, R. L. Milot, G. E. Eperon, M. A. Pérez-Osorio, H. J. Snaith, F. Giustino, M. B. Johnston, and L. M. Herz, *Electron–phonon coupling in hybrid lead halide perovskites,* Nature Communications **7**, 11755 (2016).

[115] C. Wehrenfennig, M. Liu, H. J. Snaith, M. B. Johnston, and L. M. Herz, *Homogeneous emission line broadening in the organo lead halide perovskite $CH_3NH_3PbI_{3-x}Cl_x$,* J. Phys. Chem. Lett. **5**, 1300 (2014).

[116] C. Kittel, *Introduction to Solid State Physics 8th edition* (2003).

[117] A. N. Beecher, O. E. Semonin, J. M. Skelton, J. M. Frost, M. W. Terban, H. Zhai, A. Alatas, J. S. Owen, A. Walsh, and S. J. L. Billinge, *Direct Observation of Dynamic Symmetry Breaking above Room Temperature in Methylammonium Lead Iodide Perovskite,* ACS Energy Lett. **1**, 880 (2016).

[118] T. Oku, *Crystal Structures of $CH_3NH_3PbI_3$ and Related Perovskite Compounds Used for Solar Cells* (2015).

[119] J. Tauc, R. Grigorovici, and A. Vancu, *Optical Properties and Electronic Structure of Amorphous Germanium,* physica status solidi (b) **15**, 627 (1966).

[120] E. A. Davis and N. F. Mott, *Conduction in non-crystalline systems V. Conductivity, optical absorption and photoconductivity in amorphous semiconductors,* The Philosophical Magazine: A Journal of Theoretical Experimental and Applied Physics **22**, 0903 (1970).

[121] S. John, C. Soukoulis, M. H. Cohen, and E. N. Economou, *Theory of Electron Band Tails and the Urbach Optical-Absorption Edge,* Phys. Rev. Lett. **57**, 1777 (1986).

[122] S. A. Mann, S. Z. Oener, A. Cavalli, J. E. M. Haverkort, E. P. A. M. Bakkers, and E. C. Garnett, *Quantifying losses and thermodynamic limits in nanophotonic solar cells,* Nature Nanotechnology **11**, 1071 (2016).

[123] S. Leyre, E. Coutino-Gonzalez, J. J. Joos, J. Ryckaert, Y. Meuret, D. Poelman, P. F. Smet, G. Durinck, J. Hofkens, G. Deconinck, and P. Hanselaer, *Absolute determination of photoluminescence quantum efficiency using an integrating sphere setup,* Review of Scientific Instruments **85**, 123115 (2014).

[124] N. Wang, L. Cheng, R. Ge, S. Zhang, Y. Miao, W. Zou, C. Yi, Y. Sun, Y. Cao, R. Yang, Y. Wei, Q. Guo, Y. Ke, M. Yu, Y. Jin, Y. Liu, Q. Ding, D. Di, L. Yang, G. Xing, H. Tian, C. Jin, F. Gao, R. H. Friend, J. Wang, and W. Huang, *Perovskite light-emitting diodes based on solution-processed self-organized multiple quantum wells,* Nat. Photonics (2016), 10.1038/nphoton.2016.185.

[125] E. R. Dohner, A. Jaffe, L. R. Bradshaw, and H. I. Karunadasa, *Intrinsic white-light emission from layered hybrid perovskites,* J. Am. Chem. Soc. (2014), 10.1021/ja507086b.

[126] E. R. Dohner, E. T. Hoke, and H. I. Karunadasa, *Self-assembly of broadband white-light emitters,* J. Am. Chem. Soc. (2014), 10.1021/ja411045r.

[127] E. P. Booker, T. H. Thomas, C. Quarti, M. R. Stanton, C. D. Dashwood, A. J. Gillett, J. M. Richter, A. J. Pearson, N. J. Davis, H. Sirringhaus, M. B. Price, N. C. Greenham, D. Beljonne, S. E. Dutton, and F. Deschler, *Formation of Long-Lived Color Centers for Broadband Visible Light Emission in Low-Dimensional Layered Perovskites,* J. Am. Chem. Soc. (2017), 10.1021/jacs.7b10223, arXiv:NIHMS150003 .

[128] F. Wang, W. Geng, Y. Zhou, H. H. Fang, C. J. Tong, M. A. Loi, L. M. Liu, and N. Zhao, *Phenylalkylamine Passivation of Organolead Halide Perovskites Enabling High-Efficiency and Air-Stable Photovoltaic Cells,* Adv. Mater. (2016), 10.1002/adma.201603062.

[129] H. Tsai, W. Nie, J. C. Blancon, C. C. Stoumpos, R. Asadpour, B. Harutyunyan, A. J. Neukirch, R. Verduzco, J. J. Crochet, S. Tretiak, L. Pedesseau, J. Even, M. A. Alam, G. Gupta, J. Lou, P. M. Ajayan, M. J. Bedzyk, M. G. Kanatzidis, and A. D. Mohite, *High-efficiency two-dimensional ruddlesden-popper perovskite solar cells,* Nature (2016), 10.1038/nature18306.

[130] Y. Zhai, S. Baniya, C. Zhang, J. Li, P. Haney, C. X. Sheng, E. Ehrenfreund, and Z. V. Vardeny, *Giant Rashba splitting in 2D organic-inorganic halide perovskites measured by transient spectroscopies,* Sci. Adv. (2017), 10.1126/sciadv.1700704.

[131] J. Yin, P. Maity, L. Xu, A. M. El-Zohry, H. Li, O. M. Bakr, J. L. Brédas, and O. F. Mohammed, *Layer-Dependent Rashba Band Splitting in 2D Hybrid Perovskites, Chemistry of Materials*, (2018), 10.1021/acs.chemmater.8b03436.

[132] J. Even, L. Pedesseau, and C. Katan, *Understanding quantum confinement of charge carriers in layered 2D hybrid perovskites,* ChemPhysChem (2014), 10.1002/cphc.201402428.

[133] M. T. Frederick and E. A. Weiss, *Relaxation of exciton confinement in CdSe quantum dots by modification with a conjugated dithiocarbamate ligand,* ACS Nano (2010), 10.1021/nn1007435.

[134] L. Ni, U. Huynh, A. Cheminal, T. H. Thomas, R. Shivanna, T. F. Hinrichsen, S. Ahmad, A. Sadhanala, and A. Rao, *Real-Time Observation of Exciton-Phonon Coupling Dynamics in Self-Assembled Hybrid Perovskite Quantum Wells,* ACS Nano (2017), 10.1021/acsnano.7b03984.

[135] T. Wang, B. Daiber, J. M. Frost, S. A. Mann, E. C. Garnett, A. Walsh, and B. Ehrler, *Indirect to direct bandgap transition in methylammonium lead halide perovskite,* Energy Environ. Sci. **10**, 509 (2017).

[136] L. Zhang, L. Wu, K. Wang, and B. Zou, *Pressure-Induced Broadband Emission of 2D Organic–Inorganic Hybrid Perovskite ($C_6H_5C_2H_4NH_3)_2PbBr_4$*, Adv. Sci. **0**, 1801628 (2018).

[137] J. C. Johnson, A. J. Nozik, and J. Michl, *High triplet yield from singlet fission in a thin film of 1,3-diphenylisobenzofuran,* J. Am. Chem. Soc. (2010), 10.1021/ja104123r.

[138] S. R. Yost, J. Lee, M. W. Wilson, T. Wu, D. P. McMahon, R. R. Parkhurst, N. J. Thompson, D. N. Congreve, A. Rao, K. Johnson, M. Y. Sfeir, M. G. Bawendi, T. M. Swager, R. H. Friend, M. A. Baldo, and T. Van Voorhis, *A transferable model for singlet-fission kinetics,* Nat. Chem. (2014), 10.1038/nchem.1945.

[139] A. K. Le, J. A. Bender, D. H. Arias, D. E. Cotton, J. C. Johnson, and S. T. Roberts, *Singlet Fission Involves an Interplay between Energetic Driving Force and Electronic Coupling in Perylenediimide Films,* J. Am. Chem. Soc. (2018), 10.1021/jacs.7b11888.

[140] V. Podzorov, S. E. Sysoev, E. Loginova, V. M. Pudalov, and M. E. Gershenson, *Single-crystal organic field effect transistors with the hole mobility ~8 cm^2/Vs,* Appl. Phys. Lett. (2003), 10.1063/1.1622799, arXiv:0306192 .

[141] H. Aziz and Z. D. Popovic, *Study of organic light emitting devices with a 5,6,11,12-tetraphenylnaphthacene (rubrene)-doped hole transport layer,* Appl. Phys. Lett. **80**, 2180 (2002).

[142] W. A. Yee, V. A. Kuzmin, D. S. Kliger, G. S. Hammond, and A. J. Twarowski, *Quenching of the fluorescent state of rubrene directly to the ground state,* J. Am. Chem. Soc. **101**, 5104 (1979).

[143] L. Ma, K. Zhang, C. Kloc, H. Sun, M. E. Michel-Beyerle, and G. G. Gurzadyan, *Singlet fission in rubrene single crystal: Direct observation by femtosecond pump-probe spectroscopy,* Phys. Chem. Chem. Phys. (2012), 10.1039/c2cp40449d.

[144] V. Jankus, E. W. Snedden, D. W. Bright, E. Arac, D. Dai, and A. P. Monkman, *Competition between polaron pair formation and singlet fission observed in amorphous rubrene films,* Phys. Rev. B - Condens. Matter Mater. Phys. (2013), 10.1103/PhysRevB.87.224202.

[145] K. Miyata, Y. Kurashige, K. Watanabe, T. Sugimoto, S. Takahashi, S. Tanaka, J. Takeya, T. Yanai, and Y. Matsumoto, *Coherent singlet fission activated by symmetry breaking,* Nat. Chem. (2017), 10.1038/nchem.2784.

[146] I. Breen, R. Tempelaar, L. A. Bizimana, B. Kloss, D. R. Reichman, and D. B. Turner, *Triplet Separation Drives Singlet Fission after Femtosecond Correlated Triplet Pair Production in Rubrene,* J. Am. Chem. Soc. (2017), 10.1021/jacs.7b02621.

[147] H. Tsunoyama and A. Nakajima, *Anion Photoelectron Spectroscopy of Rubrene: Molecular Insights into Singlet Fission Energetics,* J. Phys. Chem. C (2017), 10.1021/acs.jpcc.7b06900.

[148] K. Bera, C. J. Douglas, and R. R. Frontiera, *Femtosecond Raman Microscopy Reveals Structural Dynamics Leading to Triplet Separation in Rubrene Singlet Fission,* J. Phys. Chem. Lett. (2017), 10.1021/acs.jpclett.7b02769.

[149] C. Sutton, N. R. Tummala, D. Beljonne, and J. L. Brédas, *Singlet Fission in Rubrene Derivatives: Impact of Molecular Packing,* Chem. Mater. (2017), 10.1021/acs.chemmater.6b04633.

[150] W. G. Herkstroeter and P. B. Merkel, *The triplet state energies of rubrene and diphenylisobenzofuran,* J. Photochem. (1981), 10.1016/0047-2670(81)80055-X.

[151] T. T. Nakashima and H. W. Offen, *Crystal spectra of tetracene and rubrene under pressure,* J. Chem. Phys. (1968), 10.1063/1.1668088, arXiv:arXiv:1210.1095v1 .

[152] Z. Rang, M. I. Nathan, P. P. Ruden, V. Podzorov, M. E. Gershenson, C. R. Newman, and C. D. Frisbie, *Hydrostatic pressure dependence of charge carrier transport in single-crystal rubrene devices,* Appl. Phys. Lett. (2005), 10.1063/1.1875761.

[153] S. Bergantin, M. Moret, G. Buth, and F. P. A. Fabbiani, *Pressure-induced conformational change in organic semiconductors: Triggering a reversible phase transition in rubrene,* J. Phys. Chem. C (2014), 10.1021/jp503271h.

[154] B. Verreet, P. Heremans, A. Stesmans, and B. P. Rand, *Microcrystalline organic thin-film solar cells,* Adv. Mater. (2013), 10.1002/adma.201301643.

[155] N. J. Hestand and F. C. Spano, *Expanded Theory of H- and J-Molecular Aggregates: The Effects of Vibronic Coupling and Intermolecular Charge Transfer, Chemical Reviews,* (2018), 10.1021/acs.chemrev.7b00581.

[156] F. C. Spano, J. Clark, C. Silva, and R. H. Friend, *Determining exciton coherence from the photoluminescence spectral line shape in poly(3-hexylthiophene) thin films,* J. Chem. Phys. (2009), 10.1063/1.3076079.

[157] S. L. Bayliss, K. J. Thorley, J. E. Anthony, H. Bouchiat, N. C. Greenham, and A. D. Chepelianskii, *Localization length scales of triplet excitons in singlet fission materials,* Phys. Rev. B - Condens. Matter Mater. Phys. (2015), 10.1103/PhysRevB.92.115432.

[158] X. Tian, L. Zhou, X. Chen, Y. Meng, Z. Xiong, X. Zhou, and Y. Zhang, *Nanoscale exponential distance dependence and electron-transfer model for intermolecular singlet exciton fission observed in rubrene-doped organic films,* Org. Electron. Phys. Mater. Appl. (2017), 10.1016/j.orgel.2017.08.009.

[159] H. L. Stern, A. Cheminal, S. R. Yost, K. Broch, S. L. Bayliss, K. Chen, M. Tabachnyk, K. Thorley, N. Greenham, J. M. Hodgkiss, J. Anthony, M. Head-Gordon, A. J. Musser, A. Rao, and R. H. Friend, *Vibronically coherent ultrafast triplet-pair formation and subsequent thermally activated dissociation control efficient endothermic singlet fission,* Nat. Chem. (2017), 10.1038/nchem.2856, arXiv:1704.01695 .

[160] C. K. Yong, A. J. Musser, S. L. Bayliss, S. Lukman, H. Tamura, O. Bubnova, R. K. Hallani, A. Meneau, R. Resel, M. Maruyama, S. Hotta, L. M. Herz, D. Beljonne, J. E. Anthony, J. Clark, and H. Sirringhaus, *The entangled triplet pair state in acene and heteroacene materials,* Nature Communications **8**, 15953 (2017).

[161] S. N. Sanders, E. Kumarasamy, A. B. Pun, K. Appavoo, M. L. Steigerwald, L. M. Campos, and M. Y. Sfeir, *Exciton Correlations in Intramolecular Singlet Fission,* J. Am. Chem. Soc. (2016), 10.1021/jacs.6b00657.

[162] R. D. Pensack, A. J. Tilley, S. R. Parkin, T. S. Lee, M. M. Payne, D. Gao, A. A. Jahnke, D. G. Oblinsky, P. F. Li, J. E. Anthony, D. S. Seferos, and G. D. Scholes, *Exciton delocalization drives rapid singlet fission in nanoparticles of acene derivatives,* J. Am. Chem. Soc. (2015), 10.1021/ja512668r.

[163] A. B. Pun, S. N. Sanders, E. Kumarasamy, M. Y. Sfeir, D. N. Congreve, and L. M. Campos, *Triplet Harvesting from Intramolecular Singlet Fission in Polytetracene,* Adv. Mater. (2017), 10.1002/adma.201701416.

[164] Y. Y. Cheng, A. Nattestad, T. F. Schulze, R. W. Macqueen, B. Fückel, K. Lips, G. G. Wallace, T. Khoury, M. J. Crossley, and T. W. Schmidt, *Increased upconversion performance for thin film solar cells: A trimolecular composition,* Chem. Sci. (2015), 10.1039/c5sc03215f.

[165] Y. L. Lin, M. Koch, A. N. Brigeman, D. M. E. Freeman, L. Zhao, H. Bronstein, N. C. Giebink, G. D. Scholes, and B. P. Rand, *Enhanced sub-bandgap efficiency of a solid-state organic intermediate band solar cell using triplet–triplet annihilation,* Energy Environ. Sci. **10**, 1465 (2017).

[166] J. C. Goldschmidt and S. Fischer, *Upconversion for photovoltaics - a review of materials, devices and concepts for performance enhancement, Advanced Optical Materials,* (2015), 10.1002/adom.201500024.

[167] A. Monguzzi, J. Mézyk, F. Scotognella, R. Tubino, and F. Meinardi, *Upconversion-induced fluorescence in multicomponent systems: Steady-state excitation power threshold,* Phys. Rev. B - Condens. Matter Mater. Phys. (2008), 10.1103/PhysRevB.78.195112.

[168] S. Hisamitsu, N. Yanai, and N. Kimizuka, *Photon-Upconverting Ionic Liquids: Effective Triplet Energy Migration in Contiguous Ionic Chromophore Arrays,* Angew. Chem. - Int. Ed. (2015), 10.1002/anie.201505168.

[169] K. Suzuki, A. Kobayashi, S. Kaneko, K. Takehira, T. Yoshihara, H. Ishida, Y. Shiina, S. Oishi, and S. Tobita, *Reevaluation of absolute luminescence quantum yields of standard solutions using a spectrometer with an integrating sphere and a back-thinned CCD detector,* Phys. Chem. Chem. Phys. **11**, 9850 (2009).

[170] A. K. Bansal, W. Holzer, A. Penzkofer, and T. Tsuboi, *Absorption and emission spectroscopic characterization of platinum-octaethyl-porphyrin (PtOEP),* Chem. Phys. (2006), 10.1016/j.chemphys.2006.08.002.

[171] R. N. Jones, *The ultraviolet absorption spectra of anthracene derivatives,* Chem. Rev. (1947), 10.1021/cr60129a013.

[172] M. A. Baldo, D. F. O'Brien, Y. You, A. Shoustikov, S. Sibley, M. E. Thompson, and S. R. Forrest, *Highly efficient phosphorescent emission from organic electroluminescent devices,* Nature (1998), 10.1038/25954, arXiv:arXiv:1011.1669v3 .

[173] J. Mezyk, R. Tubino, A. Monguzzi, A. Mech, and F. Meinardi, *Effect of an external magnetic field on the up-conversion photoluminescence of organic films: The role of disorder in triplet-triplet annihilation,* Phys. Rev. Lett. (2009), 10.1103/PhysRevLett.102.087404.

[174] R. E. Merrifield, *Theory of Magnetic Field Effects on the Mutual Annihilation of Triplet Excitons,* J. Chem. Phys. (1968), 10.1063/1.1669777, arXiv:1011.1669 .

[175] T. Mani and S. A. Vinogradov, *Magnetic field effects on triplet-triplet annihilation in solutions: Modulation of visible/NIR luminescence,* J. Phys. Chem. Lett. (2013), 10.1021/jz401342b.

[176] P. D. M. G. M. de Abreu, M.Sc., M. Quelhas, André Domingues, C. M. Spieth, Peter, C. M. Bräuer, Götz, M. Knels, Lilla, P. Kasper, Michael, D. Pino, Alexandre Visintainer, J.-U. M. Bleyl, Ph.D., D. M. M. Hübler, Ph.D., F. M. Bozza, D.Sc., M. Salluh, Jorge, B. Kuhlisch, Eberhard, D. Giannella-Neto, Antonio, and T. M. Koch, Ph.D., *Comparative Effects of Vaporized Perfluorohexane and Partial Liquid Ventilation in Oleic Acid– induced Lung Injury,* Anesthesiology **104**, 278 (2006).

[177] G. D. Scholes, *Correlated Pair States Formed by Singlet Fission and Exciton-Exciton Annihilation,* J. Phys. Chem. A (2015), 10.1021/acs.jpca.5b09725.

[178] J. Jonas and A. Jonas, *High-Pressure NMR Spectroscopy of Proteins and Membranes,* Annu. Rev. Biophys. Biomol. Struct. **23**, 287 (1994).

[179] J. Rumble, *CRC Handbook of Chemistry and Physics,*, 99th ed. (CRC Press).

[180] B. Ehrler, M. W. B. Wilson, A. Rao, R. H. Friend, and N. C. Greenham, *Singlet Exciton Fission-Sensitized Infrared Quantum Dot Solar Cells,* Nano Lett. **12**, 1053 (2012).

[181] Y. Wan, Z. Guo, T. Zhu, S. Yan, J. Johnson, and L. Huang, *Cooperative singlet and triplet exciton transport in tetracene crystals visualized by ultrafast microscopy,* Nature Chemistry **7**, 785 (2015).

[182] M. W. Wilson, A. Rao, B. Ehrler, and R. H. Friend, *Singlet exciton fission in polycrystalline pentacene: From photophysics toward devices, Accounts of Chemical Research,* (2013), 10.1021/ar300345h.

[183] P. B. Merkel and D. R. Kearns, *Rate constant for the reaction between 1,3-diphenylisobenzofuran and singlet oxygen,* J. Am. Chem. Soc. **97**, 462 (1975).

[184] A. K. Le, J. A. Bender, and S. T. Roberts, *Slow Singlet Fission Observed in a Polycrystalline Perylenediimide Thin Film,* J. Phys. Chem. Lett. **7**, 4922 (2016).

[185] S. W. Eaton, S. A. Miller, E. A. Margulies, L. E. Shoer, R. D. Schaller, and M. R. Wasielewski, *Singlet Exciton Fission in Thin Films of tert-Butyl-Substituted Terrylenes,* J. Phys. Chem. A **119**, 4151 (2015).

[186] D. Zhao, Y. Yu, C. Wang, W. Liao, N. Shrestha, C. R. Grice, A. J. Cimaroli, L. Guan, R. J. Ellingson, K. Zhu, X. Zhao, R.-G. Xiong, and Y. Yan, *Low-bandgap mixed tin–lead iodide perovskite absorbers with long carrier lifetimes for all-perovskite tandem solar cells,* Nature Energy **2**, 17018 (2017).

[187] M. Saliba, T. Matsui, K. Domanski, J.-Y. Seo, A. Ummadisingu, S. M. Zakeeruddin, J.-P. Correa-Baena, W. R. Tress, A. Abate, A. Hagfeldt, and M. Grätzel, *Incorporation of rubidium cations into perovskite solar cells improves photovoltaic performance,* Science **354**, 206 (2016).

[188] H. Uoyama, K. Goushi, K. Shizu, H. Nomura, and C. Adachi, *Highly efficient organic light-emitting diodes from delayed fluorescence,* Nature **492**, 234 (2012).

[189] G. B. Piland, J. J. Burdett, T.-Y. Hung, P.-H. Chen, C.-F. Lin, T.-L. Chiu, J.-H. Lee, and C. J. Bardeen, *Dynamics of molecular excitons near a semiconductor surface studied by fluorescence quenching of polycrystalline tetracene on silicon,* Chemical Physics Letters **601**, 33 (2014).

[190] S. Lee, D. Hwang, S. I. Jung, and D. Kim, *Electron Transfer from Triplet State of TIPS-Pentacene Generated by Singlet Fission Processes to $CH_3NH_3PbI_3$ Perovskite,* J. Phys. Chem. Lett. **8**, 884 (2017).

[191] M. Abdi Jalebi, *Chemical Modifications and Passivation Approaches in Metal Halide Perovskite Solar Cells*, Doctoral Thesis, University of Cambridge.

[192] S. W. Tabernig, B. Daiber, T. Wang, and B. Ehrler, *Enhancing silicon solar cells with singlet fission: The case for Förster resonant energy transfer using a quantum dot intermediate,* Journal of Photonics for Energy **8**, 022008 (2018).

[193] C.-H. Chen, N. T. Tierce, M.-k. Leung, T.-L. Chiu, C.-F. Lin, C. J. Bardeen, and J.-H. Lee, *Efficient Triplet–Triplet Annihilation Upconversion in an Electroluminescence Device with a Fluorescent Sensitizer and a Triplet-Diffusion Singlet-Blocking Layer,* Advanced Materials **30**, 1804850 (2018).

[194] G. Grancini, C. Roldán-Carmona, I. Zimmermann, E. Mosconi, X. Lee, D. Martineau, S. Narbey, F. Oswald, F. De Angelis, M. Graetzel, and M. K. Nazeeruddin, *One-Year stable perovskite solar cells by 2D/3D interface engineering,* Nat. Commun. (2017), 10.1038/ncomms15684, arXiv:1609.09846 .

[195] B. Schatschneider, J.-J. Liang, A. M. Reilly, N. Marom, G.-X. Zhang, and A. Tkatchenko, *Electrodynamic response and stability of molecular crystals,* Phys. Rev. B **87**, 060104 (2013).

About the author

Tianyi Wang was born in Nantong, China on February 21, 1990. After receiving high school diploma from Nantong Middle School in 2008, he did a Bachelor's degree in Materials Science and Engineering at Nanjing University of Aeronautics and Astronautics and graduated in 2012 with a thesis focusing on the chemical bath deposition of tin sulfide thin films for photovoltaic applications under the supervision of Prof. Honglie Shen.
From 2012 to 2014, he studied Materials Science at Ludwig Maximilian University of Munich, Technical University of Munich and University of Montpellier under the Erasmus Mundus Master Program MAMASELF and graduated with a thesis on the low temperature fabrication of superstructured titania thin films via wet imprinting and characterization of these films using GISAXS under the supervision of Prof. Peter Müller-Buschbaum. In 2014 he started working as a PhD student in the Hybrid Solar Cells group at Insititute AMOLF in Amsterdam, the Netherlands, under the supervison of Dr. Bruno Ehrler. The results of this PhD project are presented in this thesis.